LONG-RANGE SHOCK PROPAGATION IN OCEAN WAVEGUIDES

by

Joseph T. Maestas

A thesis submitted to the Faculty and the Board of Trustees of the Colorado School of Mines in partial fulfillment of the requirements for the degree of Doctor of Philosophy (Applied Mathematics & Statistics).

Golden, Colorado

Date _____

Signed: _____
Joseph T. Maestas

Signed: _____
Dr. Jon Collis
Thesis Advisor

Golden, Colorado

Date _____

Signed: _____
Dr. Willy Hereman
Professor and Head
Department of Applied Mathematics & Statistics

ABSTRACT

Shock waves in the ocean are able to propagate over hundreds of meters as they slowly decay into linear sound waves. Accurate assessment of shock is therefore necessary to describe acoustic signals originating from high intensity sources which necessitates the use of specialized models that can both accurately describe the shock and be computationally efficient over large domains. There are a number of nonlinear acoustic models in existence, but the principle model for ocean acoustics is the nonlinear progressive wave equation (NPE) [B. E. McDonald *et al.*, JASA **81**]. The NPE is a time-domain formulation of Euler's fluid equations designed to model low-angle wave propagation using a wave-following computational domain. However, the current form of the model is not capable of fully describing realistic ocean environments as it can only describe waves in non-dispersive fluid media. In this work, the NPE is adapted to treat physically relevant ocean bottom sediments by accounting for sound absorption and weak elasticity. The accuracy of the model is seen to break down for fully elastic media where shear wave phenomena cannot be overlooked. Additional models, based on finite-volume methods, are developed to treat shock propagation in such environments using high-order Godunov schemes. These models are valid in range-dependent settings and properly describe nonlinear elastodynamic wave propagation, but require additional computing resources.

TABLE OF CONTENTS

LIST OF FIGURES

LIST OF TABLES

LIST OF SYMBOLS

material derivative . . . . . D_t

partial derivative with respect to time . . . . . ∂_t

partial derivative with respect to the x dimension . . . . . ∂_x

partial derivative with respect to the y dimension . . . . . ∂_y

partial derivative with respect to the z dimension . . . . . ∂_z

second partial derivative with respect to the x dimension . . . . . ∂_x^2

second partial derivative with respect to the y dimension . . . . . ∂_y^2

second partial derivative with respect to the z dimension . . . . . ∂_z^2

coefficient of nonlinearity . . . . . β

sound speed c

pressure (primary) wave speed . . . . . c_p

shear (secondary) wave speed . . . . . c_s

density . . . . . ρ

pressure . . . . . p

displacement components . . . . . u_i

velocity components . . . . . v_i

Lamé's first parameter/wavelength . . . . . λ

shear modulus . . . . . μ

bulk modulus . . . . . K

frequency . . . . . f

angular frequency . . . . . ω

attenuation coefficient . . . . . α

absorption coefficient . . . . . α_0

power law exponent . . . . . γ

dimensionless density perturbation . . . . . R

dimensionless pressure perturbation . . . . . Q

x direction normal stress . . . . . σ_{xx}

z direction normal stress . . . . . σ_{zz}

in-plane shear stress . . . . . σ_{xz}

horizontal grid spacing (cell width) . . . . . Δx

vertical grid spacing (cell height) . . . . . Δz

time step . . . . . Δt

slope limiter . . . . . χ

sound diffusivity . . . . . ζ

LIST OF ABBREVIATIONS

Nonlinear Progressive Wave Equation . . . . . NPE

Parabolic Equation . . . . . PE

Flux-Corrected Transport . . . . . FCT

Range-dependent Acoustic Model . . . . . RAM

Khokhlov-Zabolotskaya-Kuznetzov model . . . . . KZK

Finite-Difference . . . . . FD

Crank-Nicolson . . . . . CN

Absorbing Sponge Zone . . . . . ASZ

meters . . . . . m

seconds . . . . . s

kilometers . . . . . km

decibels . . . . . dB

nepers . . . . . Np

ACKNOWLEDGMENTS

I would like to thank the Trefny Institute for Educational Innovation for awarding me the Bechtel Fellowship which partially funded this work. This thesis would not have succeeded without the guidance of Dr. Jon Collis.

CHAPTER 1

INTRODUCTION

The main focus of this research is to generate computational models that accurately describe shock propagation in oceanic waveguides in both the water column and the ocean bottom. The models must be efficient for long-range problems; so the models used in this work tend to be progressive. Here, a progressive model refers to one in which the computational domain moves at a specified velocity in order to track the wavefront. These models are computationally efficient, but they lose any information that leaves the computational domain such as fast head waves or back-scattered waves.

This work concentrates mostly on how shock propagates in different ocean bottom media. The effect of ocean bottoms on pulse propagation in shallow water environments is profound and must be accurately accounted for. In a realistic ocean environment, the seafloor can comprise of loose, unconsolidated sediments, densely packed saturated muds, and hard rock. Most ocean floors actually contain some combination of all three types of material. Each type of material affects shock propagation in a different way. Loose, unconsolidated sediments often have shear wave speeds that are slow enough that shear effects can be neglected (they can be approximated as fluids), but the loose packing of the particles allows for wave energy to be converted into heat by friction. This conversion or loss mechanism can play a strong role in the overall strength of a shock wave or acoustic signal. For densely packed saturated muds, sound absorption from particle friction is still present, but may not be as pronounced. However, at some point the mud is compacted enough to support appreciable shear waves, and these shear waves can have an effect on the overall propagation of a pulse. Shear waves are very strong in hard rock, and the strength of the shear wave is on the same order of magnitude as the compressional wave strength and therefore cannot be neglected.

This thesis is organized to address each of these three material types. The outline below gives a brief summary of the main chapters, how they address a certain material type, and

the significance of the contribution to the scientific community. First, chapter 2 gives the background behind long-range shock propagation in the ocean, including current state-of-the-art, applications, and the author's prior investigations. Each individual chapter will also give a brief background for the theory and methods presented therein.

Chapter 3 is focused on adapting the current model of choice, the nonlinear progressive wave equation (NPE) to treat unconsolidated attenuating sediments. This is done by adding a fractional loss operator to the NPE formulation. Results agree well with the parabolic equation (PE) solution for the linear case. Nonlinear studies show absorption has a profound effect on shock propagation. This important physical result indicates that sediment attenuation must be accounted for when analyzing shock originating from within the sediment.

Chapter 4 looks at the derivation of a weakly-elastic NPE. The derivation of the original NPE is adapted to describe wave motion in a linear elastic medium where shear stress is a second order effect when compared to normal stress. The process provides information on the approximate shear wave field, but the resulting equation is not valid for fully elastic media. This model is a significant contribution because it allows for a method to determine at what point the fluid approximation becomes unreasonable when modeling low-shear media.

Chapter 5 looks at the development of shock models for fully elastic media. The framework of the NPE is abandoned in favor of more robust finite-volume methods. The models allow for the description of compressional and shear waves, the treatment of environments with discontinuous material properties, the ability to handle stronger shocks, and more accurate scattering than was provided with the NPE, but at increased computational cost. The final models will be a significant contribution because these numerical methods have yet to be applied to long-range ocean acoustic problems.

Finally, chapter 6 gives a closing discussion and conclusions that have been drawn from this work. Potential avenues of future work are presented as well. Supplemental materials are presented in the appendices attached to this document.

CHAPTER 2

BACKGROUND

Long-range shock propagation in the ocean is a complex problem that requires multiple models to accurately resolve the solution at different stages of its progression. Near the high intensity source (such as an explosion) where the shock is formed, pressures and temperatures are high enough to significantly alter the wave's structure. Numerical models in this regime must be able to account for nonlinear material behavior, phase change, and strong shock development. Typical models for the near-source are based on direct, first-principles physics – conservation of mass, momentum, and energy – and are known as hydrocodes. While robust, these models require a significant amount of computing resources and are therefore not effective for modeling propagation over long distances. If the shock has decayed to the point where temperature effects are negligible then a nonlinear acoustics model can be employed. These models are based on approximations to the governing equations and are much more efficient than hydrocodes. They allow the wave to be described in the so-called mid-source regime, the range over which the nonlinearity is weak. Finally, once the shock has decayed into an acoustic wave, highly efficient linear models can be used to march the solution over extremely long distances, in the far-source regime.

There exists a vast knowledge base for models in the near-source regime. Hydrocodes based on various numerical schemes have been investigated thoroughly and continue to be studied and implemented. The reader is directed to (Hertel, 1997) for a practical overview of hydrocodes and their history. Models in the far-source regime, linear acoustic models, have also been and continue to be studied extensively. *Computational Ocean Acoustics* (Jensen *et al.*, 2005) provides an excellent account of these linear models. Models in the mid-source regime, however, have not been studied as comprehensively. Models of this type tend to come from a nonlinear acoustics basis and, while rich in theory, tend to overlook details and mechanisms seen in real-world problems. The aim of this work is to develop models for this

regime that treat the nonlinear nature of the shock wave while also accurately capturing other physically important mechanisms that exist in underwater ocean environments. The following sections give an overview of the main mathematical models used in nonlinear acoustics, how they apply to the underwater shock problem, and the current state-of-the-art.

2.1 Mathematical Nomenclature

Before model descriptions are given, it is necessary to define the naming conventions as used in ocean acoustics. Generally, in ocean acoustics, the environment is defined by depth, range, and transverse direction: depth, or the z axis, starts from zero at the surface and positively increases as depth increases, range, or the x axis, is specified as the direction of propagation, and the transverse direction, or the y axis, is defined as the direction perpendicular to the xz plane. This work looks at 2D models, however 3D effects can strongly affect wave propagation in certain instances, but will be left for future endeavors.

Underwater environments can be characterized as depth-dependent, range-dependent, or spatially three-dimensionally dependent. In depth-dependent environments, the properties of the fluid (density and speed of sound) can vary with depth only. In range-dependent environments, the properties of the fluid will vary with range, and the geometry can change with range as well such as with variably sloping ocean bottoms. In three-dimensionally dependent environments, the medium properties can vary in all directions. In some cases, medium properties may vary with time, four-dimensional dependence, but this work is mainly focused on spatial variation in at most two dimensions.

The underwater environment is described by fields of state variables such as pressure p and density ρ and by medium properties such as unperturbed density ρ_0 and sound speed c_0. Different material properties may be necessary to define other mechanisms such as attenuation, thermal effects, or cavitation. For elastic media, process variables such as particle velocity are required and different state variable choices must be used. The mathematical

description of the problem of interest is given in each chapter of this thesis.

2.2 Nonlinear Acoustic Models

As mentioned previously, this work is focused on developing models for the mid-source regime, the range over which the shock propagating is considered weak. Models in this regime have historically been developed from a nonlinear acoustics framework. This section presents four fundamental equations of nonlinear acoustics: the Fubini-Bessel solution, Burgers' equation, the Westervelt equation, and the KZK equation. Each mathematical model differs in complexity and applicability to the underwater shock problem.

2.2.1 The Fubini-Bessel Solution

Fubini developed a solution for the propagation of nonlinear acoustic waves of single-frequency, sinusoidal sources. The solution is only valid for very weakly nonlinear waves where a steep shock front has yet to form. The acoustic pressure field is expressed as an infinite sum of weighted Bessel functions:

$$p(\sigma,\tau) = p_0 \sum_{n=1}^{\infty} \frac{2}{n\sigma} J_n(n\sigma)\sin(n\omega\tau), \tag{2.1}$$

where $\sigma = \omega p_0 x/c_0^2$ is the shock formation distance, $\tau = t - x/c_0$ is reduced time, p_0 is the initial sinusoidal amplitude, ω is the source frequency, and J_n is the Bessel function of order n. The solution is not valid for $\sigma>1$, the post-shock region. The Fubini-Bessel solution is very fast to implement and solve, but can only treat 1D problems and therefore is not able to treat realistic underwater environments. Also, this model does not account for any type of loss mechanism, cannot truly describe a shock formation, and is valid for only monofrequency sources whereas explosive sources tend to be broadband. These reasons make this model a poor choice for the underwater shock problem.

2.2.2 Burgers' Equation

Burgers' equation is a 1D model that is able to describe the combined effects of nonlinearity and dissipation on the propagation of plane waves. The equation is given by

$$\frac{\partial p}{\partial x} - \frac{\zeta}{2c_0^3}\frac{\partial^2 p}{\partial \tau^2} = \frac{\beta}{2\rho_0 c_0^3}\frac{\partial p^2}{\partial \tau}, \tag{2.2}$$

where ζ is the sound diffusivity, a parameter that accounts for the viscous dissipative loss (see Section 3.2 for a detailed definition). The parameter $\tau = t - x/c_0$ is represents reduced time, ρ_0 is the background pressure, and β is the coefficient of nonlinearity for the material and is physically defined by $\beta = 1 + \frac{\rho}{c}\frac{\partial c}{\partial \rho}$. This model allows for the treatment of weak shock and viscous loss, but it is not capable of describing complex two or three dimensional environments such as ocean-bottom interaction or ocean-surface interaction. Also, the loss mechanism follows a square frequency dependence (Szabo, 1993) which may not accurately describe the material of interest within an ocean environment. Chapter 3 provides more detail on the loss mechanisms seen in typical ocean environments.

2.2.3 The Westervelt Equation

Burgers' equation can be generalized to higher dimensions which leads to Westervelt equation. This wave equation can account for nonlinearity up to the second order and is given by

$$\nabla^2 p - \frac{1}{c_0^2}\frac{\partial^2 p}{\partial t^2} + \frac{\zeta}{c_0^4}\frac{\partial^3 p}{\partial t^3} = -\frac{\beta}{\rho_0 c_0^4}\frac{\partial^2 p^2}{\partial t^2}, \tag{2.3}$$

where the parameters are the same as for Burgers' equation. Unlike Burgers' equation, this model defines a solution in terms of space and time, rather than space and reduced time. It is not only able to account for nonlinearity and dissipation, but it can also describe two dimensional effects such as ocean-bottom and ocean-surface interaction, given the appropriate boundary conditions. However, with this model it is necessary to calculate the acoustic field for the entire domain of interest. For long-range shock propagation this leads to unrea-

sonable computing times. Generalized Westervelt equations have been developed to cast the equation into material coordinates and account for discontinuous media (Taraldsen, 2001). These methods are untested in the area of ocean acoustics.

2.2.4 The KZK Equation

A parabolic approximation to the Westervelt equation leads to the KZK (Khokhlov-Zaboloskaya-Kuznetsov) equation (Zabolotskaya & Khokhlov, 1969). The KZK equation is

$$\frac{\partial^2 p}{\partial z \partial \tau} = \frac{c_0}{2}\nabla_\perp^2 p + \frac{\zeta}{2c_0^3}\frac{\partial^3 p}{\partial \tau^3} + \frac{\beta}{2\rho_0 c_0^3}\frac{\partial^2 p^2}{\partial \tau^2}, \tag{2.4}$$

where z is the acoustic beam propagation direction and $\nabla_\perp^2 = \partial^2/\partial x^2 + \partial^2/\partial y^2$ is the perpendicular Laplacian. This model accounts for the effects of diffraction, absorption, and nonlinearity for directional sound beams. Describing complex domains such as sloping ocean bottoms can be difficult due to the time-formalization. There have been recent developments, however, that allow for the modeling of weak range-dependence, that is, small variations in medium properties (Jing & Cleveland, 2007), but these methods cannot handle sloping bottoms where variations in medium properties are large.

2.3 The Nonlinear Progressive Wave Equation

The current state-of-the-art model for long-range underwater shock problems is the nonlinear progressive wave equation (NPE) originally derived by McDonald and Kuperman (McDonald & Kuperman, 1987). This section provides a description of the model, its implementation, and deficiencies. New models developed in the following chapters address these deficiencies.

The NPE is a time-domain wave propagation model used to describe an acoustic pulse by means of a moving computational domain that tracks the wave front. This model is mathematically equivalent to the inviscid KZK model but in a space-formalization that allows for a more straightforward representation of physical domains (Castor *et al.*, 2002). It

was originally developed to describe long-range underwater acoustic propagation from high intensity sources (such as explosions) due to its efficient moving grid formulation. The NPE is derived in terms of a single variable from Euler's conservation of mass and momentum equations with the assumptions that associated shocks are weak and that propagation is strongest in the preferred direction of propagation (range direction). The complete derivation can be found in (McDonald *et al.*, 1994) and (Caine & West, 1995).

In Cartesian coordinates, the NPE is given by

$$D_t R = -\partial_x \left[c_1 R + \frac{\beta c_0}{2} R^2 \right] - \frac{c_0}{2} \int_{x_f}^{x} (\partial_y^2 + \partial_z^2) R \, \mathrm{dx}, \tag{2.5}$$

where $R = \rho'/\rho_0$ is a dimensionless density perturbation (the density perturbation ρ' is scaled by the background density ρ_0) and $c_1(x, y, z) = c(x, y, z) - c_0$ represents a small variation from the medium's average sound speed. In the above equation, the shorthand notations for the temporal and spatial derivatives are employed: $D_t = \frac{D}{Dt}$, $\partial_a = \frac{\partial}{\partial a}$, and $\partial_a^2 = \frac{\partial^2}{\partial a^2}$, $a = x, y, z$. For the purposes of this paper, only two-dimensional propagation is considered; ∂_y^2 is disregarded so that the unknown R is a function of x, z, and t. Physically, the two dimensional approximation is proposed assuming an axisymmetric problem. However, 2D Cartesian coordinates are adopted rather than 2D cylindrical coordinates because the problem is practically in plane strain, with the exception of a cylindrical spreading loss term which can be applied in post-processing using a proportionality law (Jensen *et al.*, 2005). The domain of consideration is, in general, defined by a grid (x, z), with the positive x axis pointing to the right and the positive z axis pointing down. The lower limit of the integral, x_f, is taken to be a point ahead of the pulse where $R = \partial_x R = 0$. For the propagation of a discrete pulse, one has only to begin the integral ahead of the pulse (McDonald & Kuperman, 1987) (a fact that will be utilized in the formulation of FD methods following this section).

Each term in (2.5) represents a different physical process: the process of refraction is described by $-\partial_x(c_1 R)$, nonlinear steepening by $-\partial_x(\frac{\beta c_0}{2} R^2)$, and diffraction by $\frac{-c_0}{2} \int_{x_f}^{x} \partial_z^2 R \, \mathrm{dx}$.

Refraction can be defined as the change in a direction of a wave due to small changes in the sound speed of the medium; the refractive term is defined as such because it consists of the dependent variable R multiplied by c_1, a value which represents a perturbation to the sound speed. The nonlinear steepening term is defined as such because it contains the dependent variable R nonlinearly; thus β is called the "coefficient of nonlinearity". Diffraction can be defined as how a wave will bend after encountering an obstacle; thus the diffraction term can be so named because it describes how wave propagation in one direction is affected by factors described in another direction.

The different mathematical representations of each physical term naturally leads to different numerical treatments for each term: the refraction and nonlinear steepening terms (hereafter referred to as the nonlinear terms) are treated with flux-corrected transport (FCT), and the results obtained are then used as a correction to the diffraction term (hereafter referred to as the linear term) which is treated by using the trapezoidal rule to approximate the integral, a second-order finite-difference (FD) formula to approximate the z derivative, and finally a Crank-Nicolson (CN) update to march forward in time.

2.3.1 Numerical Schemes

Numerical evaluation of the NPE involves discretizing the solution on a computational domain. Recall that effects due to changes in the y direction are ignored, so the general domain described is $x_0 \leq x \leq x_N$ meters (m) wide and $z_0 \leq z \leq z_M$ m deep, where the endpoints of each interval are finite values. In general, $x_0 = c_0 t$, the distance traveled by the grid (with a flat ocean bottom), and z_0 equals zero, a common designation for the ocean surface. Also, to simplify further calculations the following definitions are made: $W \equiv x_N - x_0$, the width of the computational domain, and $D \equiv z_M - z_0$, the depth or height of the computational domain. Each direction is represented by a uniform grid such that $x_i = i\Delta x$, $i = 0, 1, \ldots, N$, and $z_j = j\Delta z$, $j = 0, 1, \ldots, M$. Time is also discretized on a uniform grid such that $t_n = n\Delta t$, $n = 0, 1, \ldots, L$; time begins at $t = 0$ s and simulations

are carried out to some finite time value $t = t_L$ s. The solution is then given on the domain, $(x_0 \leq x \leq x_N, z_0 \leq z \leq z_M, 0 \leq t \leq t_L)$, as $R(x_i, z_j, t_n)$. This discrete grid will be used throughout this section. Initial and boundary conditions are described in the next section.

The nonlinear terms in the NPE depend solely on x (due to the x derivative), so FCT is applied to each jth column of constant depth. Thus, for a two-dimensional problem, FCT is applied $M + 1$ times for a single time step. In contrast, the linear terms of the NPE depend on both x (due to the integral) and z (due to the second z derivative), therefore the FD scheme is applied on all grid points, or $(N + 1)(M + 1)$ times, for every time step. Details of each method are given below.

Flux-Corrected Transport The FCT method (McDonald & Ambrosiano, 1984) is a hybrid scheme, resulting from a combination of first and second-order upwind discretization methods. Central to the scheme is the computation of flux terms, so chosen to preserve monotonicity in the numerical solution, a property that will forbid the generation of new extrema (results that would be numerically inaccurate) or the enhancement of old extrema (results that would be physically unrealistic). Fluxes are computed at intermediate grid points $x_{i+\frac{1}{2}}$, placed at the midpoint of x_i and x_{i+1}. Using these intermediate points, the first portion of the algorithm is first-order, as calculations centered at $x_{i+\frac{1}{2}}$ relate to one grid point to the immediate left or right (x_i or x_{i+1}); the results are first-order accurate, but not enough to prevent the rapid advancement of numerical errors. To correct such errors, second-order results centered at $x_{i+\frac{1}{2}}$ that now relate to two grid points to the immediate left or right (x_{i-1} and x_i or x_{i+1} and x_{i+2}) are computed. The first-and second-order results are then combined to give a stable scheme that can be used to accurately deal with any nonlinearities present in the solution to the NPE.

The portion of (2.5) to be evaluated using the FCT algorithm is written as

$$D_t R = -\partial_x \left(c_1 R + \frac{\beta c_0}{2} R^2 \right). \tag{2.6}$$

Equations presented in this section are calculated for all $i = 0, 1, \ldots, N$ at fixed j, and are used toward obtaining the solution at time t_{n+1}. One begins the scheme by computing

$$\phi_i^n = c_1 R_i^n + \frac{\beta c_0}{2}(R_i^n)^2. \tag{2.7}$$

Calculations now begin at the intermediate grid points; a characteristic direction variable, $w_{i+\frac{1}{2}}^n$, and the first-order fluxes, $f_{i+\frac{1}{2}}^n$, are computed using the stored values of ϕ_i^n. These terms are defined as:

$$w_{i+\frac{1}{2}}^n = (\phi_{i+1}^n - \phi_i^n)(R_{i+1}^n - R_i^n) \tag{2.8}$$

$$f_{i+\frac{1}{2}}^n = \frac{\Delta t}{\Delta x} \begin{cases} \phi_i^n & \text{if } w_{i+\frac{1}{2}}^n \geq 0 \\ \phi_{i+1}^n & \text{if } w_{i+\frac{1}{2}}^n < 0 \end{cases}. \tag{2.9}$$

The fluxes $f_{i+\frac{1}{2}}^n$ are corrected using the characteristic speed, $u_i^n = \partial_x(\phi_i^n)$. If $u_i^n < 0$ and $u_{i+1}^n > 0$, then a correction is applied such that

$$f_{i+\frac{1}{2}}^n = \frac{1}{2}\left(f_{i+\frac{3}{2}}^n + f_{i+\frac{1}{2}}^n - \frac{\Delta t}{\Delta x}(R_{i+1}^n - R_i^n)(u_{i+1}^n - u_i^n)\right), \tag{2.10}$$

otherwise the flux remains unchanged. Next, one computes and saves R_i^* (an update that preserves monotonicity) and ϕ_i^* (ensuring the stability of the second-order scheme):

$$R_i^* = R_i^n - f_{i+\frac{1}{2}}^n + f_{i-\frac{1}{2}}^n \tag{2.11}$$

$$\phi_i^* = \phi_i^n - \frac{1}{2}u_i^n(f_{i+\frac{1}{2}}^n - f_{i-\frac{1}{2}}^n). \tag{2.12}$$

The second-order fluxes, $F_{i+\frac{1}{2}}^n$, are then computed as

$$F_{i+\frac{1}{2}}^n = \frac{\Delta t}{2\Delta x} \begin{cases} 3\phi_i^* - \phi_{i-1}^* & \text{if } w_{i+\frac{1}{2}}^n \geq 0 \\ 3\phi_{i+1}^* - \phi_{i+2}^* & \text{if } w_{i+\frac{1}{2}}^n < 0 \end{cases}. \tag{2.13}$$

These fluxes are also corrected using the characteristic speed as in (2.10). Using $f_{i+\frac{1}{2}}^n$ and $F_{i+\frac{1}{2}}^n$, one can compute the flux correction $\delta f_{i+\frac{1}{2}}^n$ as

$$\delta f_{i+\frac{1}{2}}^n = F_{i+\frac{1}{2}}^n - f_{i+\frac{1}{2}}^n, \tag{2.14}$$

which is filtered using a flux limiter, given by

$$\delta f^n_{i+\frac{1}{2}} = s^n_{\delta f,i+\frac{1}{2}} \max(0, \min[|\delta f^n_{i+\frac{1}{2}}|, s^n_{\delta f,i+\frac{1}{2}}(R^*_{i+2} - R^*_{i+1}), s^n_{\delta f,i+\frac{1}{2}}(R^*_i - R^*_{i-1})]) \tag{2.15}$$

for $s^n_{\delta f,i+\frac{1}{2}}$, the sign of $\delta f^n_{i+\frac{1}{2}}$ (defined as one if $\delta f^n_{i+\frac{1}{2}} = 0$). It is necessary to apply the limiting function (or so-called filter) to $\delta f^n_{i+\frac{1}{2}}$ because the second-order scheme does not inherently preserve monotonicity, as does the first-order scheme, otherwise $F^n_{i+\frac{1}{2}}$ could introduce numerical errors at this step. Further, the choice of filter is not unique; different problems may require more appropriate choices of filter. An appropriate filter may be chosen through trial and error (the filter used in this work is as described by (McDonald & Ambrosiano, 1984)). The scheme is then completed with the calculation

$$R^{n+1}_i = R^*_i - \delta f^n_{i+\frac{1}{2}} + \delta f^n_{i-\frac{1}{2}}. \tag{2.16}$$

In summary, to accurately numerically evaluate the nonlinear terms in the NPE one can follow the steps outlined in this section. The correct order of the steps is as follows: (2.7), (2.8), (2.10) (if the conditions placed on u^n_i and u^n_{i+1} are satisfied), (2.11), (2.13), (2.10) (with $f^n_{i+\frac{1}{2}}$ replaced by $F^n_{i+\frac{1}{2}}$ if the conditions placed on u^n_i and u^n_{i+1} are satisfied), then (2.14), (2.15), and (2.16). Through the use of selective upwinding methods (dependent upon the direction of the characteristic speed of the unknown at intermediate grid points) and appropriate filters applied to the combined fluxes, numerical errors that may result during evaluation will be corrected at each time step, preventing effects that may be physically inaccurate from developing.

Finite-Difference Method Finite-difference (FD) methods are commonly used to numerically evaluate partial differential equations as they offer good accuracy and are relatively simple to implement. In some cases, such methods may be appropriate for only a few terms of the equation, and must then be combined with other evaluation methods. Such is the

case when dealing with the NPE. A numerical scheme, resulting from a combination of FD approximations of derivatives, a trapezoid rule approximation for the integral, and a CN update, is used to evaluate the linear term not treated by the previously described FCT algorithm.

The portion of (2.5) to be evaluated using finite-differences is written as

$$D_t R = \frac{-c_0}{2} \int_{x_f}^{x} \partial_z^2 R \ \mathrm{dx}. \tag{2.17}$$

This portion of the NPE is fundamentally different than the nonlinear portion described in the previous section; here, the unknown is dependent upon two spatial dimensions. This difference affects the discretization used, as discussed at the beginning of the section. Calculations are done at each grid point for all $i = 0, 1, \ldots, N$ and $j = 0, 1, \ldots, M$, and are used to obtain the solution at the next time step t_{n+1}. Also, recall that $D_t = \partial_t + c_0 \partial_x$ was introduced in the derivation of the NPE, where its dependence on ∂_x has already been accounted for in the NPE formulation; numerical approximations of D_t are then treated the same as those given for ∂_t. The FD formulas that approximate the derivatives in (2.17) are given by:

$$\partial_z^2 R_{i,j}^n \approx \frac{R_{i,j-1}^n - 2R_{i,j}^n + R_{i,j+1}^n}{\Delta z^2} \tag{2.18}$$

$$D_t R_{i,j}^n \approx \frac{R_{i,j}^{n+1} - R_{i,j}^n}{\Delta t}. \tag{2.19}$$

Employing the CN method (averaging the $\partial_z^2 R$ term in time) provides more accuracy and transforms (2.17) into

$$\partial_t R_{i,j}^n = \frac{-c_0}{2} \int_{x_f}^{x} \frac{1}{2} \left(\partial_z^2 R_{i,j}^n + \partial_z^2 R_{i,j}^{n+1} \right) \ \mathrm{dx}. \tag{2.20}$$

Applying formulas (2.18) and (2.19) to (2.20) gives

$$\frac{R_{i,j}^{n+1} - R_{i,j}^{n}}{\Delta t} = \frac{-c_0}{4\Delta z^2} \int_{x_f}^{x} \left(R_{i,j-1}^{n} - 2R_{i,j}^{n} + R_{i,j+1}^{n} + R_{i,j-1}^{n+1} - 2R_{i,j}^{n+1} + R_{i,j+1}^{n+1} \right) \, \mathrm{dx}. \tag{2.21}$$

Numerically, the upper limit of the integral is representative of a grid point x_i, and the lower limit is taken to be the right-most grid point $x_f = x_N$. The trapezoidal rule is then applied to the integral such that

$$\int_{x_N}^{x_i} R_{i,j}^{n} \, \mathrm{dx} \approx \frac{-\Delta x}{2} \left(R_{i,j}^{n} + R_{N,j}^{n} + 2 \sum_{k=i+1}^{N-1} R_{k,j}^{n} \right). \tag{2.22}$$

The fact that $R_{N,j}^{n} = 0$ (representative of a quiescent medium ahead of the pulse) is used to eliminate this term in the approximation. Substituting Eqn. (2.22) into Eqn. (2.21) and moving all unknown terms to the left hand side results in an $N \times M$ system of linear equations for $R_{i,j}^{n+1}$, given by

$$\begin{aligned} R_{i,j}^{n+1} \quad - \quad & \frac{c_0 \Delta t \Delta x}{8\Delta z^2} (R_{i,j-1}^{n+1} - 2R_{i,j}^{n+1} + R_{i,j+1}^{n+1}) = R_{i,j}^{n} + \frac{c_0 \Delta t \Delta x}{8\Delta z^2} (R_{i,j-1}^{n} - 2R_{i,j}^{n} + R_{i,j+1}^{n}) \\ + \quad & \frac{c_0 \Delta t \Delta x}{4\Delta z^2} \sum_{k=i+1}^{N-1} (R_{k,j-1}^{n} - 2R_{k,j}^{n} + R_{k,j+1}^{n} + R_{k,j-1}^{n+1} - 2R_{k,j}^{n+1} + R_{k,j+1}^{n+1}). \end{aligned} \tag{2.23}$$

This system is now rewritten using matrix-vector notation. Let $\sigma = \frac{c_0 \Delta t \Delta x}{8\Delta z^2}$, and consider $R_{i,j}^{n}$ for all $j = 0, 1, \ldots, M$ and fixed i to create the $M \times 1$ column vector

$$\vec{R}_i^{n} = (R_{i,1}^{n} \; R_{i,2}^{n} \; \ldots \; R_{i,M-1}^{n} \; R_{i,M}^{n})^T.$$

The system (2.23) can then be written as the condensed system of N linear equations

$$(\mathbf{I} - \sigma \mathbf{A}) \vec{R}_i^{n+1} = (\mathbf{I} + \sigma \mathbf{A}) \vec{R}_i^{n} + 2\sigma \sum_{k=i+1}^{N-1} (\mathbf{A}(\vec{R}_k^{n} + \vec{R}_k^{n+1})) \tag{2.24}$$

where $\mathbf{A} = \begin{bmatrix} 2 & -1 & \cdots & 0 \\ -1 & \ddots & \ddots & \vdots \\ \vdots & \ddots & \ddots & -1 \\ 0 & \cdots & -1 & 2 \end{bmatrix}$ is the $M \times M$ matrix resulting from approximating the z derivative, and $\mathbf{I}$ is the $M \times M$ identity matrix. The fact that this is a banded, tridiagonal system allows the use of specialized sparse matrix solvers, increasing efficiency. Boundary and interface conditions specific to a given problem are then incorporated in the matrix $\mathbf{A}$ when discretized.

Defining the vector and matrix quantities in this way allows one to solve for a matrix of unknown values

$$\mathbf{R}^{n+1} = [\vec{R}_1^{n+1}\ \vec{R}_2^{n+1}\ \ldots\ \vec{R}_i^{n+1}\ \ldots\ \vec{R}_{N-1}^{n+1}\ \vec{R}_N^{n+1}]$$

column-wise from right to left (a result that is representative of beginning the integral ahead of the pulse). That is, one first applies $R_{N,j}^{n+1} = 0$, then solves for $R_{N-1,j}^{n+1}$, and so on; thus all the terms in the summation are known quantities. The efficiency provided by the vectorization and the fact that CN methods are numerically stable (granted the choices of Δx, Δz and Δt are compliant with the Courant-Friedrichs-Lewy condition) give confidence that the scheme will not only provide accurate results when applied to the NPE but will provide them in an acceptable amount of computation time. This numerical formulation is appropriate for only the simplest of cases (perfectly reflecting boundaries). In order to account for more complex environments such as penetrable ocean bottoms, sediment layering, and sloping bathymetry certain adjustments need to be made to the numerical scheme; details of such cases will be provided in the following sections.

2.3.2 Boundary Conditions

The standard NPE is written in terms of a dimensionless density perturbation, R, which is not conducive for applying boundary conditions. It is possible to reformulate the NPE in

terms of a dimensionless pressure variable $Q \equiv p'/\rho_0 c_0^2$ (Ambrosiano *et al.*, 1990):

$$D_t Q = -\partial_x \left[c_1 Q + \frac{\beta c_0}{2} Q^2 \right] - \frac{c_0}{2} \int_{x_f}^{x} (\partial_y^2 + \partial_z^2) Q \, \mathrm{dx}. \tag{2.25}$$

This form of the equation is no different than the original formulation. The reason for this is because $Q = R + \mathcal{O}(\epsilon^2)$, and substitution of this term into (2.5) leads to an error of size $\mathcal{O}(\epsilon^3)$ (terms of this size were disregarded in the derivation). Use of this new dimensionless pressure variable, Q, allows for the treatment of boundary and interface conditions. The boundary conditions enforced during simulation are as follows. The ocean surface is considered a pressure-release boundary, $Q = 0$ at $z = 0$, and the medium ahead of the computational domain is considered quiescent, $Q = 0$ at $x = x_N$. These conditions presume that the acoustic pulse is propagating in a calm ocean devoid of any surface waves.

In basic ocean environment models, the seafloor is often considered a rigid boundary to simplify calculations. In such a case, the Neumann boundary condition $\frac{\partial Q}{\partial z} = 0$ is applied at the bottom boundary. To implement this boundary condition with the finite-difference scheme presented in the previous section, the bottom boundary is placed just below the last row of the computational domain, between row M and artificial row $M+1$. The grid points on row $M+1$ represent non-physical values since they lay outside of the domain. Now, the Neumann boundary condition is applied to grid points on either side of the bottom boundary as shown in Figure 2.1. The discrete finite-difference boundary condition is given by

$$\frac{Q_{M+1} - Q_M}{\Delta z} = 0, \tag{2.26}$$

where Q_{M+1} represents a non-physical value. This equation is solved, trivially, giving $Q_{M+1} = Q_M$. This equality is applied to equation (2.23) with $j = M$ which in turn leads to a modified $\mathbf{A}$ matrix. The M^{th} row of $\mathbf{A}$ becomes

$$\mathbf{A}_M = \begin{bmatrix} 0 & \cdots & 1 & -1 \end{bmatrix}, \tag{2.27}$$

and the rest of the finite-difference scheme remains the same.

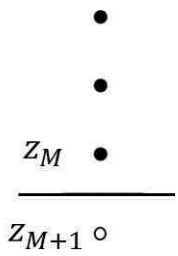

Figure 2.1: Grid used for applying bottom boundary condition. The empty circle represents the non-physical grid point.

2.3.3 Penetrable Ocean Bottom

Although the rigid seafloor model is computational efficient, it does not adequately describe realistic ocean environments where sound is able to travel into and out of ocean bottom sediment layers. For the standard NPE model, sediment layers in the ocean bottom are treated as fluids with densities and sound speeds that differ from those of the water column. This leads to the approximation that shear wave propagation in the seafloor is negligible (nonelastic material): this is true for unconsolidated soils which are often found in the seabed, but this is not necessarily accurate for dense bottom media.

Two interface conditions that need to be satisfied at the fluid-fluid interface at the ocean bottom are continuity of pressure and continuity of normal particle speed. Mathematically, these conditions are given by

$$Q_u = Q_l, \tag{2.28a}$$

$$\frac{1}{\rho_u}\frac{\partial Q_u}{\partial z} = \frac{1}{\rho_l}\frac{\partial Q_l}{\partial z}, \tag{2.28b}$$

where the subscripts u and l denote the upper and lower fluids. To implement these conditions with the finite-difference scheme, the interface is placed between rows j and $j+1$ of the the computational domain. The interface conditions are applied to grid points on either

side of the interface as shown in Figure 2.2. This results in discrete formulae

$$\frac{Q_{u_j} + Q_{u_{j+1}}}{2} = \frac{Q_{l_j} + Q_{l_{j+1}}}{2} \tag{2.29a}$$

$$\text{and} \qquad \frac{1}{\rho_u}\frac{Q_{u_{j+1}} - Q_{u_j}}{\Delta z} = \frac{1}{\rho_l}\frac{Q_{l_{j+1}} - Q_{l_j}}{\Delta z}, \tag{2.29b}$$

where $Q_{u_{j+1}}$ and Q_{l_j} are termed non-physical values. The formulas in (2.29) correspond to a set of two equations for two unknowns, the non-physical values. Solving for the unknowns gives

$$Q_{u_{j+1}} = \frac{\rho_l - \rho_u}{\rho_l + \rho_u} Q_{u_j} + \frac{2\rho_u}{\rho_l + \rho_u} Q_{l_{j+1}} \tag{2.30a}$$

$$\text{and} \qquad Q_{l_j} = \frac{2\rho_l}{\rho_l + \rho_u} Q_{u_j} + \frac{\rho_u - \rho_l}{\rho_l + \rho_u} Q_{l_{j+1}}. \tag{2.30b}$$

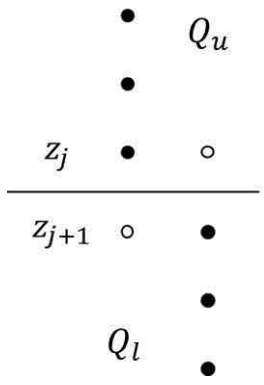

Figure 2.2: Grid used for applying interface conditions. The empty circles represent non-physical grid points.

Applying these terms to Eqn. (2.23) for rows j and $j+1$ leads to a modified $\mathbf{A}$ matrix. The rows associated with the fluid-fluid interface become

$$\mathbf{A}_j = \begin{bmatrix} 0 & \cdots & 1 & -\left(2 - \frac{\rho_l - \rho_u}{\rho_l + \rho_u}\right) & \frac{2\rho_u}{\rho_l + \rho_u} & \cdots & 0 \end{bmatrix} \tag{2.31}$$

and

$$\mathbf{A}_{j+1} = \begin{bmatrix} 0 & \cdots & \frac{2\rho_l}{\rho_l+\rho_u} & -\left(2 - \frac{\rho_u-\rho_l}{\rho_l+\rho_u}\right) & 1 & \cdots & 0 \end{bmatrix}. \tag{2.32}$$

Again, the finite-difference scheme is executed in a similar manner as described previously, except now there are multiple σ values corresponding to the various fluid layers.

Artificial Absorbing Layer The penetrable ocean bottom allows for the possibility of energy to propagate to the base of the computational domain. Therefore, an artificial absorbing layer is needed to damp out any energy near the bottom of the computational grid to prevent any unrealistic reflections. The absorbing layer is numerically implemented by adding a $-R/\tau$ term to Eqn. (2.5) (or, equivalently, adding a $-Q/\tau$ term to Eqn. (2.25)). The numerical damping coefficient τ varies as a function of depth and is defined solely in the artificial absorbing region, $z_{damp} \leq z \leq z_M$, where z_{damp} is the depth at which the artificial absorbing layer begins. After the damping term is added to the NPE, the finite-difference scheme given in Eqn. (2.24) now becomes

$$(\mathbf{I} - \sigma\mathbf{A})\vec{R}_i^{n+1} = \left(\mathbf{I} + \sigma\mathbf{A} - \frac{\Delta t}{\tau(z)}\mathbf{I}\right)\vec{R}_i^n + 2\sigma \sum_{k=i+1}^{N-1} (\mathbf{A}(\vec{R}_k^n + \vec{R}_k^{n+1})). \tag{2.33}$$

From Eqn. (2.33) it is inferred that the $\Delta t/\tau$ term should disappear near the beginning of the artificial absorbing layer, $z = z_{damp}$ and it should go to unity near the bottom of the computational domain at $z = z_M$. This ensures no damping at the beginning of the absorbing layer and complete damping at the bottom of the computational grid. The numerical damping coefficient $\tau(z)$ can be any continuous, smooth function that satisfies $\Delta t/\tau = 0$ at $z = z_{damp}$ and $\Delta t/\tau = 1$ at $z = z_M$. The function used throughout this work is of the form

$$\tau(z) = \frac{C}{(z - z_{damp} + 1)^\alpha}, \tag{2.34}$$

where C is an arbitrary large number and the exponent α is a value that satisfies

$$(z_M - z_{damp} + 1)^{\alpha} = \frac{C}{\Delta t}. \tag{2.35}$$

This function provides adequate damping near the bottom of the domain while maintaining a smooth transition from the non-damped region to the artificial absorbing layer.

2.4 Thesis Introduction

The NPE in its current form treats diffraction, refraction, and nonlinear steepening of weak shocks. Geometric spreading loss is easily implemented by scaling computed results or with the addition of a loss operator to (2.5) (McDonald & Orris, 1998). Viscous dissipation can be implemented by appending an addition term onto the equation: a spatial-derivative term for quadratic frequency dependence or a Cauchy-integral term for linear frequency dependence (Castor *et al.*, 2004). Chapter 3 discusses dissipative sediments in more detail. The NPE is naturally able to handle depth-dependence, and has been shown to handle range-dependence characterized by constant sloped ocean bottoms (Maestas *et al.*, 2014). Recent research has seen adjustments made to the NPE that allow for range-dependence in the form of a variable sound speed profile (McDonald & Piacsek, 2011). Despite these advancements and additional operators, the NPE is still not able to treat most realistic ocean environments. Arbitrary frequency dependence is not treated with any current model, but is needed to describe typical oceanic sediments. All of the models thus far have only considered fluid media, but seafloors can also comprise of condensed material where elastic effects become important. These deficiencies are addressed in the following chapters.

CHAPTER 3

DISPERSIVE SEDIMENTS

The current nonlinear progressive wave equation (NPE) model does not take into account frequency-dependent sediment attenuation, a feature necessary for accurately describing sound propagation into and out of the ocean sediment. These attenuating, dispersive sediments are naturally captured with linear, frequency-domain solutions through use of complex wavespeeds, but a comparable treatment is nontrivial in the time-domain. Recent developments in fractional loss operator methods allow for frequency-dependent loss mechanisms to be applied in the time-domain providing physically realistic results (Prier & Holm, 2011). Using these approaches, the governing equations used to describe the NPE are modified to use fractional derivatives in order to develop a fractional NPE. The updated model is benchmarked against a Fourier-transformed parabolic equation solution for the linear case using various sediment attenuation factors. The fractional NPE is then used to investigate the effects of attenuation on shock wave propagation.

3.1 Introduction

The nonlinear progressive wave equation (NPE), first introduced by McDonald and Kuperman, describes nonlinear acoustic pulse propagation in ocean waveguides (McDonald & Kuperman, 1987). It accurately handles nonlinear steepening and is useful in simulating underwater shock propagation when the pressure levels are sufficiently low to be considered as a weak shock (Kamegai & White, 1994). However, prior implementations of the NPE have not been capable of modeling propagation through lossy sediments which are frequency-dependent. In this work, the NPE is adapted to treat lossy sediments that exhibit frequency power law dependency using a fractional Laplacian approach (Chen & Holm, 2004). The fractional NPE is then used to quantify shock decay for different levels of attenuation, and the model is applied to a physically realistic buried explosive study.

Typical ocean environments contain sediments (sand, gravel, clay, etc.) that absorb acoustic energy in the form of heat in a process known as thermoviscous absorption. This energy absorption is quantified using an attenuation coefficient, α, which is defined by

$$A = A_0 e^{-\alpha x} \tag{3.1}$$

for a plane wave. Energy loss is dependent on the material properties of the particles, the properties of the fluid, and the structure of the particle assemblages, and each process is significant in different frequency ranges (Stoll & Bryan, 1970). Experiments by Stoll (Stoll, 1985), Hampton (Hampton, 1967), and others ((Bowles, 1997), (Buchan *et al.*, 1967), and (Anderson & Blackman, 1971)) have shown that sediment attenuation obeys a power law dependence on frequency, and, as such, the attenuation factor α can be described by

$$\alpha = \alpha_0 |\omega|^\gamma, \tag{3.2}$$

where α_0 is the absorption coefficient in $\mathrm{Np(rad/s)^{-\gamma}m^{-1}}$ and ω is the angular frequency in rad/s. The value of the power law exponent γ is material specific and typically exists in the range $0 \leq \gamma \leq 2$ (Szabo, 1994). Experiments in the references above provide typical values for α_0 and γ.

Linear frequency dependence ($\gamma = 1$) is naturally applied in frequency-domain models with the use of a complex wave speed, and nonlinear frequency dependence is easily implemented using simple conversions (Collis *et al.*, 2007b). However, it is not possible to use frequency-domain models to analyze underwater shock propagation problems because the nonlinearity causes coupling between wave energy at different frequencies. In the time-domain, frequency-dependent attenuation is more difficult. One method for this is the multiple relaxations approach, where thermodynamic and constitutive relations are used to derive a causal wave equation with N relaxation processes (Nachman *et al.*, 1990). The number of relaxation processes and each processes' relaxation time and compressibility can be adjusted

so that the frequency dependence fits any arbitrary power law, but the resulting equation is valid only over narrow frequency bands or the number of assumed relaxation mechanisms N must be large (Yang & Cleveland, 2005).

Another set of methods that is mathematically similar to multiple relaxations is the fractional derivative approach (Holm & Näsholm, 2011). These methods use time or space fractional operators to describe loss in a wave equation. Space fractional models such as those based on the fractional Laplacian have been shown to be applicable to many types of wave equations and have a straightforward numerical implementation (Chen & Holm, 2004) (Treeby & Cox, 2010). Also, it has recently been shown that the fractional Laplacian models are low frequency approximations of the fractional Kelvin-Voigt wave equation and the more general fractional Zener wave equation and thus have physical justification (Holm & Näsholm, 2014). The fractional Laplacian approach is chosen for this work since it is easily applied to the existing NPE models. Such a method has already been applied to the KZK equation (Chen & Holm, 2002) which is similar in nature to the NPE. However, the KZK solution is not as suitable for long-range shock propagation because the numerical schemes used in NPE calculations more accurately capture shock.

The approach is as follows: the thermoviscous NPE model first introduced by Too and Lee (Too & Lee, 1995) is adapted following the methodology of Chen and Holm (Chen & Holm, 2004) to yield an updated fractional NPE. The updated model is benchmarked, for the linear case, against a Fourier transformed parabolic equation (PE) solution. The model is then used to study two physically relevant problems: the effect of attenuation on shock decay and the effect of nonlinear frequency dependent attenuation in the sediment layer on shock propagation for a buried explosive study.

3.2 The Fractional Nonlinear Progressive Wave Equation

Assuming a fluid that is viscous and initially quiescent, Too and Lee derived a nonlinear wave equation including a thermoviscous loss operator (Too & Lee, 1995). The equation is

derived from conservation of mass and momentum, an equation of state, and a heat transfer equation to give

$$\frac{\partial^2}{\partial t^2}Q - \zeta\frac{\partial}{\partial t}\nabla^2 Q = \nabla^2(c^2 Q) + \beta\frac{\partial^2}{\partial t^2}Q^2, \tag{3.3}$$

where β is the coefficient of nonlinearity, c is the spatially variable sound speed, $Q = p'/\rho_0 c_0^2$ is a nondimensional pressure variable (p' is an overpressure value), and ζ is the sound diffusivity which is defined as

$$\zeta = \left[\eta + \frac{4}{3}\mu + \kappa\left(\frac{1}{c_v} - \frac{1}{c_p}\right)\right]\frac{1}{\rho_0}, \tag{3.4}$$

where η is the bulk viscosity, μ is the shear viscosity, and κ is the thermal conductivity, c_v is the specific heat per unit mass at constant volume, c_p is the specific heat per unit mass at constant pressure, and ρ_0 is the density. If the sound speed is assumed to be a constant c_0, equation (3.3) can be rearranged to give

$$\nabla^2 Q = \frac{1}{c_0^2}\frac{\partial^2}{\partial t^2}(Q - \beta Q^2) + \frac{\zeta}{c_0^2}\frac{\partial}{\partial t}(-\nabla^2 Q). \tag{3.5}$$

Equation (3.5) is referred to as the nonlinear thermoviscous wave equation because it is similar in form to the linear thermoviscous wave equation ((Blackstock, 1967), (Lighthill, 1980), and (Pierce, 1989)):

$$\nabla^2 p = \frac{1}{c_0^2}\frac{\partial^2 p}{\partial t^2} + \frac{\zeta}{c_0^2}\frac{\partial}{\partial t}(-\nabla^2 p), \tag{3.6}$$

where p is the pressure and ζ is the same sound diffusivity. The last terms in Eqs. (3.5) and (3.6) represent an attenuation effect. This attenuation term in (3.3) and (3.5) is now generalized so the equation obeys an arbitrary frequency-dependent power law using a methodology Chen and Holm used to treat the linear equation (3.6) (Chen & Holm, 2004).

Following the approach taken by Chen and Holm (Chen & Holm, 2004), the nonlinear thermoviscous wave equation is generalized to a fractional form. The variable sound speed form of the equation is used in order to allow for spatial variations in medium properties.

Equation (3.3) is generalized to

$$\nabla^2(c^2Q) = \frac{\partial^2}{\partial t^2}(Q - \beta Q^2) + 2\alpha_0 c^{1+\gamma}\frac{\partial}{\partial t}(-\nabla^2)^{\gamma/2}Q, \tag{3.7}$$

where $0 \leq \gamma \leq 2$ and the term $(-\nabla^2)^{\gamma/2}$ represents a fractional operator, specifically the fractional Laplacian. The fractional Laplacian is often interpreted using its inverse Fourier transform:

$$F_-\{(-\nabla^2)^{s/2}\phi\} = k^s\Phi, \quad 0<s<2 \tag{3.8a}$$

$$(-\nabla^2)^{s/2}\phi = F_-^{-1}\{k^s\Phi\} = \frac{1}{2\pi}\int_\Omega \Phi k^s e^{ik\mathbf{x}}\mathrm{d}k \tag{3.8b}$$

for the wavenumber k. A more detailed formulation of the fractional Laplacian is provided in Appendix A. From Eq. (3.7) it is observed that setting $\gamma = 2$ and $\alpha_0 = \zeta/2c^3$ leads to the original, square frequency dependent nonlinear thermoviscous wave equation, (3.3). Setting $\gamma = 0$ leads to the nonlinear damped wave equation (telegrapher equation) with a damping coefficient of $2\alpha_0/c$.

In an attempt to derived the dispersion relation for (3.7), the 1-D case is considered:

$$\frac{\partial^2}{\partial z^2}(c^2Q) = \frac{\partial^2}{\partial t^2}(Q - \beta Q^2) + 2\alpha_0 c^{1+\gamma}\frac{\partial}{\partial t}\left(-\frac{\partial^2}{\partial z^2}\right)^{\gamma/2}Q, \tag{3.9}$$

for z an arbitrary spatial variable. Generalization to higher spatial dimensions is not lost with the use of the 1D equation due to the properties of the Laplacian and fractional Laplacian (Chen & Holm, 2004).

Substituting a plane wave solution $Q = \hat{Q}e^{i(\tilde{k}z-\omega t)}$ where $\tilde{k}$ is the complex wavenumber into (3.9) yields the following dispersion relation

$$\tilde{k}^2 = \frac{\omega^2}{c_0^2} - 4\beta\frac{\omega^2}{c_0^2}Q + 2i\omega\alpha_0 c_0^{\gamma-1}\tilde{k}^\gamma, \tag{3.10}$$

for a given c_0 and α_0 which are assumed to be constants. A constant sound speed is justified in

observing that it is locally constant over the length scale for which absorption in the sediment takes place; even at a discontinuity in material sound speed this assumption holds due to restrictions held on the numerical time step (CFL condition) that allows only a fraction of the wave energy to transfer between cells so that attenuation at a grid point is most sensitive to the local constant sound speed at that point (Graves, 1996). Here the fractional Laplacian of the exponential function comes implicitly from the Fourier transform relation (3.8) (Treeby & Cox, 2010). The wavenumber is shown to have an amplitude dependence that is a direct result of the nonlinear form of the equation. Splitting the wavenumber into its real and complex parts $\tilde{k} = k_r + ik_i$ gives

$$k_r^2 + 2ik_rk_i - k_i^2 = \frac{\omega^2}{c_0^2} - 4\beta\frac{\omega^2}{c_0^2}Q + 2i\omega\alpha_0 c_0^{\gamma-1}(k_r + ik_i)^\gamma. \tag{3.11}$$

The real part of the wavenumber dictates the propagating part of the wave and can be written as $k_r = \omega/c_P$ where c_P is the frequency dependent phase velocity. The imaginary part of the wavenumber dictates absorption and is equal to the attenuation coefficient, $k_i = \alpha$. Now, one assumes that the attenuation is considerably smaller than the real part of the wavenumber, $k_i \ll k_r$. This assumption is valid for most ocean sediments where attenuation is small even for low frequencies found in explosive broadband sources. The smallness approximation allows for a binomial expansion to be used for the $(k_r + ik_i)^\gamma$ term. Retaining the first two terms of the expansion leads to

$$k_r^2 + 2ik_rk_i - k_i^2 = \frac{\omega^2}{c_0^2} - 4\beta\frac{\omega^2}{c_0^2}Q + 2i\omega\alpha_0 c_0^{\gamma-1}k_r^\gamma(1 + i\gamma k_i/k_r). \tag{3.12}$$

Collecting the real and imaginary terms gives the following equations

$$\begin{aligned} k_r^2 - k_i^2 - \frac{\omega^2}{c_0^2}(1 - 4\beta Q) + 2\alpha_0\omega c_0^{\gamma-1}\gamma k_r^{\gamma-1}k_i = 0 \qquad &\text{(real)} \\ k_rk_i - \alpha_0\omega c_0^{\gamma-1}k_r^\gamma = 0 \qquad &\text{(imaginary).} \end{aligned} \tag{3.13}$$

Rearranging the imaginary term gives

$$k_r^{\gamma-1} = \frac{k_i}{\alpha_0 \omega c_0^{\gamma-1}}, \tag{3.14}$$

which when substituted into the real term equation yields

$$k_r^2 = \frac{\omega^2}{c_0^2}(1 - 4\beta Q) + (1 - 2\gamma)k_i^2. \tag{3.15}$$

Using the smallness approximation $k_i \ll k_r$ the real part of the wavenumber is written as

$$k_r \approx \frac{\omega}{c_0}\sqrt{1 - 4\beta Q}. \tag{3.16}$$

Finally, substituting (3.16) into the imaginary term equation produces

$$k_i = \alpha_0 \omega c_0^{\gamma-1} k_r^{\gamma-1} = \alpha_0 \omega^\gamma \left(\sqrt{1 - 4\beta Q}\right)^{\gamma-1}, \tag{3.17}$$

which reduces to

$$\alpha = \alpha_0 \omega^\gamma (1 - 4\beta Q)^{(\gamma-1)/2}. \tag{3.18}$$

For weak shocks $\beta Q \ll 1$ and $\alpha \approx \alpha_0 |\omega|^\gamma$ which makes this approach valid for the NPE as it is only able to treat weak shock. For strong shocks, this method captures linear frequency dependence but breaks down for other values of $\gamma \neq 1$.

Equation (3.7) is now recast into a moving domain advancing in range at a speed of c_0. This is done through the use of a Lagrangian derivative in time,

$$\frac{\partial}{\partial t} = \frac{D}{Dt} - c_0 \frac{\partial}{\partial x}. \tag{3.19}$$

It is assumed the sound speed of the medium can vary slightly in space according to $c = c_0 + c_1(x, y, z)$, where c_0 is the constant average sound speed of the medium and c_1 is a small

spatial deviation from that average. Applying Eq. (3.19) and the variable sound speed term to Eq. (3.7) and expanding gives

$$\left(\frac{\partial^2}{\partial x^2}+\frac{\partial^2}{\partial y^2}+\frac{\partial^2}{\partial z^2}\right)(c_0^2+2c_0c_1+c_1^2)Q=\left(\frac{D^2}{Dt^2}-2c_0\frac{D}{Dt}\frac{\partial}{\partial x}-c_0^2\frac{\partial^2}{\partial x^2}\right)(Q-\beta Q^2) \quad (3.20)$$
$$-2\alpha_0(c_0+c_1)^{1+\gamma}\left(\frac{D}{Dt}-c_0\frac{\partial}{\partial x}\right)\left(\frac{\partial^2}{\partial x^2}+\frac{\partial^2}{\partial y^2}+\frac{\partial^2}{\partial z^2}\right)^{\gamma/2}Q.$$

Following the narrow angle assumption used by McDonald and Kuperman (McDonald & Kuperman, 1987), it is assumed that the x direction derivative is considerably more dominant than the y and z direction derivatives. Also, the following terms are considered small: D/Dt - the evolution of the wave within the moving domain is small compared to the velocity of the grid; c_1 - the spatial variation in the sound speed is considered small compared to c_0; βQ^2 - the nonlinearity is considered weak; and α_0 - the attenuation is small. Retaining only the dominant terms in Eq. (3.20) gives

$$\frac{\partial^2}{\partial x^2}\left[(c_0^2+2c_0c_1)Q\right]+c_0^2\left(\frac{\partial^2}{\partial y^2}+\frac{\partial^2}{\partial z^2}\right)Q= \quad (3.21)$$
$$-2c_0\frac{D}{Dt}\frac{\partial}{\partial x}Q+c_0^2\frac{\partial^2}{\partial x^2}(Q-\beta Q^2)+2\alpha_0c_0^{2+\gamma}\left(\frac{\partial}{\partial x}\right)^{1+\gamma}Q.$$

Rearranging, dividing through by c_0, and differentiating with respect to x leads to the final form of the fractional NPE:

$$\frac{DQ}{Dt}=-\frac{\partial}{\partial x}\left[c_1Q+\frac{c_0\beta}{2}Q^2\right]-\frac{c_0}{2}\int_{x_f}^{x}\left(\frac{\partial^2}{\partial y^2}+\frac{\partial^2}{\partial z^2}\right)Q\,\mathrm{dx}+\alpha_0c_0^{1+\gamma}\left(\frac{\partial^2}{\partial x^2}\right)^{\gamma/2}Q, \quad (3.22)$$

where x_f is a point taken ahead of the pulse in the quiescent medium where $Q=\partial Q/\partial x=0$. The overall form of the equation is the same as the orginal NPE, but with the addition of the fractional thermoviscous loss operator. Boundary and interface conditions conditions remain the same as for the original NPE and are given in Chapter 2.

The following section provides details on numerical procedures used to evaluate the NPE. Results of this model are compared to those of a fluid PE solution for a range-independent case; the nonlinear capabilities of the NPE are suppressed.

3.3 Numerical Implementation and Linear Benchmark

The fractional NPE is implemented numerically using an operator splitting approach. Each operation of the governing equation is calculated independently in three successive steps:

$$\begin{aligned} Q_{i,j}^{n+\frac{1}{3}} &= \mathcal{L}_1 Q_{i,j}^{n} \\ Q_{i,j}^{n+\frac{2}{3}} &= \mathcal{L}_2 Q_{i,j}^{n+\frac{1}{3}} \\ Q_{i,j}^{n+1} &= \mathcal{L}_3 Q_{i,j}^{n+\frac{2}{3}}, \end{aligned} \tag{3.23}$$

where the operations are given by

$$\mathcal{L}_1 = -\frac{\partial}{\partial x}\left[c_1 Q + \frac{c_0\beta}{2}Q^2\right] \tag{3.24a}$$

$$\mathcal{L}_2 = \alpha_0 c_0^{1+\gamma}\left(\frac{\partial^2}{\partial x^2}\right)^{\gamma/2} Q \tag{3.24b}$$

$$\mathcal{L}_3 = -\frac{c_0}{2}\int_{x_f}^{x}\left(\frac{\partial^2}{\partial z^2}\right) Q \,\mathrm{dx}. \tag{3.24c}$$

The $\mathcal{L}_1$ operation represents refraction and nonlinear steepening, and it is treated using a flux-corrected transport (FCT) algorithm. The $\mathcal{L}_2$ operation representing sound attenuation is treated using a finite-difference (FD) approximation and a Crank-Nicolson scheme to integrate in time. The fractional operator is handled using a singular value decomposition of the FD operator matrix:

$$K^{\gamma/2} = \Phi^T\left(\Sigma\lambda_i^2\right)^{\gamma/2}\Phi, \tag{3.25}$$

where K represents the finite-difference matrix operator that approximates $\partial^2/\partial x^2$. The $\mathcal{L}_3$ operation represents diffraction. Note that the y derivative term has been neglected as only two dimensions are considered here. The diffraction operator is treated using FD approximations for the spatial derivative, a trapezoid rule approximation for the integral, and a Crank-Nicolson scheme to integrate in time.

3.3.1 Mesh Convergence Study

Prior to benchmarking the fractional model, it is necessary to determine what effect the resolution of the computational grid has on the solution when applying the new fractional loss term. A mesh convergence study is presented here to investigate the convergence rate of the numerical solution. The problem used for the study is the evolution of a 1D square shock wave in a dispersive sediment. The sediment has a density of 1500 kg/m^3 and a sound speed of 1650 m/s. Three different cases are presented for attenuation: case A, $\alpha^{(\lambda)} = 0.1$ dB/λ, case B, $\alpha^{(\lambda)} = 1.0$ dB/λ, and case C, $\alpha^{(\lambda)} = 10.0$ dB/λ, where λ is the acoustic wavelength; these terms are related to (3.2) by

$$\alpha_0 = \frac{\alpha^{(\lambda)}}{40\pi c \log(e)}, \quad \gamma = 1. \tag{3.26}$$

The initial waveform used in the study is a 10 m long square shock with an amplitude of 100 MPa as seen in Figure 3.1 below. The 1D computational domain is 50 m long and the grid spacing is set to 1.0, 0.5, 0.25, and 0.125 m to allow for 50, 100, 200, and 400 points in the mesh, respectively. The time step is set to 0.01 ms and the coefficient of nonlinearity β is set to 3.5. The shock is propagated for a total of 100 ms.

The results are given below in Figures 3.2-3.4 and show that solutions are not strongly dependent on the mesh resolution. The rate of convergence is also computed to determine the approximate rate at which the numerical solution converges to the exact solution. The rate is calculated with

$$r = \frac{\log\left(\frac{a_{400} - a_{200}}{a_{200} - a_{100}}\right)}{\log 2}, \tag{3.27}$$

where a here is the L^1 norm of the pressure profiles. The rate of convergence is found to be 1.00 for all cases. This study indicates that relatively accurate results can be obtained using a coarser mesh – a useful fact when analyzing long-range propagation problems.

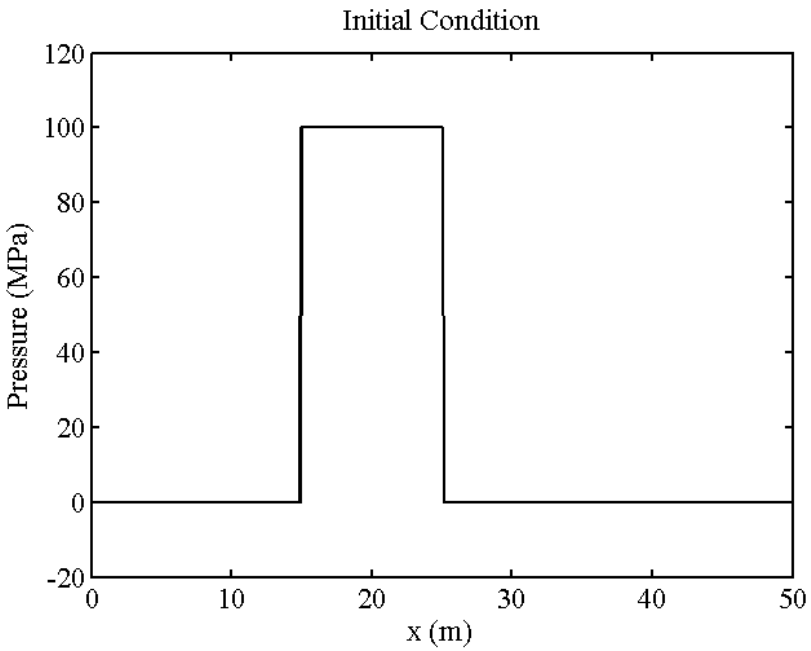

Figure 3.1: Initial condition for mesh convergence study.

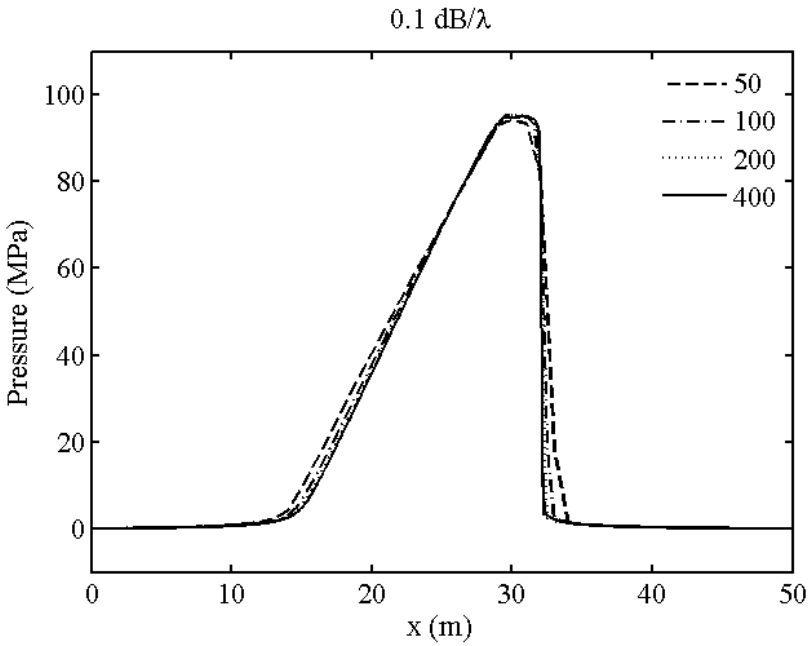

Figure 3.2: Waveform at t = 100 ms for case A.

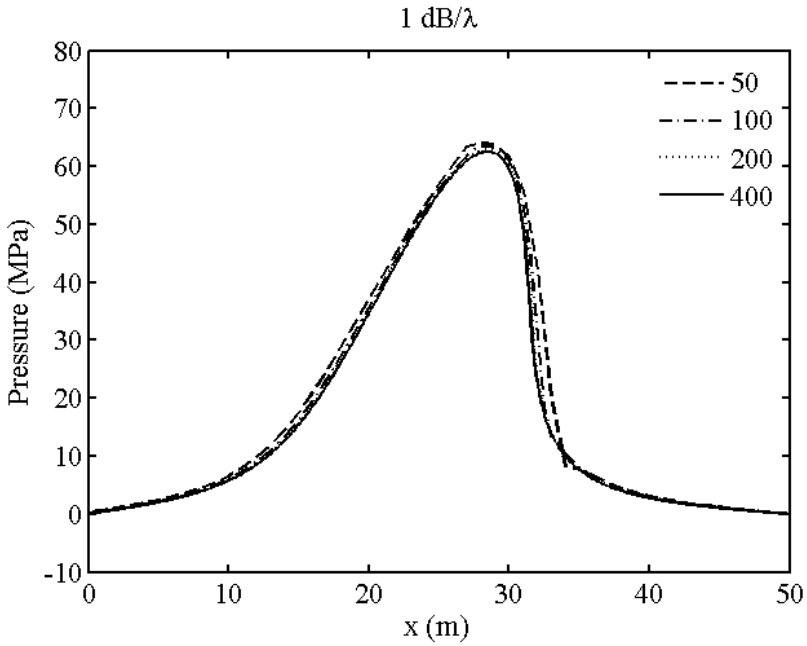

Figure 3.3: Waveform at t = 100 ms for case B.

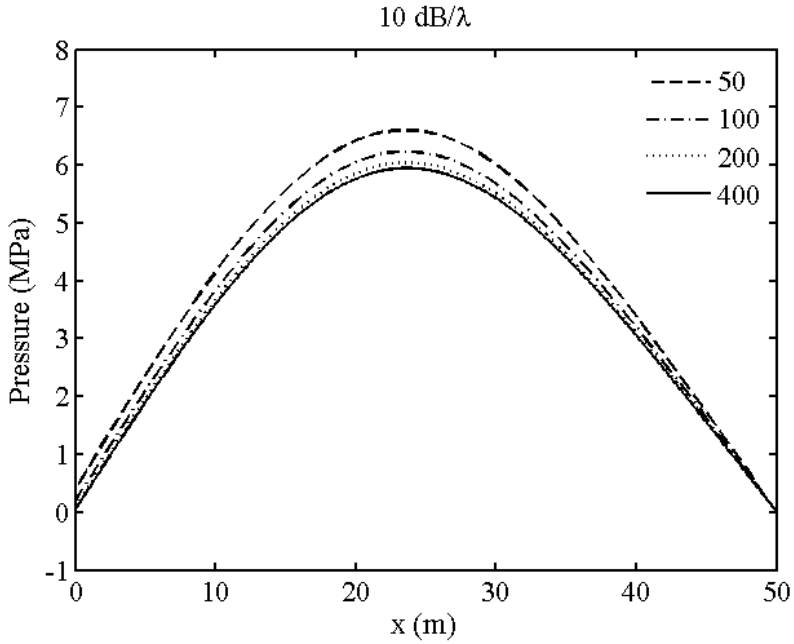

Figure 3.4: Waveform at t = 100 ms for case C.

3.3.2 Linear Benchmark

The fractional NPE solution is benchmarked against a parabolic equation solution for a linear, range-independent case. The parabolic equation model used is the Range-dependent Acoustic Model (RAM) developed at the Naval Research Laboratory by Michael Collins (Collins, 1993a). It is a linear, frequency-domain solution known for producing accurate results in dispersive media using the complex wavespeed approach. As RAM is a frequency-domain model, a Fourier transform is required for solutions in the time-domain, using a discrete Fourier synthesis.

The environment for comparisons is the flat, layered waveguide with a water column depth of 100 m atop an additional 100 m of sediment depth. The water column has a density of 1000 kg/m^3 and a sound speed of 1500 m/s, whereas the sediment has a density of 1500 kg/m^3 and a sound speed of 1650 m/s. Two different cases are presented for attenuation in the sediment layer: case A, $\alpha^{(\lambda)} = 0.1$ dB/λ and case B, $\alpha^{(\lambda)} = 10.0$ dB/λ. Linear frequency dependence allows the standard RAM solution to be used rather than a modified solution. The source is located at $z_s = 50$ m and emits a pulse described by

$$Q(t) = \begin{cases} \sin(\omega_c t) - \frac{1}{2}\sin(2\omega_c t) & \text{for } 0<t<1/f_c \\ 0 & \text{otherwise,} \end{cases} \tag{3.28}$$

where the center frequency f_c is chosen to be 100 Hz. This problem is considered in a moving rectangular computational domain of depth 200 m and width 90 m. The x direction grid spacing is 0.3 m, the z direction grid spacing is 1 m, and the time step is 0.5 ms. Only the linear case is considered and as such the coefficient of nonlinearity β is set to zero. An artificial absorbing layer starting at $z = 190$ m is used to damp out any energy near the bottom of the computational grid to prevent any unrealistic reflections.

To benchmark the NPE solution, the Fourier-transformed PE solution is used to generate the initial waveform for the NPE code, and the simulation marches the domain out to a

final range of 1000 m. The pressure data is saved at four different receiver locations: 500 m and 1000 m in range (both at 20 m and 50 m in depth). The time series data at these receiver locations are then compared to those of the Fourier-transformed RAM solution. The comparisons for the two cases are detailed in the plots of Figure 3.5 and Figure 3.6 which show that the PE (solid curve) and NPE (dashed curve) solutions agree very well. This validates that the fractional NPE accurately captures the dispersive nature of the sediment.

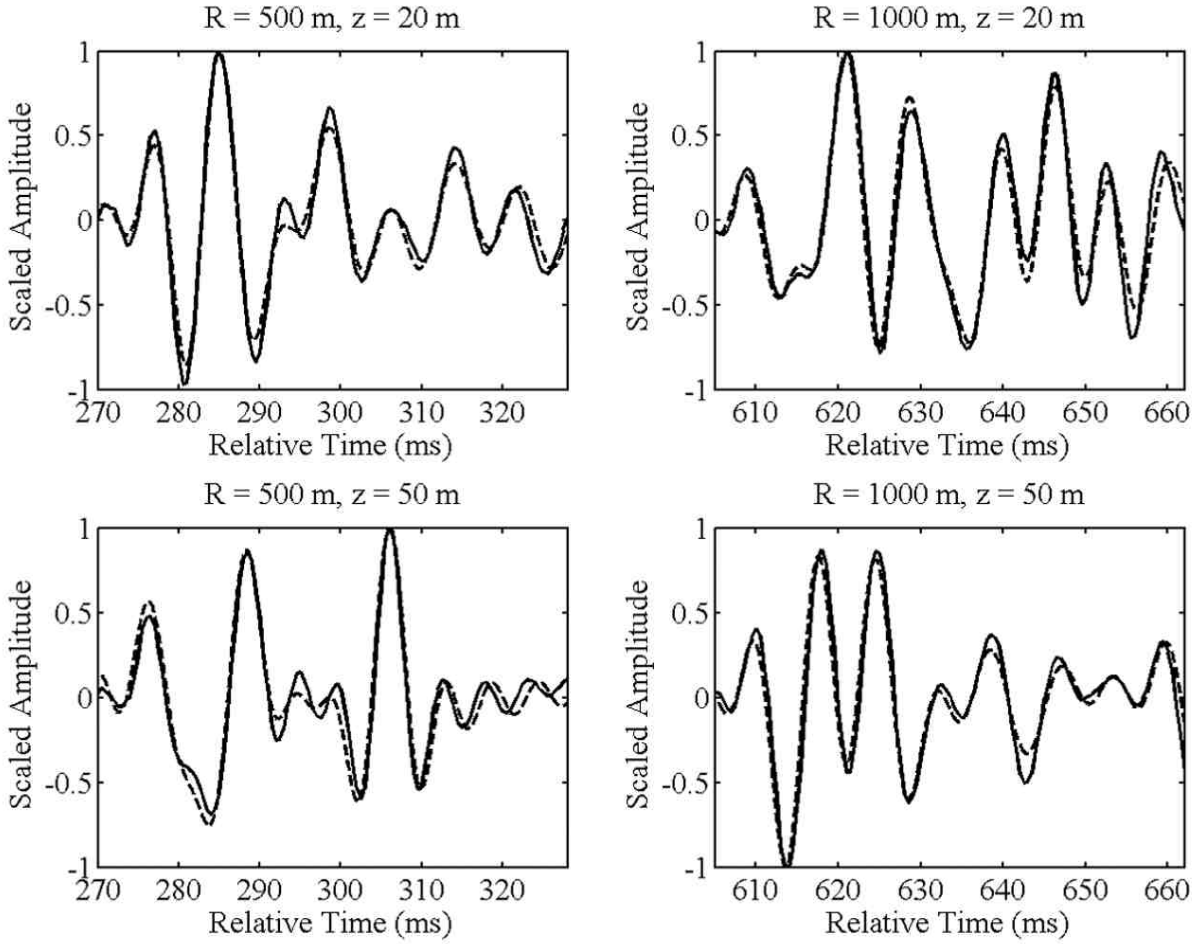

Figure 3.5: Nonlinear progressive wave equation and parabolic wave equation solutions for the case A comparison (attenuation in the sediment, $\alpha^{(\lambda)} = 0.1$ dB/λ). Dashed line: linear PE solution; solid line: linear NPE solution.

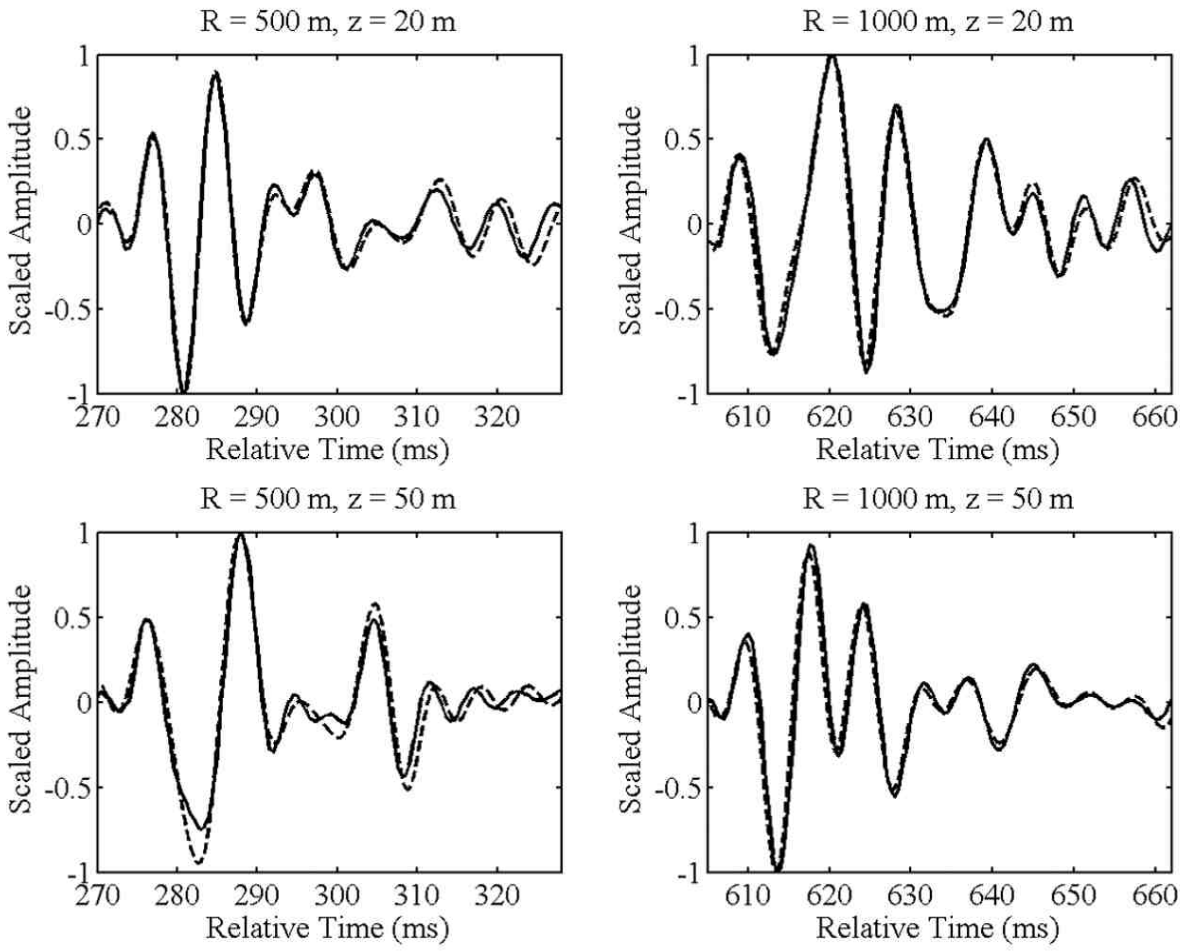

Figure 3.6: Nonlinear progressive wave equation and parabolic wave equation solutions for the case B comparison (attenuation in the sediment, $\alpha^{(\lambda)} = 10$ dB/λ). Dashed line: linear PE solution; solid line: linear NPE solution.

3.4 Shock Propagation in Attenuating Sediments

The benchmarked fractional NPE is used to study physically-relevant problems. Attenuation is of particular importance in shock wave propagation because the high frequency content resides at the shock front, and because attenuation increases with frequency attenuation is expected to have a significant effect on damping sharp shock peaks. Two studies are presented here. The first looks at the effect of attenuation on shock propagation and the decay rate of peak shock pressures for various attenuation rates. The second study examines a real-world application with a buried explosive investigation. The explosive is buried in a dispersive sediment layer that attenuates sound according to a power law empirically fit to experimental measurements. Both studies give useful insight as to the importance of including attenuation in shock propagation models.

3.4.1 Shock Decay Through Lossy Media

This study examines the effect of attenuation on the physical form of a shock wave. The fractional NPE is used to propagate a shock wave through a single dispersive layer whose attenuating properties are varied so as to observe the effect of increasing attenuation. In order to decrease calculation time, a symmetry boundary condition (zero flux condition) is applied to the upper boundary so that only half of the waveform need be calculated. The medium has a density of 1500 kg/m^3, a sound speed of 1650 m/s, and the attenuation is varied: $\alpha^{(\lambda)} = 0.0$, 0.1, 0.5, 1.0, and 5.0 dB/λ, where $\alpha^{(\lambda)}$ is related to the frequency power law via Eq. (3.26). The initial condition is a spherical wave centered at the origin with an exponentially decaying radial profile. The peak pressure of the initial waveform is 100 MPa and is located at a distance of 4.84 m from the source point. Such an initial condition may be typical of a fairly large underwater blast (comparable to the detonation of approximately 500 kg of TNT). This problem is analyzed in a moving window of depth 25 m and width 10 m. The x direction grid spacing is 0.1 m, the z direction grid spacing is 0.2 m, and the time step is 0.06 ms. The use of a small time step is necessary for capturing the shock peak

when the waveform is sampled in time. The coefficient of nonlinearity β is set to 3.5, a value typical for water.

The NPE simulation marches the domain out to a final range of 200 m, and pressure data is saved at $z = 0$ m for various distances down range. Figure 3.7 gives the peak shock pressures versus range for all five attenuation rates. The plot shows that attenuation plays a significant role in shock decay. For the medium with no attenuation (solid line), the overpressure remains at unsafe levels, but for the medium with an attenuation of 5 dB/λ the peak overpressures are well below the acoustic limit. The plot also shows that an increase in attenuation tends to cause a shift from a linear decay rate to a more nonlinear decay.

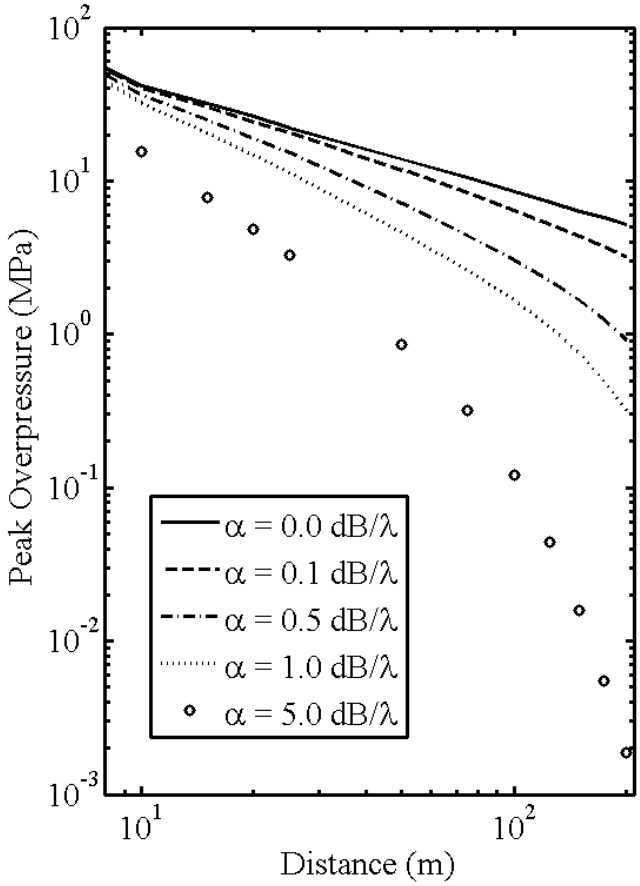

Figure 3.7: Shock wave attenuation study. Peak overpressure values are taken from receivers located at $z = 0$ m (center of the waveform) at various distances down range.

The alteration of the waveform structure is also of interest. Figure 3.8 gives the shock waveforms for each attenuation case for a receiver located at $x = 200$ m, $z = 0$ m. The plot shows that as attenuation increases the shock front slowly smooths out. This result is consistent with the fact that attenuation increases with frequency and thus an absorbing medium will act as a low-pass filter. These results indicate that correct attenuation properties are vital to accurately modeling wave propagation, especially shock wave propagation.

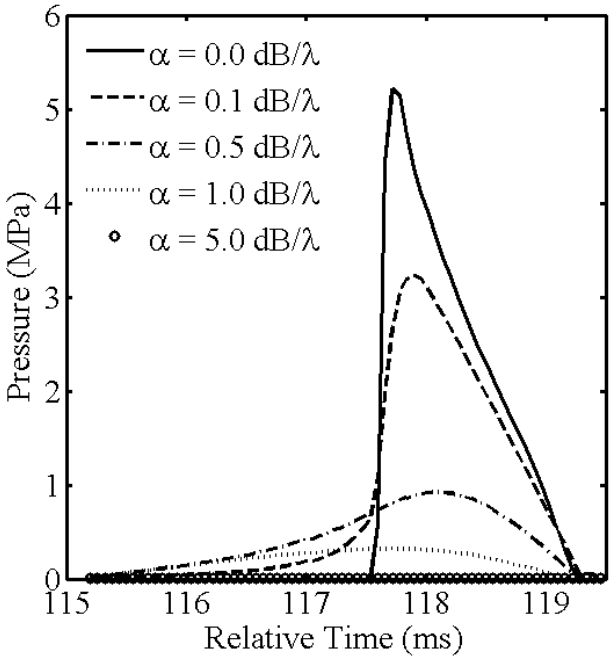

Figure 3.8: Shock waveforms at $x = 200$ m, $z = 0$ m for the shock wave attenuation study. The steep shock front is smoothed out as high frequencies are filtered out.

3.4.2 The Effect of Attenuation on Sediment-borne Blast Wave Propagation

A study is presented here to investigate the effect of attenuated sediments on blast wave propagation when the source is located within the dispersive sediment layer. Such a study is conceivable when considering the effects of underwater demolition on marine life. Accurate modeling of peak shock pressure as well as shock duration are necessary for determining if an underwater blast will have detrimental effects on sea life.

The details of the calculations are as follows: an explosive source is located at a depth of 10 m below mud line above which sits a 25 m water column with constant sound speed and density of $c_w = 1500$ m/s and $\rho_w = 1000$ kg/m^3. The sediment half space lies below the water column and contains the following parameters: $c_b = 2200$ m/s and $\rho_b = 1700$ kg/m^3. Two cases are considered for the sediment attenuation. Zero attenuation is considered in the first case, and for the second case the attenuation obeys a frequency power law presented by Bowles (Bowles, 1997):

$$\alpha(\text{dB/m}) = 2.42 \times 10^{-5} f^{1.12}, \tag{3.29}$$

where $f = \omega/2\pi$. This equation was generated by fitting P-wave attenuation measurements for various fine-grained marine sediments.

The pressure waveform used for the initial condition of the study is given in Figure 3.9(a). This simplified waveform represents the detonation of approximately 100 kg of TNT. The parameters of peak pressure, arrival distance, and shock duration are taken from an NSWC report for underwater explosions (Swisdak, 1978). The frequency spectrum for the initial blast wave is given in Figure 3.9(b), and the plot shows that the signal is broadband with the majority of the energy existing below 5 kHz. The computational grid has a width of 100 m and depth of 70 m, including a 15 m thick artificial absorbing region. The x direction grid spacing is 0.25 m, the z direction grid spacing is 0.25 m, and the time step is 0.0001 s. The coefficient of nonlinearity, β, is set to 3.5.

The blast wave is propagated 200 m down a shallow water waveguide to simulate propagation into the open ocean, and pressure histories are recorded at various depths in the water column (Figure 3.10). The pressure traces show that sediment attenuation has a notable effect on the wave as it propagates. The waveform in the environment with the dispersive sediment is damped by nearly ten times (-20 dB) when compared to the non-dispersive sediment case. The amplified dispersive sediment solution (dashed line) reveals some interesting results: the wave in the dispersive sediment appears to have had the high frequencies filtered out, and it also appears that the pattern phase has remained unaffected. Results of this study

indicate that sediment attenuation plays a pivotal role in buried explosive investigations and cannot be disregarded.

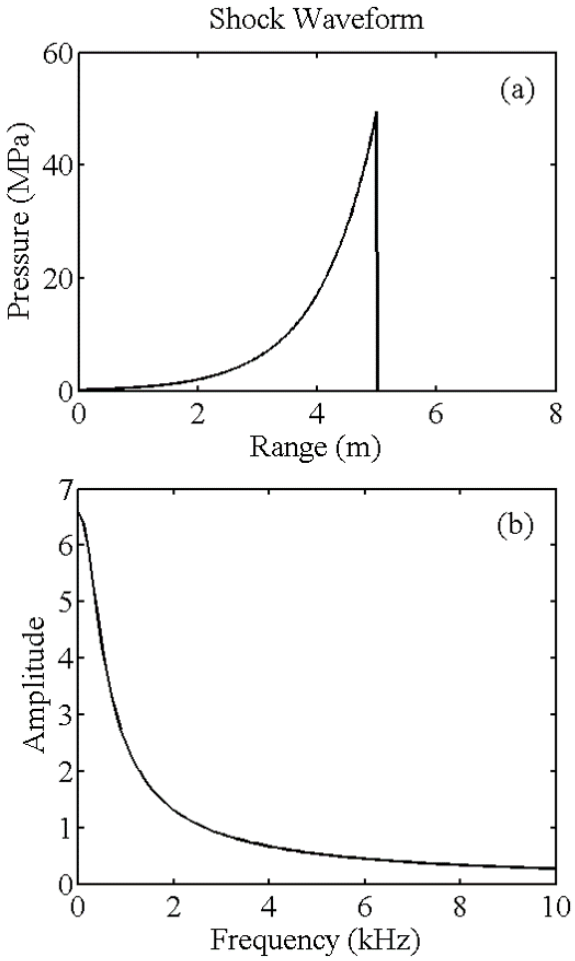

Figure 3.9: Initial pulse used in the thin sediment layer study. Amplitude and duration are representative of a 100 kg TNT blast. (a) Pressure waveform of the initial pulse. (b) Frequency spectrum of the initial pulse.

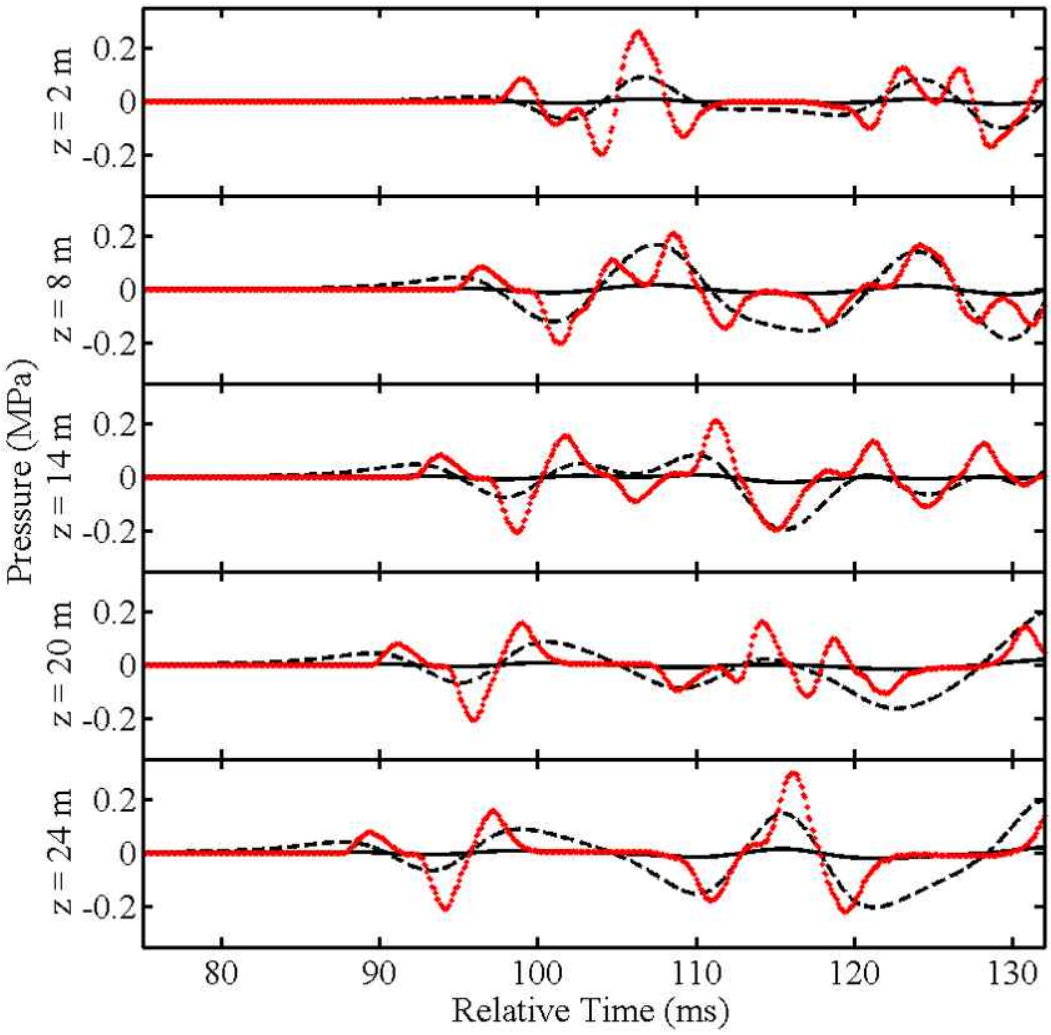

Figure 3.10: Comparison of wave propagation with and without sediment attenuation. Results are taken at a range of 200 m. Solid red markers represent results from an environment that does not include sediment attenuation. The solid black line represents results from an environment in which the sediment attenuation obeys $\alpha(\mathrm{dB/m}) = 2.42 \times 10^{-5} f^{1.12}$. The dashed line represents the same result but amplified by a power of 10.

3.5 Discussion

The thermoviscous NPE of Too and Lee(Too & Lee, 1995) was transformed into a fractional NPE following the methodology of Chen and Holm (Chen & Holm, 2004). The approach assumed that attenuation is small with regard to wavenumber, an assumption valid for most ocean bottom sediments for frequency ranges of interest. The fractional NPE was numerically implemented using an operator splitting approach and the fractional derivative was treated with a singular value decomposition of the FD operator matrix. Comparisons with the Fourier-transformed PE solution for the linear case showed that the fractional NPE model is accurate for a large range of attenuation values typical of ocean sediments. The fractional solution was then applied in two studies: investigating shock decay rates in attenuating media and investigating the effect of sediment attenuation on blast wave propagation. In the first study, results indicated that medium attenuation can greatly affect the form of the shock wave by damping the peak pressure and smoothing the shock front. In the second study, results showed that even a moderate amount of sediment attenuation significantly alters the wave when the source is located in the sediment. Both studies confirmed the form of Eq. (3.2) as high frequency content dissipated faster.

The fractional NPE appears to accurately describe attenuation following an arbitrary frequency power law, but attenuation in sediments often adheres to different frequency power laws at different frequency ranges. For example, attenuation at low frequencies often appears to obey an $\omega^{1.8-2}$ law whereas at higher frequencies (>1kHz) attenuation almost always obeys a nearly linear frequency dependence (Zhou *et al.*, 1987). Therefore, it is not possible for the fractional NPE model to accurately describe attenuation across all frequencies. This leads to complications when simulating shock wave propagation because the majority of the shock's energy exists in the low frequencies but the shock front contains the majority of the high-frequency energy, and it is the shock front that is often of the most interest. It may be possible to develop frequency power laws that approximate the attenuation at very large frequency ranges so that absorption at the frequency bands of interest is captured. It

may also be possible to develop a fractional NPE model with a more complicated dispersion relation that can allow for a more robust frequency dependence. However, given the lack of experimental data for shock propagation through various sediment types, it would be difficult to verify such developments.

CHAPTER 4

WEAKLY-ELASTIC ENVIRONMENTS

In this chapter, a weakly-elastic NPE model is derived by generalizing the original NPE's derivation. The final form of the equation is similar to that of the NPE so implementation is nearly the same as well. It is shown that as the shear modulus μ tends to zero the weakly-elastic model simplifies back to the original form of the NPE. The original NPE model has been benchmarked and verified, so we can assume the weakly-elastic version is valid over some range of $0 \leq \mu \leq \mu^*$, and precisely what μ^* is becomes the crucial question.

4.1 Introduction

Typical ocean bottoms comprise of low-shear speed sediments atop denser elastic media such as rock (Hamilton, 1980). Most ocean acoustic models make the assumption that the low-shear speed layers can be approximated as a fluid, and for many unconsolidated sediments this holds true – the seafloor muds act more as a viscous fluid rather than an elastic solid. The original NPE is no different and assumes the ocean-bottom interface as a fluid-fluid interaction; the validity of this assumption needs to be investigated.

In this work, the derivation of original NPE is modified to describe propagation in an isotropic, linear elastic medium. This material model may not truly represent a saturated granular substance (a poroelastic or viscoelastic model may be more appropriate), but it is the simplest material model capable of capturing the coupling between compressional and shear waves. The isotropic, linear elastic model has been applied to the parabolic equation solution for ocean acoustics with good results (Collins, 1989), (Collis *et al.*, 2009), (Kusel, 2005), (Outing, 2004). However, in this derivation, the shear wave energy is assumed to be a higher order effect compared to the compressional wave energy. This "weak elasticity" assumption allows for a slightly modified form of the NPE, again in terms of a single variable allowing for efficient calculations.

The motivation for developing a weakly-elastic model comes from the lack of models that are capable of treating low shear speed media. Fully elastic models tend to break down as the shear modulus becomes too small and all fluid models are incapable of treating any sort of shear effects (Gilbert, 1998). This leads to the natural question of whether there is a range over which the fluid approximation is invalid and for which a fully elastic model is unable to handle. The model developed in this work provides a necessary framework to investigate this question for pulse propagation problems of interest. One expects this intermediate weakly-elastic range to vary for different environments. For example, upsloping ocean bottoms drive more wave energy into the basement layer therefore weak shear effects would be more pronounced than in the flat bottom case.

The following sections describe the derivation and implementation of a weakly-elastic nonlinear progressive wave equation. This equation is used to study the weak elasticity problem in a simple two layer waveguide (water column atop sediment basement) to determine the range of sediment properties that can be approximated as a fluid for the nonlinear case. A similar analysis for the linear case is not presented here, but the nonlinear results should be an accurate estimate for linear propagation as elastic solids tend to act like a fluid in the direct vicinity of the shock front (elasto-plasticity) (Rinehart, 1975).

4.2 Derivation of the Weakly-elastic Nonlinear Progressive Wave Equation

The weakly-elastic nonlinear progressive wave equation (WENPE) is derived by taking equations of conservation of mass and momentum and combining them, using the adiabatic equation of state, into a set of equations of a single unknown dependent variable. The constitutive relations used in the derivation assume the pulse propagates in a linear elastic medium. The resulting equation, written in terms of one dependent variable, is useful in the area of computational acoustics because it allows for efficient computation when dealing with long-range propagation (greater than 1 km). Further, the WENPE is capable of describing several different physical effects of propagation such as diffraction, refraction, and nonlinear

steepening. The approach used in the derivation presented here is based off an approach used for the original fluid NPE (McDonald *et al.*, 1994). One assumes that the background medium velocity is zero and that the pulse is at sufficiently far distance from the source so that shocks are considered weak enough to neglect thermal effects. Throughout this derivation, the Einstein summation convention, $c_i x_i = \sum c_i x_i = c_1 x_1 + c_2 x_2 + c_3 x_3$, the shorthand spatial derivative notation, $\frac{\partial}{\partial x_i} = \partial_i$ and $\frac{\partial^2}{\partial x_i^2} = \partial_i^2$, and shorthand temporal derivative notation, $\frac{\partial}{\partial t} = \partial_t$, will be employed to make formulas more concise.

4.2.1 Governing Equations

The governing equations for elastic wave propagation are conservation of mass, conservation of linear and angular momentum, the constitutive equation, and the equation of state. An equation for conservation of energy is not included because thermal effects are neglected with the assumption shocks are weak. The equation for conservation of mass (continuity) is given by:

$$\partial_t \rho + \partial_i (\rho v_i) = 0, \tag{4.1}$$

where x_i and t represent the spatial and temporal dimensions ($i = 1, 2, 3$ represent the x, y, and z dimensions, respectively), v_i are the velocity values, and ρ is the density of the medium. The equation for conservation of momentum (the Cauchy momentum equation) is given by:

$$\rho(\partial_t v_i + v_j \partial_j v_i) = \partial_j \sigma_{ij}, \quad i, j = 1, 2, 3 \tag{4.2}$$

where σ_{ij} is the Cauchy stress tensor defined by

$$\sigma_{ij} = \begin{Bmatrix} \sigma_{11} & \sigma_{12} & \sigma_{13} \\ \sigma_{21} & \sigma_{22} & \sigma_{23} \\ \sigma_{31} & \sigma_{32} & \sigma_{33} \end{Bmatrix} = \begin{Bmatrix} \sigma_{xx} & \sigma_{xy} & \sigma_{xz} \\ \sigma_{yx} & \sigma_{yy} & \sigma_{yz} \\ \sigma_{zx} & \sigma_{zy} & \sigma_{zz} \end{Bmatrix}. \tag{4.3}$$

Following the principle of conservation of angular momentum leads to the conclusion that the stress tensor is symmetric, $\sigma_{ij} = \sigma_{ji}$, yielding six unknown stress components. The constitutive equation (Hooke's Law) relating displacements to stresses is

$$\sigma_{ij} = \lambda \delta_{ij} \partial_k u_k + \mu(\partial_j u_i + \partial_i u_j) \tag{4.4}$$

where u_i are displacement values and δ_{ij} is the Kronecker delta function. This equation can be differentiated with respect to time to yield the stress-velocity relations:

$$\partial_t \sigma_{ij} = \lambda \delta_{ij} \partial_k v_k + \mu(\partial_j v_i + \partial_i v_j). \tag{4.5}$$

The pressure, p, is a function of density and specific entropy, s, as seen in the equation of state given by

$$p = p(\rho, s). \tag{4.6}$$

Applying a Taylor series expansion along the isentrope $s = s_0$ yields

$$p = p_0 + \left[\frac{\partial p}{\partial \rho}\right]_{s_0} (\rho - \rho_0) + \frac{1}{2}\left[\frac{\partial^2 p}{\partial \rho^2}\right]_{s_0} (\rho - \rho_0)^2 + \ldots, \tag{4.7}$$

where the zero subscript represents an unperturbed, ambient value. The partial derivatives $(\partial p/\partial \rho)$, $(\partial^2 p/\partial \rho^2)$, etc., in (4.7) are all evaluated at the unperturbed state (ρ_0, s_0); here the assumption is made that the heat generated during the process of compression has an insignificant effect on the relationship of pressure and density. This assumption is valid since thermal effects are not considered in this formulation. Equation (4.7) can be written in a form common to nonlinear acoustics (Hamilton & Blackstock, 1997):

$$p - p_0 = A\left(\frac{\rho - \rho_0}{\rho_0}\right) + \frac{B}{2!}\left(\frac{\rho - \rho_0}{\rho_0}\right)^2 + \frac{C}{3!}\left(\frac{\rho - \rho_0}{\rho_0}\right)^3 + \ldots, \tag{4.8}$$

where

$$A = \rho_0 \left[\frac{\partial p}{\partial \rho}\right]_{s_0}, \tag{4.9}$$

$$B = \rho_0^2 \left[\frac{\partial^2 p}{\partial \rho^2}\right]_{s_0}, \tag{4.10}$$

$$C = \rho_0^3 \left[\frac{\partial^3 p}{\partial \rho^3}\right]_{s_0}. \tag{4.11}$$

In linear acoustic theory, the pressure-density relationship is linear and only the A term in the expansion is conserved. However, under high pressures, density is not linearly related to pressure and higher orders of the expansion are required to relate the variables. In the case of the WENPE, only weak shocks are considered therefore it is sufficient to include only one addition term in the pressure expansion. Now, the pressure-density relationship is assumed to have the form

$$p - p_0 \approx A\left(\frac{\rho - \rho_0}{\rho_0}\right) + \frac{B}{2}\left(\frac{\rho - \rho_0}{\rho_0}\right)^2. \tag{4.12}$$

The value of A for a material is often well understood as there exist robust experimental techniques for defining the pressure-density relationship for low values of pressure. The value of B is much more difficult to obtain. The value of B is known for various fluids and biological tissues (Hamilton & Blackstock, 1997), and is usually reported as the ratio B/A or as what's known as the coefficient of nonlinearity, defined for fluids as $\beta = 1 + B/2A$. Fewer experimental results exist for solids, and the B value must be approximated using a quadratic regression fit of pressure-density plots (if such data is available).

The final governing equation is that relating pressure to stress by

$$p = -\frac{\sigma_{ii}}{3}. \tag{4.13}$$

This equation defines pressure an an average of the normal stresses.

Nonlinear Elastic Wave Equation The equations of conservation of mass and momentum are combined to generate a nonlinear elastic wave equation. First, one differentiates (4.1) with respect to time to give

$$\partial_t^2 \rho = -\partial_i \left(\rho \partial_t v_i + v_i \partial_t \rho \right) \tag{4.14}$$

Substituting equations (4.1) and (4.2) into (4.14) gives the nonlinear elastic wave equation

$$\partial_t^2 \rho = \partial_i \partial_j (\rho v_i v_j - \sigma_{ij}). \tag{4.15}$$

This equation dictates the behavior of the density of the medium as a function of stress and velocity. Analysis of this nonlinear wave equation leads to the WENPE.

4.2.2 Coordinate Transformation

This nonlinear elastic wave equation and other governing equations are recast in a moving frame that tracks the traveling pulse (a Lagrangian approach). This methodology assumes that the majority of the acoustic energy is propagated in the x-direction (the narrow-angle assumption). The new variables (x', y', z', t') will be used to represent the moving-frame coordinate system, while the variables (x, y, z, t) will be representative of the stationary system. The new computational grid will move at a constant speed c_0 (representative of the average sound speed in the medium) in the x-direction. The governing equations are simplified by employing a perturbation-like scaling where the new variables are scaled in order to retain largest terms and discard the small terms. The new variables are given by:

$$\begin{aligned} x' &:= x - c_0 t \\ y' &:= \epsilon^{1/2} y \\ z' &:= \epsilon^{1/2} z \\ t' &:= \epsilon t, \end{aligned} \tag{4.16}$$

where the scaling factor $\epsilon \ll 1$ is used to emphasize the predominance of propagation in the x-direction. The variable t is transformed using a factor of ϵ as opposed to $\epsilon^{1/2}$ in order to weaken the overall dependence of the solution on the new variable t'; it is assumed that the evolution of the pulse (within the moving frame) is small compared to the velocity of the moving frame.

The transformation from Eulerian to Lagrangian coordinates requires the use of a material derivative in time. The material derivative, $D_{t'} = \partial_t + c_0\partial_x$, gives the time derivative while following a specific particle in the fluid. The differential operators are now written as:

$$\begin{aligned} \partial_x &:= \partial_{x'} \\ \partial_y &:= \epsilon^{1/2}\partial_{y'} \\ \partial_z &:= \epsilon^{1/2}\partial_{z'} \\ \partial_t &:= \epsilon D_{t'} - c_0\partial_x = \epsilon D_{t'} - c_0\partial_{x'} \end{aligned} \tag{4.17}$$

The ∂_t term is formulated by rearranging the formula given above for $D_{t'}$; this implies that the effects of the advective term, $c_0\partial_x$, will be carried throughout the derivation. By using the change of variables in (4.16) and differential operators in (4.17), the governing equations can be expressed in terms of the new, moving coordinate system. The equation for conservation of mass now becomes

$$(\epsilon D_{t'} - c_0\partial_{x'})\rho = -\partial_{x'}(\rho v_1) - \epsilon^{1/2}\partial_{y'}(\rho v_2) - \epsilon^{1/2}\partial_{z'}(\rho v_3). \tag{4.18}$$

Using the fact $\sigma_{ij} = \sigma_{ji}$, the nonlinear elastic wave equation becomes

$$\begin{aligned} (\epsilon^2 D_{t'}^2 - 2\epsilon c_0 D_{t'}\partial_{x'} + c_0^2\partial_{x'}^2)\rho &= \partial_{x'}^2(\rho v_1^2 - \sigma_{xx}) + 2\epsilon^{1/2}\partial_{x'}\partial_y'(\rho v_1 v_2 - \sigma_{xy}) \\ &+ 2\epsilon^{1/2}\partial_{x'}\partial_{z'}(\rho v_1 v_3 - \sigma_{xz}) + \epsilon\{\partial_{y'}^2(\rho v_2^2 - \sigma_{yy}) \\ &+ \partial_{z'}^2(\rho v_3^2 - \sigma_{zz}) + 2\partial_{y'}\partial_{z'}(\rho v_2 v_3 - \sigma_{yz})\}, \end{aligned} \tag{4.19}$$

and the stress-velocity relations become

$$
\begin{aligned}
(\epsilon D_{t'} - c_0\partial_{x'})\sigma_{xx} &= (\lambda + 2\mu)\partial_{x'}v_1 + \epsilon^{1/2}\lambda(\partial_{y'}v_2 + \partial_{z'}v_3) \\
(\epsilon D_{t'} - c_0\partial_{x'})\sigma_{yy} &= \lambda\partial_{x'}v_1 + \epsilon^{1/2}[(\lambda + 2\mu)\partial_{y'}v_2 + \lambda\partial_{z'}v_3] \\
(\epsilon D_{t'} - c_0\partial_{x'})\sigma_{zz} &= \lambda\partial_{x'}v_1 + \epsilon^{1/2}[\lambda\partial_{y'}v_2 + (\lambda + 2\mu)\partial_{z'}v_3] \\
(\epsilon D_{t'} - c_0\partial_{x'})\sigma_{xy} &= \mu\partial_{x'}v_2 + \epsilon^{1/2}\mu\partial_{y'}v_1 \\
(\epsilon D_{t'} - c_0\partial_{x'})\sigma_{xz} &= \mu\partial_{x'}v_3 + \epsilon^{1/2}\mu\partial_{y'}v_1 \\
(\epsilon D_{t'} - c_0\partial_{x'})\sigma_{yz} &= \epsilon^{1/2}\mu(\partial_{y'}v_3 + \partial_{z'}v_2).
\end{aligned}
\tag{4.20}
$$

The primes are dropped in subsequent equations to ease notation.

4.2.3 Asymptotic Analysis

Perturbations are applied to the eleven dependent variables ρ, p, v_i, and σ_{ij} to represent an acoustic disturbance. Choices for the scaling factor ϵ are meant to mirror the choices seen in the original derivation (McDonald *et al.*, 1994). Naive expansions are used for ρ and p:

$$
\begin{aligned}
\rho &\approx \rho_0 + \epsilon\rho_1 + \epsilon^2\rho_2 \\
p &\approx p_0 + \epsilon p_1 + \epsilon^2 p_2,
\end{aligned}
\tag{4.21}
$$

where a subscript of zero denotes a constant, ambient quantity. For the velocity terms, again naive expansions are employed but the v_{i0} term is omitted due to the assumption that the background velocity is absent, and the y and z velocities are considered small compared to the x velocity:

$$
\begin{aligned}
v_1 \equiv v_x &\approx \epsilon v_{x1} + \epsilon^2 v_{x2} \\
v_2 \equiv v_y &\approx \epsilon^2 v_{y2} \\
v_3 \equiv v_z &\approx \epsilon^2 v_{z2}.
\end{aligned}
\tag{4.22}
$$

Naive expansions are applied to values of normal stress to maintain consistency with the pressure expression:

$$
\begin{aligned}
\sigma_{xx} &\approx \sigma_{xx0} + \epsilon\sigma_{xx1} + \epsilon^2\sigma_{xx2} \\
\sigma_{yy} &\approx \sigma_{yy0} + \epsilon\sigma_{yy1} + \epsilon^2\sigma_{yy2} \\
\sigma_{zz} &\approx \sigma_{zz0} + \epsilon\sigma_{zz1} + \epsilon^2\sigma_{zz2},
\end{aligned}
\tag{4.23}
$$

where again the zero-subscripted terms indicate constant values. In this formulation, the shear stresses are considered small relative to the normal stresses and are given by

$$\begin{aligned} \sigma_{xy} &\approx \epsilon^{3/2}\sigma_{xy1} + \epsilon^2\sigma_{xy2} \\ \sigma_{xz} &\approx \epsilon^{3/2}\sigma_{xz1} + \epsilon^2\sigma_{xz2} \\ \sigma_{yz} &\approx \epsilon^{3/2}\sigma_{yz1} + \epsilon^2\sigma_{yz2}. \end{aligned} \tag{4.24}$$

The background, ambient shear stress terms are omitted due to the fact that, in absence of an acoustic disturbance, the stress in the medium is dictated only by the geostatic pressure (compressive stress from the self-weight of the medium) which is related solely to normal stress (Richards, 2000). Leading order terms in the shear stress expansions are $\epsilon^{3/2}$ to reduce the total effect of shear in the system yet still provide shear correction terms in the final governing equation. The assumption that shear-wave propagation is a weak, second order effect when compared to pressure-wave propagation is often accurate for most underwater environments where the sediment is largely unconsolidated.

Each of the subscripted values in (4.21) through (4.24), except the constant, ambient values, is in general a function of x, y, z, and t. Substituting the appropriate asymptotic expansions into the continuity equation (4.18), gives

$$\begin{aligned} &(\epsilon D_t - c_0\partial_x)(\rho_0 + \epsilon\rho_1 + \epsilon^2\rho_2) \\ &\quad = -\partial_x[(\rho_0 + \epsilon\rho_1 + \epsilon^2\rho_2)(\epsilon v_{x1} + \epsilon^2 v_{x2})] \\ &\quad -\epsilon^{1/2}\partial_y[(\rho_0 + \epsilon\rho_1 + \epsilon^2\rho_2)\epsilon^2 v_{y2}] \\ &\quad -\epsilon^{1/2}\partial_z[(\rho_0 + \epsilon\rho_1 + \epsilon^2\rho_2)\epsilon^2 v_{z2}]. \end{aligned} \tag{4.25}$$

Equating first order (ϵ) terms gives

$$\partial_x v_{x1} = \frac{c_0}{\rho_0}\partial_x\rho_1. \tag{4.26}$$

Equation (4.26) is integrated with respect to x to obtain

$$v_{x1} = c_0\frac{\rho_1}{\rho_0}. \tag{4.27}$$

Integration constants that may be functions of y and z are ignored by assuming that the expansions given in (4.21) and (4.22) are consistent with the narrow-angle approximation. Integration constants that are constant values are omitted as well since they disappear through differentiation at the end of the derivation. Now, substitute the appropriate asymptotic expansions into the stress-velocity relations, equation (4.20), to get

$$\begin{aligned}
(\epsilon D_t - c_0\partial_x)(\sigma_{xx0} + \epsilon\sigma_{xx1} + \epsilon^2\sigma_{xx2}) &= (\lambda+2\mu)\partial_x(\epsilon v_{x1} + \epsilon^2 v_{x2}) \\
&+ \epsilon^{1/2}\lambda[\partial_y(\epsilon^2 v_{y2}) + \partial_z(\epsilon^2 v_{z2})] \\
(\epsilon D_t - c_0\partial_x)(\sigma_{yy0} + \epsilon\sigma_{yy1} + \epsilon^2\sigma_{yy2}) &= \lambda\partial_x(\epsilon v_{x1} + \epsilon^2 v_{x2}) \\
&+ \epsilon^{1/2}[(\lambda+2\mu)\partial_y(\epsilon^2 v_{y2}) + \lambda\partial_z(\epsilon^2 v_{z2})] \\
(\epsilon D_t - c_0\partial_x)(\sigma_{zz0} + \epsilon\sigma_{zz1} + \epsilon^2\sigma_{zz2}) &= \lambda\partial_x(\epsilon v_{x1} + \epsilon^2 v_{x2}) \\
&+ \epsilon^{1/2}[\lambda\partial_y(\epsilon^2 v_{y2}) + (\lambda+2\mu)\partial_z(\epsilon^2 v_{z2})] \\
(\epsilon D_t - c_0\partial_x)(\epsilon^{3/2}\sigma_{xy1} + \epsilon^2\sigma_{xy2}) &= \mu\partial_x(\epsilon^2 v_{y2}) + \epsilon^{1/2}\mu\partial_y(\epsilon v_{x1} + \epsilon^2 v_{x2}) \\
(\epsilon D_t - c_0\partial_x)(\epsilon^{3/2}\sigma_{xz1} + \epsilon^2\sigma_{xz2}) &= \mu\partial_x(\epsilon^2 v_{z2}) + \epsilon^{1/2}\mu\partial_z(\epsilon v_{x1} + \epsilon^2 v_{x2}) \\
(\epsilon D_t - c_0\partial_x)(\epsilon^{3/2}\sigma_{yz1} + \epsilon^2\sigma_{yz2}) &= \epsilon^{1/2}\mu[\partial_y(\epsilon^2 v_{z2}) + \partial_z(\epsilon^2 v_{y2})].
\end{aligned} \tag{4.28}$$

Equating first order (ϵ) terms in the σ_{xx} equation yields

$$-c_0\partial_x\sigma_{xx1} = (\lambda+2\mu)\partial_x v_{x1}. \tag{4.29}$$

Integrating with respect to x and using (4.27) gives

$$\sigma_{xx1} = -(\lambda+2\mu)\frac{\rho_1}{\rho_0}. \tag{4.30}$$

Expressions for σ_{yy1} and σ_{zz1} are generated in a similar way to produce

$$\sigma_{yy1} = \sigma_{zz1} = -\lambda\frac{\rho_1}{\rho_0}. \tag{4.31}$$

Now, equating three halves order ($\epsilon^{3/2}$) terms in the σ_{xy} equation gives

$$-c_0\partial_x\sigma_{xy1} = \mu\partial_y v_{x1}. \tag{4.32}$$

Integrating with respect to x and employing (4.27) gives

$$\sigma_{xy1} = -\mu \int_{x_f}^{x} \partial_y \frac{\rho_1}{\rho_0} \, \mathrm{d}x, \tag{4.33}$$

where the limits of integration are assigned according to the problem being considered. The same approach is used to find the expression for σ_{xz1}:

$$\sigma_{xz1} = -\mu \int_{x_f}^{x} \partial_z \frac{\rho_1}{\rho_0} \, \mathrm{d}x. \tag{4.34}$$

Looking at the three halves ($\epsilon^{3/2}$) and second (ϵ^2) order terms in the final equation in (4.28) for σ_{yz} reveals that

$$\sigma_{yz1} = \sigma_{yz2} = 0, \tag{4.35}$$

indicating that the yz shear stress is negligible. Once again, the σ_{xx} expression is examined, but now equating second order (ϵ^2) terms in conjunction with (4.30) produces an equation for the x derivative of σ_{xx2}:

$$\partial_x \sigma_{xx2} = -\frac{\lambda + 2\mu}{c_0} \left(D_t \frac{\rho_1}{\rho_0} + \partial_x v_{x2} \right). \tag{4.36}$$

A similar procedure is followed to obtain terms for the x derivative of σ_{yy2} and σ_{zz2} given by

$$\partial_x \sigma_{yy2} = \partial_x \sigma_{zz2} = -\frac{\lambda}{c_0} \left(D_t \frac{\rho_1}{\rho_0} + \partial_x v_{x2} \right). \tag{4.37}$$

Applying asymptotic expansions to the pressure-stress relation, equation (4.13), and equating zero order (ϵ^0) terms leads to

$$p_0 = -\frac{\sigma_{xx0} + \sigma_{yy0} + \sigma_{zz0}}{3}, \tag{4.38}$$

which indicates that the background pressure in the medium is the average of the normal stresses present due to the weight of the surrounding material (a hydrostatic pressure), a

physically realistic presumption. Equating first order (ϵ) terms gives

$$p_1 = -\frac{\sigma_{xx1} + \sigma_{yy1} + \sigma_{zz1}}{3}, \tag{4.39}$$

to which (4.30) and (4.31) are applied to yield

$$p_1 = \left(\lambda + \frac{2}{3}\mu\right)\frac{\rho_1}{\rho_0} = K_0\frac{\rho_1}{\rho_0}, \tag{4.40}$$

where $K_0 = \lambda + 2/3\mu$ is known as the average bulk modulus of the medium. The bulk modulus measures a substance's resistance to uniform compression, and is defined by

$$K = \rho\frac{dP}{d\rho}. \tag{4.41}$$

Equation (4.40) represents the first order result in the expansion of (4.41). One now equates the second order (ϵ^2) terms in the pressure-stress relation to give

$$p_2 = -\frac{\sigma_{xx2} + \sigma_{yy2} + \sigma_{zz2}}{3}. \tag{4.42}$$

Differentiating (4.42) with respect to x and applying (4.36) and (4.37) gives

$$\partial_x p_2 = \frac{K_0}{c_0}\left(D_t\frac{\rho_1}{\rho_0} + \partial_x v_{x2}\right). \tag{4.43}$$

Rearranging leads to an expression for the x direction derivative of the second order x velocity term:

$$\partial_x v_{x2} = \frac{c_0}{K_0}\partial_x p_2 - D_t\frac{\rho_1}{\rho_0}. \tag{4.44}$$

The equation of state, (4.12), is treated by assuming the linear parameter, A, can be asymptotically expanded (with only a single, first order correction):

$$A \approx A_0 + \epsilon A_1(x, y, z), \tag{4.45}$$

where $A_1(x, y, z)$ is a spatial variation from A_0. Spatial variations in B are assumed to have a negligible effect as B already operates on a second order term. Applying appropriate asymptotic expansions to the remaining terms in (4.12) gives

$$\epsilon p_1 + \epsilon^2 p_2 = (A_0 + \epsilon A_1)\left(\frac{\epsilon\rho_1 + \epsilon^2\rho_2}{\rho_0}\right) + \frac{B}{2}\left(\frac{\epsilon\rho_1 + \epsilon^2\rho_2}{\rho_0}\right)^2. \tag{4.46}$$

Looking at the first order (ϵ) terms, shows that

$$p_1 = A_0\frac{\rho_1}{\rho_0}, \tag{4.47}$$

and, from equation (4.40), it must follow that $A_0 = K_0$. This statement reflects the fact that the definition of A seen in equation (4.9) is equivalent to the definition of bulk modulus seen in equation (4.41). Therefore, A_0 and A_1 are replaced with K_0 and K_1 to simplify further notation. Equating second order (ϵ^2) terms leads to the relationship between p_2 and ρ_2:

$$p_2 = K_0\frac{\rho_2}{\rho_0} + K_1\frac{\rho_1}{\rho_0} + \frac{B}{2}\left(\frac{\rho_1}{\rho_0}\right)^2 \tag{4.48}$$

At this point, appropriate asymptotic expansions are applied the coordinate-transformed nonlinear elastic wave equation, (4.19):

$$\begin{aligned}
&(\epsilon^2 D_t^2 - 2\epsilon c_0 D_t\partial_x + c_0^2\partial_x^2)(\rho_0 + \epsilon\rho_1 + \epsilon^2\rho_2) \\
&\quad = \partial_x^2[(\rho_0 + \epsilon\rho_1 + \epsilon^2\rho_2)(\epsilon v_{x1} + \epsilon^2 v_{x2})^2 - (\sigma_{xx0} + \epsilon\sigma_{xx1} + \epsilon^2\sigma_{xx2})] \\
&\quad +2\epsilon^{1/2}\partial_x\partial_y[(\rho_0 + \epsilon\rho_1 + \epsilon^2\rho_2)(\epsilon v_{x1} + \epsilon^2 v_{x2})(\epsilon^2 v_{y2}) - (\epsilon^{3/2}\sigma_{xy1} + \epsilon^2\sigma_{xy2})] \\
&\quad +2\epsilon^{1/2}\partial_x\partial_z[(\rho_0 + \epsilon\rho 1 + \epsilon^2\rho_2)(\epsilon v_{x1} + \epsilon^2 v_{x2})(\epsilon^2 v_{z2}) - (\epsilon^{3/2}\sigma_{xz1} + \epsilon^2\sigma_{xz2})] \\
&\quad +\epsilon\partial_y^2[(\rho_0 + \epsilon\rho_1 + \epsilon^2\rho_2)(\epsilon^2 v_{y2})^2 - (\sigma_{yy0} + \epsilon\sigma_{yy1} + \epsilon^2\sigma_{yy2})] \\
&\quad +\epsilon\partial_z^2[(\rho_0 + \epsilon\rho_1 + \epsilon^2\rho_2)(\epsilon^2 v_{z2})^2 - (\sigma_{zz0} + \epsilon\sigma_{zz1} + \epsilon^2\sigma_{zz2})] \\
&\quad +2\epsilon\partial_y\partial_z[(\rho_0 + \epsilon\rho_1 + \epsilon^2\rho_2)(\epsilon^2 v_{y2})(\epsilon^2 v_{z2})].
\end{aligned} \tag{4.49}$$

Zero order (ϵ^0) terms are trivially satisfied. Equating first order (ϵ) terms leads to

$$c_0^2\partial_x^2\rho_1 = -\partial_x^2\sigma_{xx1} \tag{4.50}$$

Applying the result for σ_{xx1} in equation (4.30) yields

$$c_0^2 \partial_x^2 \rho_1 = (\lambda + 2\mu)\partial_x^2 \frac{\rho_1}{\rho_0}. \tag{4.51}$$

If the velocity of the moving-frame, c_0, is taken to equal the average pressure-wave speed (sound speed) of the medium , i.e.

$$c_0 \equiv c_p = \sqrt{\frac{\lambda + 2\mu}{\rho_0}}, \tag{4.52}$$

then (4.51) is satisfied. Equating second order (ϵ^2) terms gives

$$\begin{aligned} &-2c_0 D_t \partial_x \rho_1 + c_0^2 \partial_x^2 \rho_2 \\ &\quad = \partial_x^2(\rho_0 v_{x1}^2 - \sigma_{xx2}) + 2\partial_x \partial_y(-\sigma_{xy1}) \\ &\quad +2\partial_x \partial_z(-\sigma_{xz1}) + \partial_y^2(-\sigma_{yy1}) - \partial_z^2(-\sigma_{zz1}). \end{aligned} \tag{4.53}$$

Rearranging (4.53), dividing by $-2c_0$, and differentiating with respect to x produces

$$\begin{aligned} D_t \rho_1 = \partial_x \left(\frac{c_0}{2}\rho_2 - \frac{\rho_0}{2c_0} v_{x1}^2 + \frac{1}{2c_0}\sigma_{xx2} \right) \\ +\frac{1}{c_0}\partial_y \sigma_{xy1} + \frac{1}{c_0}\partial_z \sigma_{xz1} + \frac{1}{2c_0}\int_{x_f}^{x} (\partial_y^2 \sigma_{yy1} + \partial_z^2 \sigma_{zz1})\, \mathrm{d}x. \end{aligned} \tag{4.54}$$

Applying equations (4.27), (4.33), (4.34), (4.36), and (4.37) yields

$$\begin{aligned} D_t \rho_1 = \partial_x \left[\frac{c_0}{2}\rho_2 - \frac{\rho_0 c_0}{2}\left(\frac{\rho_1}{\rho_0}\right)^2 \right] - \frac{\lambda + 2\mu}{2c_0^2}\left[D_t \frac{\rho_1}{\rho_0} + \partial_x v_{x2} \right] \\ -\frac{\mu}{c_0}\int_{x_f}^{x} \partial_y^2 \frac{\rho_1}{\rho_0}\mathrm{d}x - \frac{\mu}{c_0}\int_{x_f}^{x} \partial_z^2 \frac{\rho_1}{\rho_0}\mathrm{d}x - \frac{\lambda}{2c_0}\int_{x_f}^{x} \left[\partial_y^2 \frac{\rho_1}{\rho_0} + \partial_z^2 \frac{\rho_1}{\rho_0} \right] \mathrm{d}x. \end{aligned} \tag{4.55}$$

Equation (4.55) simplifies to

$$\begin{aligned} D_t \rho_1 = \partial_x \left[\frac{c_0}{2}\rho_2 - \frac{\rho_0 c_0}{2}\left(\frac{\rho_1}{\rho_0}\right)^2 - \frac{\lambda + 2\mu}{2c_0^2} v_{x2} \right] - \frac{\lambda + 2\mu}{2c_0^2} D_t \frac{\rho_1}{\rho_0} \\ -\frac{\lambda + 2\mu}{2c_0}\int_{x_f}^{x} (\partial_y^2 + \partial_z^2)\frac{\rho_1}{\rho_0}\, \mathrm{d}x. \end{aligned} \tag{4.56}$$

Using the definition of c_0, equation (4.52), allows (4.56) to reduce further to

$$D_t\rho_1 = \partial_x \left[\frac{c_0}{2}\rho_2 - \frac{\rho_0 c_0}{2}\left(\frac{\rho_1}{\rho_0}\right)^2 - \frac{\rho_0}{2}v_{x2} \right] - \frac{\rho_0}{2} D_t \frac{\rho_1}{\rho_0} - \frac{\rho_0 c_0}{2}\int_{x_f}^{x} (\partial_y^2 + \partial_z^2)\frac{\rho_1}{\rho_0}\,\mathrm{d}x. \tag{4.57}$$

Applying the expression for $\partial_x v_{x2}$, equation (4.44), gives

$$D_t\rho_1 = \partial_x \left[\frac{c_0}{2}\rho_2 - \frac{\rho_0 c_0}{2}\left(\frac{\rho_1}{\rho_0}\right)^2 - \frac{\rho_0 c_0}{2K_0}p_2 \right] - \frac{\rho_0 c_0}{2}\int_{x_f}^{x} (\partial_y^2 + \partial_z^2)\frac{\rho_1}{\rho_0}\,\mathrm{d}x. \tag{4.58}$$

The last step in the derivation is to apply the equation of state, equation (4.48), for the p_2 term. Doing so yields

$$D_t\rho_1 = \partial_x \left[-\frac{\rho_0 c_0}{2}\frac{K_1}{K_0}\frac{\rho_1}{\rho_0} - \frac{\rho_0 c_0}{2}\left(1 + \frac{B}{2K_0}\right)\left(\frac{\rho_1}{\rho_0}\right)^2 \right] - \frac{\rho_0 c_0}{2}\int_{x_f}^{x} (\partial_y^2 + \partial_z^2)\frac{\rho_1}{\rho_0}\,\mathrm{d}x. \tag{4.59}$$

Simplifying and dividing through by ρ_0 gives

$$D_t\frac{\rho_1}{\rho_0} = -\partial_x \left[\frac{c_0}{2}\frac{K_1}{K_0}\frac{\rho_1}{\rho_0} + \frac{c_0}{2}\left(1 + \frac{B}{2K_0}\right)\left(\frac{\rho_1}{\rho_0}\right)^2 \right] - \frac{c_0}{2}\int_{x_f}^{x} (\partial_y^2 + \partial_z^2)\frac{\rho_1}{\rho_0}\,\mathrm{d}x. \tag{4.60}$$

Now, (4.60) is written in terms of a single variable $R = \frac{\rho_1}{\rho_0}$, a dimensionless density perturbation, leaving the final form of the WENPE:

$$D_t R = -\partial_x \left[\frac{c_0}{2}\frac{K_1}{K_0}R + \frac{c_0}{2}\left(1 + \frac{B}{2K_0}\right)R^2 \right] - \frac{c_0}{2}\int_{x_f}^{x} (\partial_y^2 + \partial_z^2)R\,\mathrm{d}x. \tag{4.61}$$

This new equation has nearly the same form as the original NPE except for changes to the refraction and nonlinear steepening terms. Because the form of the equation remains the same, the same numerical implementation can be used which is described in Chapter 2.

4.3 Relationship to the original fluid NPE

The NPE can be seen as a particular case of the more general WENPE in which the medium is considered a fluid. As such, one expects that the original NPE may be reconstructed when simplifying assumptions are made for the environment. The formulation of the NPE, starting from the WENPE, is outlined here.

One first assumes that the medium is an inviscid fluid, and, as such, shear stress is not supported. Therefore, the shear modulus, μ, equals zero. It should be noted that shear stress and fluid viscosity are not the same: shear stress is proportional to the total amount of shear deformation, whereas in a fluid the viscosity is proportional to the rate of shear deformation over time. In the case of the NPE, it is assumed that the shear deformation is zero for all time so both the shear stress and viscosity are nonexistent.

According to acoustic theory, the small-signal sound speed of the medium is defined as

$$c^2 = \left[\frac{\partial p}{\partial \rho}\right]_{s_0}. \tag{4.62}$$

The derivative of c^2 with respect to density is

$$\frac{\partial c^2}{\partial \rho} = \frac{\partial^2 p}{\partial \rho^2}. \tag{4.63}$$

This leads to expansion coefficients given by

$$A = \rho_0 \left[\frac{\partial p}{\partial \rho}\right]_{s_0} = \rho_0 c^2 \tag{4.64}$$

and

$$B = \rho_0^2 \left[\frac{\partial^2 p}{\partial \rho^2}\right]_{s_0} = \rho_0^2 \frac{\partial c^2}{\partial \rho} = 2\rho_0^2 c \frac{\partial c}{\partial \rho}. \tag{4.65}$$

Now, it is assumed that the sound speed can vary slightly in space, $c = c_0 + \epsilon c_1(x, z)$, where c_0 is the average sound speed of the medium and c_1 is a small spatial deviation from the

average. As before, the linear expansion parameter, A, is asymptotically expanded to

$$A \approx A_0 + \epsilon A_1(x, z), \tag{4.66}$$

and by matching powers of epsilon the approximations for K_0 and K_1 are computed to be

$$K_0 = A_0 = \rho_0 c_0^2, \tag{4.67}$$
$$K_1 = A_1 = 2\rho_0 c_0 c_1. \tag{4.68}$$

Applying (4.65), (4.67), and (4.68) to the WENPE, equation (4.69), yields

$$D_t R = -\partial_x \left[c_1 R + \frac{\beta c_0}{2} R^2 \right] - \frac{c_0}{2} \int_{x_f}^{x} \partial_z^2 R \, \mathrm{d}x, \tag{4.69}$$

where

$$\beta = 1 + \frac{\rho_0}{c_0} \left(\frac{\partial c}{\partial \rho} \right)_{s_0} \tag{4.70}$$

is the coefficient of nonlinearity. Equation (4.70) is the exact form of the original NPE.

4.4 Mesh Convergence Study

A mesh convergence study is presented here to investigate how the resolution of the computational grid effects the solution. Numerically, the weakly-elastic NPE is identical to the fractional NPE with zero attenuation ($\alpha_0 = 0$), and a mesh convergence study has been performed for the fractional model in Section 3.3.1. However, it is still necessary to have a mesh convergence study for the attenuation-free case because all observed dissipation will be numerical in nature. This gives more insight into the accuracy of the numerical methods employed, especially the flux-corrected transport scheme that captures the nonlinear shock. It is expected that the convergence rate be similar to that of the fractional NPE because the numerical procedures are the same.

The problem used for the study is similar to the convergence study done with the fractional NPE model: the evolution of a 1D square shock wave in a weakly-elastic sediment

without attenuation. The sediment has a density of 1500 kg/m^3 and elastic parameters $\lambda =$ 3.8 GPa and $\mu = 0.15$ GPa. The initial waveform used in the study is a 10 m long square shock with an amplitude of 100 MPa as seen in Figure 4.1 below. The 1D computational domain is 50 m long and the grid spacing is set to 1.0, 0.5, 0.25, and 0.125 m to allow for 50, 100, 200, and 400 points in the mesh, respectively. The time step is set to 0.01 ms and the coefficient of nonlinearity β is set to 3.5. The shock is propagated for a total of 100 ms. The results are given in Figure 4.2 and show that the solution does not have a strong dependence on the mesh. The rate of convergence computed using the L^1 norm of the pressure profiles is found to be 1.00.

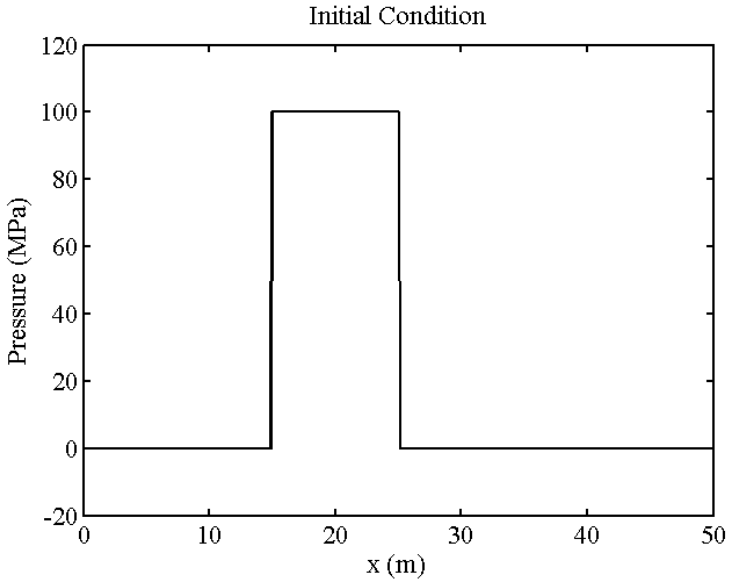

Figure 4.1: Initial condition for mesh convergence study.

4.5 Weak Elasticity Study

The weakly-elastic NPE has been shown to reduce to the original NPE when the shear modulus μ is zero. However, the upper limit for μ is unknown: the rigidity for which the weak elasticity assumption fails. A study is presented here to attempt to determine the range of elastic properties for which the WENPE is valid within a typical ocean waveguide. This

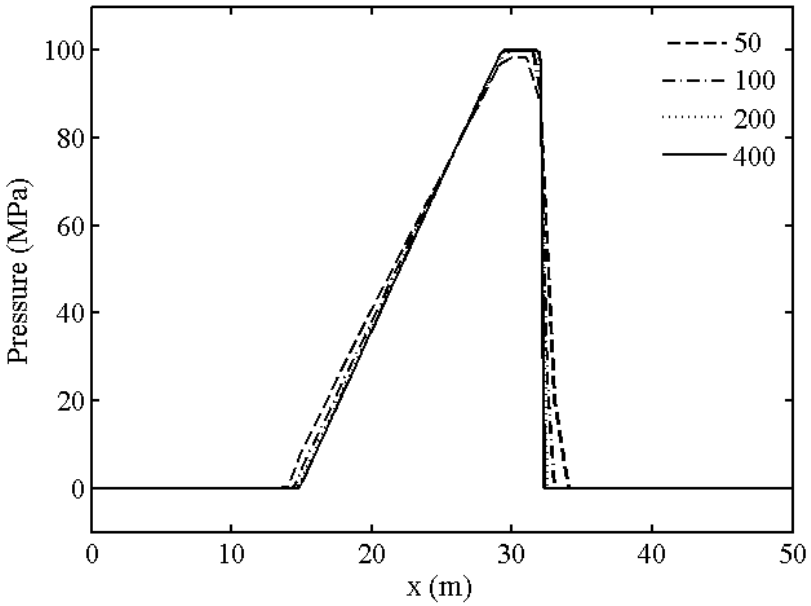

Figure 4.2: Waveform at t = 100 ms for the mesh convergence study.

is done by comparing results of the WENPE to those of the progressive elastic-fluid model (developed in Section 5.5 of the next chapter) for a range of varying sediment shear speeds. It is expected that there exists a range of shear speeds for which both solutions match, and at some point the solutions will start to diverge as the shear speed becomes significant.

The environment for the study is a flat, layered waveguide with a water column depth of 60 m atop an additional 15 m of sediment depth. The water column has a density of 1000 kg/m^3 and a sound speed of 1500 m/s, whereas the sediment has a density of 1378 kg/m^3 and a compressional wave speed of 1650 m/s. The shear wave speed in the sediment layer is varied from 200 m/s to 1200 m/s over a total of six test cases. The elastic parameters for the six test cases are summarized in Table 4.1 below. The lowest shear speed analyzed is 200 m/s, because below this value, solutions from the progressive elastic-fluid model become inaccurate. This is due to singularities brought about by the small shear modulus value. The highest shear speed analyzed is 1200 m/s which leads to a negative Poisson ratio (auxetic material); this material may not be physically realistic for seafloors, but is presented for illustrative purposes.

Table 4.1: Elastic parameters of the sediment layer for the weak elasticity study.

Test Case	Shear Speed (m/s)	λ (GPa)	μ (GPa)	ν
1	200	3.641	0.055	0.493
2	400	3.311	0.220	0.469
3	600	2.759	0.496	0.424
4	800	1.988	0.882	0.346
5	1000	0.996	1.378	0.210
6	1200	-0.217	1.984	-0.061

The source used in the study is a simulated explosive blast located at $z_s = 30$ m. The blast wave is modeled with a Friedlander waveform which comprises of a sharp shock with peak pressure of 10 MPa that exponentially decays to zero, as seen in Figure 4.3. The pressure profile is representative of a detonation of approximately 100 kg of TNT. This problem is considered in a moving rectangular computational domain of depth 75 m and width 30 m. The x direction grid spacing is 0.5 m, the z direction grid spacing is 0.5 m, and the time step is 0.1 ms. The nonlinear case is considered and as such the coefficient of nonlinearity β is set to 3.5, a value typical of ocean environments (McDonald & Kuperman, 1987). An artificial absorbing layer starting at $z = 67$ m is used to damp out any energy near the bottom of the computational grid to prevent any unrealistic reflections. The simulation marches the domain out to a final range of 400 m, and pressure data is saved at four different receiver locations: 100 m and 400 m in range (both at 20 m and 50 m in depth). The receiver locations are chosen as such to capture the primary and secondary reflections which are the areas of the wave that are expected to change the most from case to case.

The time series data at the receiver locations are then compared to those of the progressive elastic-fluid model. Results at the first upper receiver location ($x = 100$ m, $z = 20$ m) for Case 1 are shown in Figure 4.4 below. The plot shows that both solutions are in good agreement and accurately capture the first reflection from the ocean surface. The "wiggles" present in the WENPE solution are an artifact from the wave propagating in the z direction, since the model assumes propagation is dominant in the range direction (small-angle assumption).

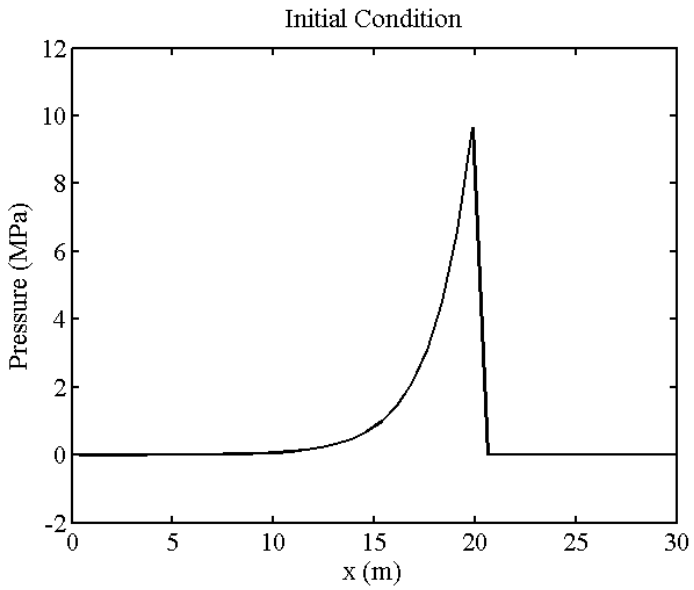

Figure 4.3: Initial condition for the weak elasticity study.

Results at the first lower receiver location (x = 100m, z = 50 m) for Case 1 is shown in Figure 4.5. The plot shows that there is a significant difference between the two solutions. This indicates that the first reflection at the ocean bottom is not being captured correctly by the WENPE model.

In order to determine the exact cause of the difference between the two solutions, the entire pressure field is compared for both models in the area near the first receiver positions. The pressure fields are given in Figure 4.6 for a time of approximately 70 ms into the simulation. The plots illustrate some major distinctions between the two models. In the WENPE model, the wave in the sediment layer has already propagated ahead of the main wavefront and generates a slight head wave in the fluid layer. Also, there is a weak negative phase tailing the first reflection off the bottom interface. In the progressive elastic-fluid model, the compressional wave in the sediment has not progressed as far because it takes a small amount of time for the compressional wave to decouple from the shear wave. The trailing shear wave then interacts with the interface generating a secondary compressional wave in the sediment. The elastic model also shows there is no negative phase behind the first bottom reflection as this is translated entirely into shear wave energy at the interface.

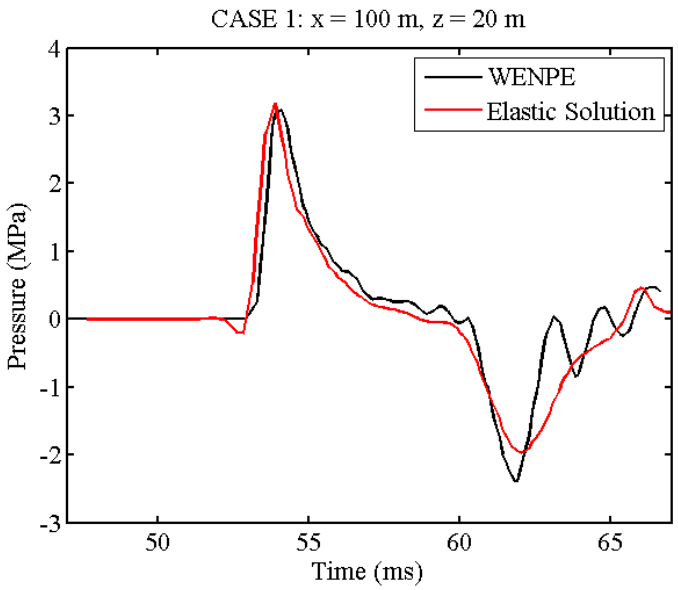

Figure 4.4: Pressure profiles at the upper receiver position for Case 1. Reflection at the ocean surface is accurately captured by both models.

These subtle differences lead to large errors in the wave field at far distances.

The individual plots for all test cases as well as pressure field plots are given in Appendix B. The results show that similar differences exist for all test cases. This is to be expected as the shear strength is greater for the remaining cases. The case that appears to match the best is Case 4. This is because the bulk modulus for the sediment is nearly equal to that of water, so the ratio of moduli K_1/K_0 seen in the WENPE equation is nearly one, thus leading to a correct interface approximation. This analysis has shown that the WENPE model is unable to resolve the wave field for moderately rigid ocean bottoms because of errors at the ocean-bottom interface. There still must exist a shear modulus μ small enough for which the WENPE is accurate. However, it appears that it is smaller than what can be handled by the progressive elastic-fluid model. This means there is no overlapping solution space for the WENPE and progressive elastic-fluid models, so extreme care must be taken with sediments with very low shear speeds.

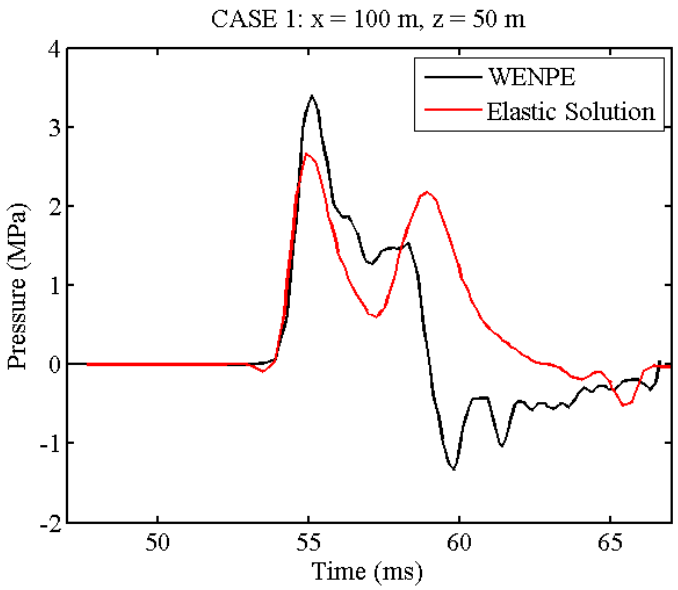

Figure 4.5: Pressure profiles at the lower receiver position for Case 1. Reflection at the ocean bottom is not accurately captured by the WENPE, even for the weak elasticity case.

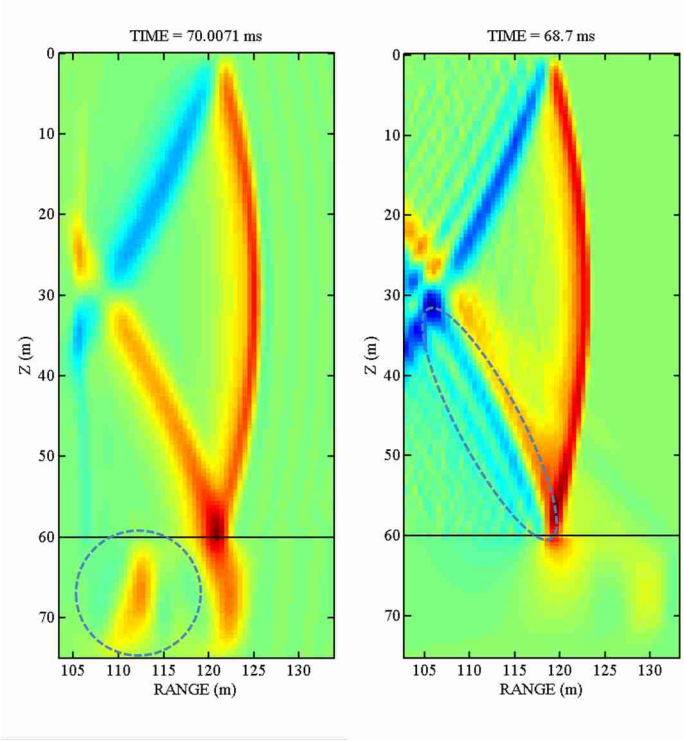

Figure 4.6: Pressure fields after the first reflection. Left plot represents progressive elastic-fluid solution and right plot represents WENPE solution. Important physical differences are circled.

4.6 Discussion

The derivation of the original NPE was modified to allow for weak elasticity, which is defined as a material where the shear stress is a higher order effect compared to the normal stress. The weakly-elastic NPE was implemented in a similar way as the original NPE, using an operator splitting approach, and the numerical solution was found to not be highly dependent on the mesh resolution. Comparisons with the progressive elastic-fluid model provided insight into the shortcomings of the model when applied to layered ocean waveguides. Results showed that discrepancies develop at the ocean-bottom interface for even relatively weak elastic bottoms. These discrepancies compound over the full range of interest, ultimately leading to an erroneous pressure profile. A discussion is provided here to investigate this behavior seen in the study.

The WENPE model is an equation of a single unknown and therefore is incapable of describing a true elastic medium which requires solving for two unknowns at a minimum (compressional and shear fields). From the derivation, it is observed that a first order approximation for the shear stress can be written as

$$\sigma_{xz} \approx -\mu \int_{x_f}^{x} \partial_z R \mathrm{d}x. \tag{4.71}$$

This approximation defines the shear stress in the direct vicinity of the pressure disturbance, but it does not describe the propagation of a shear wave on its own accord. Thus the WENPE model is essentially a fluid approximation solution with elastic parameters correctly transcribed into fluid parameters. Despite this, the derivation still accounted for weak elasticity and therefore shows that the fluid approximation holds merit in a mathematical sense. That is, the fluid approximation is valid when shear stress is of order $\epsilon^{3/2}$ or greater when compared to the normal stress. Equation (4.71) shows that the shear stress roughly

depends on the transverse derivative of the pressure field, so when the propagation is mainly in the x direction one expects the shear stress to be small for an appropriately small shear modulus. However, when the wave penetrates the seafloor, the transverse change in pressure is significant and the smallness approximation may be violated. This model may be more appropriate when there is a smooth transition in medium properties from the water to the sediment.

These errors at the interface were seen in the weak elasticity study for a layered ocean waveguide for the nonlinear case. Similar behavior is expected for the linear case as the linear case is a special case of the more general nonlinear case. This means this same investigation can be applied to problems that utilize the parabolic equation (PE) solution – the linear counterpart to the NPE. Thus, the analysis presented in this chapter applies to ocean acoustics in general, rather than just the long-range shock propagation problem.

This chapter has defined the limitations of applying NPE-based models to propagation problems involving elastic media. The inherent difficulty lies at the ocean-bottom interface and in the fact that the NPE is a single equation of a single unknown and elastic wave propagation comprises of coupled compressional and shear fields which have additional unknowns. Developing a coupled set of equations in a framework similar to the NPE is also not possible due to the nonlinearity. Therefore, the NPE approach will need to be abandoned when attempting to resolve the long-range shock propagation problem in fully elastic media.

CHAPTER 5

FULLY ELASTIC ENVIRONMENTS

Ocean waveguides typically comprise of a water column atop a basement layer. The basement layer can consist of loose unconsolidated sediments such as sand, gravel, and clays, but it can also contain hard rock layers such as basalt and granite found in the bedrock. These hard rock layers are capable of supporting strong shear waves and cannot be approximated as a fluid. Therefore, the weakly-elastic NPE model seen in the previous chapter which is accurate for low-shear media is no longer valid for environments that include fully-elastic layers. New, more robust models are required to describe both the dilatation and shear waves while still accounting for shock development. In this chapter, the governing equations are cast into hyperbolic conservation law forms to which powerful finite-volume techniques can be applied. The resulting elastic models are able to accurately describe shock propagation in environments of interest.

5.1 Introduction

Shock propagation through elastic solids is dictated by coupled, nonlinear equations. Standard finite difference techniques tend to be numerically unstable when applied to nonlinear equations. Certain methods such as the flux-corrected transport algorithm have been developed to capture weak shocks effectively but still introduce ringing (Gibbs' oscillations) and numerical dissipation when subjected to strong shocks (Tóth & Odstrčil, 1996). Families of techniques known as finite-volume methods are able to handle discontinuous solutions accurately by solving for fluxes rather than variable values (LeVeque, 2002).

Finite volume methods, like finite-difference methods, discretize a physical domain into a computational grid. The computational grid is comprised of finite volumes, referred to as cells, of specified size and shape. The flux of a state variable (such as density, stress, etc.) into or out of a cell's side is the same between cells so the variable is conserved throughout the

process. This is an excellent benefit when dealing with conservation laws of first-principles physics, but calculating the flux in between cells is difficult especially when there are large jumps in the values of the state variables between adjacent cells. The difficulty also increases when conserved variables obey nonlinear conservation laws as numerical stability and convergence become more complicated than with the linear case. Nonlinearities such as shocks must be dealt with carefully to ensure the method converges to the correct solution.

One approach for calculating flux in a nonlinear framework is the Godunov method (Godunov, 1959). In this method, a Riemann problem is solved at the jump between neighboring cells in order to determine characteristic speeds of the discontinuity based on the governing system of equations (or approximate system of equations). A Riemann problem is an initial value problems where a discontinuity separates two different states (Toro, 2009). Describing the jump in terms of a solution to the Riemann problem allows this method to accurately describe discontinuous solutions such as shocks as well as solutions in discontinuous media such as layered rock in the ocean bottom.

In this chapter, the nonlinear governing equations are cast in a quasi-conservation form and evaluated numerically using procedures based on high-order Godunov schemes. The first model developed is an elastic stationary model. This model describes nonlinear propagation of elastic waves within a stationary computational domain. This model is to be used as a basis on which to develop a progressive elastic model and ultimately a progressive, coupled fluid-solid model.

5.2 Governing Equations

Wave propagation through solids is dictated by a set of governing equations derived from first principles physics. As seen in the previous chapter, the equations are conservation of mass, conservation of momentum, constitutive relations between stress and strain, and an equation of state relating stress to the density of the medium. As before, conservation of energy is not considered here since it is assumed shock pressures are low enough to neglect

thermal effects. For the methods exhibited in this chapter, the governing equations must be presented in a conservation form wherein the overall change (in time) of the conserved variable is equal to zero. The equations of conservation of mass and conservation of momentum in the x and z directions, in conservation form, are given by

$$\frac{\partial \rho}{\partial t} + \frac{\partial}{\partial x}(\rho v_x) + \frac{\partial}{\partial z}(\rho v_z) = 0, \tag{5.1}$$

$$\frac{\partial}{\partial t}(\rho v_x) + \frac{\partial}{\partial x}(\rho v_x^2 - \sigma_{xx}) + \frac{\partial}{\partial z}(\rho v_x v_z - \sigma_{xz}) = \rho f_x, \tag{5.2}$$

$$\frac{\partial}{\partial t}(\rho v_z) + \frac{\partial}{\partial x}(\rho v_x v_z - \sigma_{xz}) + \frac{\partial}{\partial z}(\rho v_z^2 - \sigma_{zz}) = \rho f_z, \tag{5.3}$$

where f_x and f_z represent source terms. The constitutive laws relating stress to strain are similar to that given in the last chapter except here the time derivative is replaced by a material derivative in order to retain any nonlinear convective acceleration effects of stress. The constitutive relations are given by

$$\frac{D}{Dt}(\sigma_{xx}) \equiv \left(\frac{\partial}{\partial t} + v_x\frac{\partial}{\partial x} + v_z\frac{\partial}{\partial z}\right)\sigma_{xx} = (\lambda + 2\mu)\frac{\partial}{\partial x}v_x + \lambda\frac{\partial}{\partial z}v_z, \tag{5.4}$$

$$\frac{D}{Dt}(\sigma_{zz}) \equiv \left(\frac{\partial}{\partial t} + v_x\frac{\partial}{\partial x} + v_z\frac{\partial}{\partial z}\right)\sigma_{zz} = \lambda\frac{\partial}{\partial x}v_x + (\lambda + 2\mu)\frac{\partial}{\partial z}v_z, \tag{5.5}$$

$$\frac{D}{Dt}(\sigma_{xz}) \equiv \left(\frac{\partial}{\partial t} + v_x\frac{\partial}{\partial x} + v_z\frac{\partial}{\partial z}\right)\sigma_{xz} = \mu\frac{\partial}{\partial x}v_z + \mu\frac{\partial}{\partial z}v_x., \tag{5.6}$$

These equations are not conducive to the flux-differencing schemes used in numerical implementation, so they are rearranged to form

$$\frac{\partial}{\partial t}(\sigma_{xx}) + \frac{\partial}{\partial x}\left\{v_x\sigma_{xx} - (\lambda + 2\mu)v_x\right\} + \frac{\partial}{\partial z}\left(v_z\sigma_{xx} - \lambda v_z\right) = \sigma_{xx}\left(\frac{\partial v_x}{\partial x} + \frac{\partial v_z}{\partial z}\right) \tag{5.7}$$

$$\frac{\partial}{\partial t}(\sigma_{zz}) + \frac{\partial}{\partial x}\left(v_x\sigma_{zz} - \lambda v_x\right) + \frac{\partial}{\partial z}\left\{v_z\sigma_{zz} - (\lambda + 2\mu)v_z\right\} = \sigma_{zz}\left(\frac{\partial v_x}{\partial x} + \frac{\partial v_z}{\partial z}\right) \tag{5.8}$$

$$\frac{\partial}{\partial t}(\sigma_{xz}) + \frac{\partial}{\partial x}\left(v_x\sigma_{xz} - \mu v_z\right) + \frac{\partial}{\partial z}\left(v_z\sigma_{xz} - \mu v_x\right) = \sigma_{xz}\left(\frac{\partial v_x}{\partial x} + \frac{\partial v_z}{\partial z}\right). \tag{5.9}$$

Equations (5.7) - (5.9) represent a quasi-conservation form of (5.4) - (5.6) as the right-hand sides of the equations contain the conserved variables and are therefore not true source functions.

The final governing equation required to describe elastic wave propagation is an equation of state relating pressure, or some measure of dilatation, to density. The equation of state is material specific and can vary as a function of temperature or internal energy. However, in this work, thermal effects are not considered so internal energy is assumed to remain constant. Specific equations of state are discussed in a later section.

5.3 Elastic Stationary Model

In order to develop an effective long-range shock propagation model for elastic media, a short-range shock model is first developed that employs a stationary computational grid. Once the accuracy of the stationary model is established the analytic framework and numerical implementation can be extended to progressive models and coupled fluid-solid models.

The governing equations for nonlinear elastodynamics for two dimensions, in quasi-conservation form, are given by

$$\frac{\partial}{\partial t}\begin{pmatrix} \rho \\ \rho v_x \\ \rho v_z \\ \sigma_{xx} \\ \sigma_{zz} \\ \sigma_{xz} \end{pmatrix} + \frac{\partial}{\partial x}\begin{pmatrix} \rho v_x \\ \rho v_x^2 - \sigma_{xx} \\ \rho v_x v_z - \sigma_{xz} \\ v_x\sigma_{xx} - (\lambda+2\mu)v_x \\ v_x\sigma_{zz} - \lambda v_x \\ v_x\sigma_{xz} - \mu v_z \end{pmatrix} + \frac{\partial}{\partial z}\begin{pmatrix} \rho v_z \\ \rho v_x v_z - \sigma_{xz} \\ \rho v_z^2 - \sigma_{zz} \\ v_z\sigma_{xx} - \lambda v_z \\ v_z\sigma_{zz} - (\lambda+2\mu)v_z \\ v_z\sigma_{xz} - \mu v_x \end{pmatrix} = \begin{pmatrix} 0 \\ \rho f_x \\ \rho f_z \\ \sigma_{xx}\left(\frac{\partial v_x}{\partial x} + \frac{\partial v_z}{\partial z}\right) \\ \sigma_{zz}\left(\frac{\partial v_x}{\partial x} + \frac{\partial v_z}{\partial z}\right) \\ \sigma_{xz}\left(\frac{\partial v_x}{\partial x} + \frac{\partial v_z}{\partial z}\right) \end{pmatrix}. \tag{5.10}$$

The system of equations, (5.10), can be abbreviated as

$$\frac{\partial \mathbf{U}}{\partial t} + \frac{\partial F(\mathbf{U})}{\partial x} + \frac{\partial G(\mathbf{U})}{\partial z} = S(\mathbf{U}), \tag{5.11}$$

where $\mathbf{U}$ is a vector of quasi-conserved variables, $F(\mathbf{U})$ and $G(\mathbf{U})$ are fluxes, and $S(\mathbf{U})$ is a vector of source values. To solve these equations, a predictor-corrector strategy is adopted based on an approach presented by Miller and Colella (Miller & Colella, 2001). For each time step, a set of time-centered primitive variable values are calculated at each cell edge using a linearized set of governing equations. These edge values are used to pose Riemann problems at each edge, and solutions to the problems are used to construct the predictor fluxes. A corrector problem is then posited wherein previously defined edge values are adjusted using transverse predictor fluxes. After another set of Riemann problems are solved at each edge, the resulting fluxes are differentiated and combined with source values to generate the solution.

The numerical scheme is based on a standard high-order Godunov strategy that uses a characteristic analysis of the linearized equations. The quasilinear form of (5.10) is

$$\frac{\partial}{\partial t}\begin{pmatrix}\rho\\ v_x\\ v_z\\ \sigma_{xx}\\ \sigma_{zz}\\ \sigma_{xz}\end{pmatrix} + A_x\frac{\partial}{\partial x}\begin{pmatrix}\rho\\ v_x\\ v_z\\ \sigma_{xx}\\ \sigma_{zz}\\ \sigma_{xz}\end{pmatrix} + A_z\frac{\partial}{\partial z}\begin{pmatrix}\rho\\ v_x\\ v_z\\ \sigma_{xx}\\ \sigma_{zz}\\ \sigma_{xz}\end{pmatrix} = \begin{pmatrix}0\\ f_x\\ f_z\\ 0\\ 0\\ 0\end{pmatrix} \tag{5.12}$$

which can be stated as

$$\frac{\partial \mathbf{q}}{\partial t} + A_x\frac{\partial \mathbf{q}}{\partial x} + A_z\frac{\partial \mathbf{q}}{\partial z} = \mathbf{s}, \tag{5.13}$$

where $\mathbf{q} = [\rho\ v_x\ v_z\ \sigma_{xx}\ \sigma_{zz}\ \sigma_{xz}]^{\mathrm{T}}$ is a vector of primitive variables and $\mathbf{s} = [0\ f_x\ f_z\ 0\ 0\ 0]^{\mathrm{T}}$ is

the source term vector. The matrices A_x and A_z are given by

$$A_x = \begin{bmatrix} v_x & \rho & 0 & 0 & 0 & 0 \\ 0 & v_x & 0 & -1/\rho & 0 & 0 \\ 0 & 0 & v_x & 0 & 0 & -1/\rho \\ 0 & -(\lambda+2\mu) & 0 & v_x & 0 & 0 \\ 0 & -\lambda & 0 & 0 & v_x & 0 \\ 0 & 0 & -\mu & 0 & 0 & v_x \end{bmatrix} \tag{5.14}$$

and

$$A_z = \begin{bmatrix} v_z & 0 & \rho & 0 & 0 & 0 \\ 0 & v_z & 0 & 0 & 0 & -1/\rho \\ 0 & 0 & v_z & 0 & -1/\rho & 0 \\ 0 & 0 & -\lambda & v_z & 0 & 0 \\ 0 & 0 & -(\lambda+2\mu) & 0 & v_z & 0 \\ 0 & -\mu & 0 & 0 & 0 & v_z \end{bmatrix}. \tag{5.15}$$

The linearized matrix A_x has the eigenvalue decomposition

$$A_x = X_x \Lambda_x X_x^{-1}, \tag{5.16}$$

where X_x is the matrix of eigenvectors given by

$$X_x = \begin{bmatrix} 1 & 0 & -M_{xp}\rho & 0 & -M_{xp}\rho & 0 \\ 0 & 0 & M_{xp}c_p & 0 & -M_{xp}c_p & 0 \\ 0 & 0 & 0 & M_{xs}c_s & 0 & -M_{xs}c_s \\ 0 & 0 & M_{xp}(\lambda+2\mu) & 0 & M_{xp}(\lambda+2\mu) & 0 \\ 0 & 1 & M_{xp}\lambda & 0 & M_{xp}\lambda & 0 \\ 0 & 0 & 0 & M_{xs}\mu & 0 & M_{xs}\mu \end{bmatrix}, \tag{5.17}$$

where $c_p = \sqrt{\frac{\lambda+2\mu}{\rho}}$ and $c_s = \sqrt{\frac{\mu}{\rho}}$ represent the p-wave and s-wave velocities, respectively, and M_{xp} and M_{xs} are arbitrary constants. The columns of X_x are eigenvectors corresponding to eigenvalues in the diagonal matrix Λ_x given by

$$\Lambda_x = \begin{bmatrix} v_x & 0 & 0 & 0 & 0 & 0 \\ 0 & v_x & 0 & 0 & 0 & 0 \\ 0 & 0 & v_x - c_p & 0 & 0 & 0 \\ 0 & 0 & 0 & v_x - c_s & 0 & 0 \\ 0 & 0 & 0 & 0 & v_x + c_p & 0 \\ 0 & 0 & 0 & 0 & 0 & v_x + c_s \end{bmatrix}. \tag{5.18}$$

These eigenvalues represent the characteristic speeds of the system with two $(-)$ waves with velocities $v_x - c_\gamma$, two $(+)$ waves with velocities $v_x + c_\gamma$, and two material waves with velocities v_x, where γ is p or s. The inverse of X_x, X_x^{-1}, is given by

$$X_x^{-1} = \begin{bmatrix} 1 & 0 & 0 & \rho/(\lambda+2\mu) & 0 & 0 \\ 0 & 0 & 0 & -\lambda/(\lambda+2\mu) & 1 & 0 \\ 0 & 1/(2M_{xp}c_p) & 0 & 1/(2M_{xp}(\lambda+2\mu)) & 0 & 0 \\ 0 & 0 & 1/(2M_{xs}c_s) & 0 & 0 & 1/(2M_{xs}\mu) \\ 0 & -1/(2M_{xp}c_p) & 0 & 1/(2M_{xp}(\lambda+2\mu)) & 0 & 0 \\ 0 & 0 & -1/(2M_{xs}c_s) & 0 & 0 & 1/(2M_{xs}\mu) \end{bmatrix}. \tag{5.19}$$

The linearized A_z matrix has a similar eigenvalue decomposition with

$$A_z = X_z \Lambda_z X_z^{-1}, \tag{5.20}$$

where

$$X_z = \begin{bmatrix} 1 & 0 & -M_{zp}\rho & 0 & -M_{zp}\rho & 0 \\ 0 & 0 & 0 & M_{zs}c_s & 0 & -M_{zs}c_s \\ 0 & 0 & M_{zp}c_p & 0 & -M_{zp}c_p & 0 \\ 0 & 1 & M_{zp}\lambda & 0 & M_{zp}\lambda & 0 \\ 0 & 0 & M_{zp}(\lambda+2\mu) & 0 & M_{zp}(\lambda+2\mu) & 0 \\ 0 & 0 & 0 & M_{zs}\mu & 0 & M_{zs}\mu \end{bmatrix}, \tag{5.21}$$

$$\Lambda_z = \begin{bmatrix} v_z & 0 & 0 & 0 & 0 & 0 \\ 0 & v_z & 0 & 0 & 0 & 0 \\ 0 & 0 & v_z - c_p & 0 & 0 & 0 \\ 0 & 0 & 0 & v_z - c_s & 0 & 0 \\ 0 & 0 & 0 & 0 & v_z + c_p & 0 \\ 0 & 0 & 0 & 0 & 0 & v_z + c_s \end{bmatrix}, \tag{5.22}$$

and

$$X_z^{-1} = \begin{bmatrix} 1 & 0 & 0 & 0 & \rho/(\lambda+2\mu) & 0 \\ 0 & 0 & 0 & 1 & -\lambda/(\lambda+2\mu) & 0 \\ 0 & 0 & 1/(2M_{zp}c_p) & 0 & 1/(2M_{zp}(\lambda+2\mu)) & 0 \\ 0 & 1/(2M_{zs}c_s) & 0 & 0 & 0 & 1/(2M_{zs}\mu) \\ 0 & 0 & -1/(2M_{zp}c_p) & 0 & 1/(2M_{zp}(\lambda+2\mu)) & 0 \\ 0 & -1/(2M_{zs}c_s) & 0 & 0 & 0 & 1/(2M_{zs}\mu) \end{bmatrix}. \tag{5.23}$$

Again, M_{zp} and M_{zs} are arbitrary constants.

The numerical procedure also requires a method for relating the nonlinear equation, (5.10), to the linearized equation, (5.12). The time derivative of $\mathbf{U}$ is related to the time

derivative of $\mathbf{q}$ by

$$\frac{\partial \mathbf{U}}{\partial t} = \frac{\partial}{\partial t}\begin{pmatrix} q_1 \\ q_1 q_2 \\ q_1 q_3 \\ q_4 \\ q_5 \\ q_6 \end{pmatrix} = \begin{pmatrix} \frac{\partial}{\partial t} q_1 \\ q_1 \frac{\partial}{\partial t} q_2 + q_2 \frac{\partial}{\partial t} q_1 \\ q_1 \frac{\partial}{\partial t} q_3 + q_3 \frac{\partial}{\partial t} q_1 \\ \frac{\partial}{\partial t} q_4 \\ \frac{\partial}{\partial t} q_5 \\ \frac{\partial}{\partial t} q_6 \end{pmatrix} = \begin{bmatrix} 1 & 0 & 0 & 0 & 0 & 0 \\ q_2 & q_1 & 0 & 0 & 0 & 0 \\ q_3 & 0 & q_1 & 0 & 0 & 0 \\ 0 & 0 & 0 & 1 & 0 & 0 \\ 0 & 0 & 0 & 0 & 1 & 0 \\ 0 & 0 & 0 & 0 & 0 & 1 \end{bmatrix} \frac{\partial}{\partial t}\begin{pmatrix} q_1 \\ q_2 \\ q_3 \\ q_4 \\ q_5 \\ q_6 \end{pmatrix}. \tag{5.24}$$

More concisely,

$$\frac{\partial \mathbf{U}}{\partial t} = H(\mathbf{q}) \frac{\partial \mathbf{q}}{\partial t}, \tag{5.25}$$

where

$$H = \begin{bmatrix} 1 & 0 & 0 & 0 & 0 & 0 \\ v_x & \rho & 0 & 0 & 0 & 0 \\ v_z & 0 & \rho & 0 & 0 & 0 \\ 0 & 0 & 0 & 1 & 0 & 0 \\ 0 & 0 & 0 & 0 & 1 & 0 \\ 0 & 0 & 0 & 0 & 0 & 1 \end{bmatrix}. \tag{5.26}$$

Using (5.25), Eq. (5.11) can be written as

$$H(\mathbf{q}) \frac{\partial \mathbf{q}}{\partial t} + \frac{\partial F(\mathbf{U})}{\partial x} + \frac{\partial G(\mathbf{U})}{\partial z} = S(\mathbf{U}). \tag{5.27}$$

The inverse of H, H^{-1}, is computed as

$$H^{-1} = \begin{bmatrix} 1 & 0 & 0 & 0 & 0 & 0 \\ -v_x/\rho & 1/\rho & 0 & 0 & 0 & 0 \\ -v_z/\rho & 0 & 1/\rho & 0 & 0 & 0 \\ 0 & 0 & 0 & 1 & 0 & 0 \\ 0 & 0 & 0 & 0 & 1 & 0 \\ 0 & 0 & 0 & 0 & 0 & 1 \end{bmatrix} = \begin{bmatrix} 1 & 0 & 0 & 0 & 0 & 0 \\ 0 & 1 & 0 & 0 & 0 & 0 \\ 0 & 0 & 1 & 0 & 0 & 0 \\ 0 & 0 & 0 & 1 & 0 & 0 \\ 0 & 0 & 0 & 0 & 1 & 0 \\ 0 & 0 & 0 & 0 & 0 & 1 \end{bmatrix} - \begin{bmatrix} 0 & 0 & 0 & 0 & 0 & 0 \\ v_x/\rho & 1-1/\rho & 0 & 0 & 0 & 0 \\ v_z/\rho & 0 & 1-1/\rho & 0 & 0 & 0 \\ 0 & 0 & 0 & 0 & 0 & 0 \\ 0 & 0 & 0 & 0 & 0 & 0 \\ 0 & 0 & 0 & 0 & 0 & 0 \end{bmatrix}, \tag{5.28}$$

which is abbreviated as $H^{-1} = I - C$. The vectors $F^c = C \cdot F$ and $G^c = C \cdot G$ are referred to as the nonlinear adjustment fluxes and are written as

$$F^c = \begin{pmatrix} 0 \\ \rho v_x^2 - \sigma_{xx} + \sigma_{xx}/\rho \\ \rho v_x v_z - \sigma_{xz} + \sigma_{xz}/\rho \\ 0 \\ 0 \\ 0 \end{pmatrix} \quad \text{and} \quad G^c = \begin{pmatrix} 0 \\ \rho v_x v_z - \sigma_{xz} + \sigma_{xz}/\rho \\ \rho v_z^2 - \sigma_{zz} + \sigma_{zz}/\rho \\ 0 \\ 0 \\ 0 \end{pmatrix}. \tag{5.29}$$

5.3.1 Numerical Implementation

In two dimensions, the physical domain of interest is discretized into cells, with subscript i for the x direction and j for the z direction. Cell dimensions are held constant throughout the computational domain with width Δx and height Δz. Time is discretized into time steps of duration Δt with superscript index n. Half-integral subscript indices represent edge values and half-integral superscript indices represent time-centered terms.

At the start of each time step, time step Δt is computed by determining the maximum

duration that satisfies the CFL condition:

$$L = \frac{\Delta t \left[\max_{ij}(|v_{x,ij}|, |v_{z,ij}|) + c_{\max}\right]}{\min(\Delta x, \Delta z)}, \tag{5.30}$$

where $c_{\max}$ is the maximum p-wave speed of the entire medium and L is the Courant number, taken to be 0.5 in this work. Next, the density of each cell is adjusted by evaluating the equation of state, and after, the spatial derivatives, or slopes, of each of the primitive variables of $\mathbf{q}$ are calculated. The slopes are fourth-order accurate and are constructed in two steps. First, a monotizing van Leer slope is computed in cell (i, j) for the x and z directions (van Leer, 1979):

$$\left(\frac{\partial \mathbf{q}}{\partial x}\right)_{ij}^{vL} = \text{sign}(\mathbf{q}_{i+1,j} - \mathbf{q}_{i-1,j}) \min\left(\frac{|\mathbf{q}_{i+1,j} - \mathbf{q}_{i-1,j}|}{2\Delta x}, \frac{2|\mathbf{q}_{i,j} - \mathbf{q}_{i-1,j}|}{\Delta x}, \frac{2|\mathbf{q}_{i+1,j} - \mathbf{q}_{i,j}|}{\Delta x}\right), \tag{5.31}$$

$$\left(\frac{\partial \mathbf{q}}{\partial z}\right)_{ij}^{vL} = \text{sign}(\mathbf{q}_{i,j+1} - \mathbf{q}_{i,j-1}) \min\left(\frac{|\mathbf{q}_{i,j+1} - \mathbf{q}_{i,j_1}|}{2\Delta z}, \frac{2|\mathbf{q}_{i,j} - \mathbf{q}_{i,j-1}|}{\Delta z}, \frac{2|\mathbf{q}_{i,j+1} - \mathbf{q}_{i,j}|}{\Delta z}\right). \tag{5.32}$$

Next, the fourth-order accurate slopes are generated in the x and z directions as

$$\left(\frac{\partial \mathbf{q}}{\partial x}\right)_{ij}^{4\text{th}} = \frac{\left(\left[\mathbf{q}_{i+1,j} - \frac{1}{4}\Delta x \left(\frac{\partial \mathbf{q}}{\partial x}\right)_{i+1,j}^{vL}\right] - \left[\mathbf{q}_{i-1,j} + \frac{1}{4}\Delta x \left(\frac{\partial \mathbf{q}}{\partial x}\right)_{i-1,j}^{vL}\right]\right)}{\frac{3}{2}\Delta x} \tag{5.33}$$

and

$$\left(\frac{\partial \mathbf{q}}{\partial z}\right)_{ij}^{4\text{th}} = \frac{\left(\left[\mathbf{q}_{i,j+1} - \frac{1}{4}\Delta z \left(\frac{\partial \mathbf{q}}{\partial z}\right)_{i,j+1}^{vL}\right] - \left[\mathbf{q}_{i,j-1} + \frac{1}{4}\Delta z \left(\frac{\partial \mathbf{q}}{\partial z}\right)_{i,j-1}^{vL}\right]\right)}{\frac{3}{2}\Delta z}. \tag{5.34}$$

The slopes are then limited in order to prevent oscillations from strong shocks by

$$\left(\frac{\partial \mathbf{q}}{\partial a}\right)_{ij} = \chi_{ij} \left(\frac{\partial \mathbf{q}}{\partial a}\right)_{ij}^{4\text{th}}, \tag{5.35}$$

where a is x or z and χ is a flattening parameter. Please refer to Appendix C for the details

in computing χ.

The slopes are then used to construct time-centered estimates of the primitive variable values at the cell edges. Evaluating Eq. (5.13) over a half time step yields estimates at four cell edges as illustrated in Figure 5.1. The L and R subscripts indicate left and right states to be defined in the Riemann problems posed below. The edge values are given by

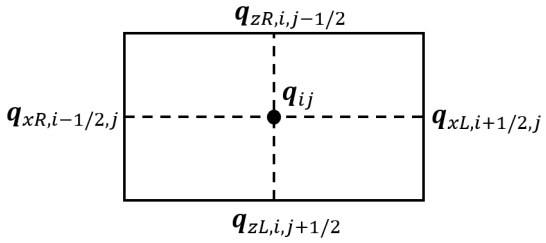

Figure 5.1: Computational cell (i, j) with edge value descriptions.

$$\mathbf{q}^{n+1/2}_{xR,i-1/2,j} = \mathbf{q}^{n}_{ij} - \frac{\Delta x}{2} X_{x,ij} \left(\frac{\Delta t}{\Delta x} \Lambda_{x,ij} + I \right) X^{-1}_{x,ij} \left(\frac{\partial \mathbf{q}}{\partial x} \right)_{ij} + \frac{\Delta t}{2} s_{ij} \tag{5.36}$$

$$\mathbf{q}^{n+1/2}_{xL,i+1/2,j} = \mathbf{q}^{n}_{ij} - \frac{\Delta x}{2} X_{x,ij} \left(\frac{\Delta t}{\Delta x} \Lambda_{x,ij} - I \right) X^{-1}_{x,ij} \left(\frac{\partial \mathbf{q}}{\partial x} \right)_{ij} + \frac{\Delta t}{2} s_{ij} \tag{5.37}$$

$$\mathbf{q}^{n+1/2}_{zR,i,j-1/2} = \mathbf{q}^{n}_{ij} - \frac{\Delta z}{2} X_{z,ij} \left(\frac{\Delta t}{\Delta z} \Lambda_{z,ij} + I \right) X^{-1}_{z,ij} \left(\frac{\partial \mathbf{q}}{\partial z} \right)_{ij} + \frac{\Delta t}{2} s_{ij} \tag{5.38}$$

$$\mathbf{q}^{n+1/2}_{zL,i,j+1/2} = \mathbf{q}^{n}_{ij} - \frac{\Delta z}{2} X_{z,ij} \left(\frac{\Delta t}{\Delta z} \Lambda_{z,ij} - I \right) X^{-1}_{z,ij} \left(\frac{\partial \mathbf{q}}{\partial z} \right)_{ij} + \frac{\Delta t}{2} s_{ij}, \tag{5.39}$$

assuming

$$\mathbf{q}_{i\pm1/2,j} = \mathbf{q}_{ij} \pm \left(\frac{\partial \mathbf{q}}{\partial x} \right)_{ij} \left(\frac{\Delta x}{2} \right) \tag{5.40}$$

and

$$\mathbf{q}_{i,j\pm1/2} = \mathbf{q}_{ij} \pm \left(\frac{\partial \mathbf{q}}{\partial z} \right)_{ij} \left(\frac{\Delta z}{2} \right). \tag{5.41}$$

To prevent spurious oscillations from developing, Eqs. (5.36)-(5.39) are made strictly upwind by filtering out the downwind characteristics using projection operators:

$$\mathbf{q}^{n+1/2}_{xR,i-1/2,j} = \mathbf{q}^{n}_{ij} - \frac{\Delta x}{2} X_{x,ij} P^{-}_{x} X^{-1}_{x,ij} \left(\frac{\partial \mathbf{q}}{\partial x}\right)_{ij} + \frac{\Delta t}{2} s_{ij} \tag{5.42}$$

$$\mathbf{q}^{n+1/2}_{xL,i+1/2,j} = \mathbf{q}^{n}_{ij} - \frac{\Delta x}{2} X_{x,ij} P^{+}_{x} X^{-1}_{x,ij} \left(\frac{\partial \mathbf{q}}{\partial x}\right)_{ij} + \frac{\Delta t}{2} s_{ij} \tag{5.43}$$

$$\mathbf{q}^{n+1/2}_{zR,i,j-1/2} = \mathbf{q}^{n}_{ij} - \frac{\Delta z}{2} X_{z,ij} P^{-}_{z} X^{-1}_{z,ij} \left(\frac{\partial \mathbf{q}}{\partial z}\right)_{ij} + \frac{\Delta t}{2} s_{ij} \tag{5.44}$$

$$\mathbf{q}^{n+1/2}_{zL,i,j+1/2} = \mathbf{q}^{n}_{ij} - \frac{\Delta z}{2} X_{z,ij} P^{+}_{z} X^{-1}_{z,ij} \left(\frac{\partial \mathbf{q}}{\partial z}\right)_{ij} + \frac{\Delta t}{2} s_{ij}, \tag{5.45}$$

where the projection matrix operators are defined as

$$(P^{-}_{x})_{\alpha\beta} = \begin{cases} \left(\frac{\Delta t}{\Delta x}(\Lambda_x)_{\alpha\alpha} + 1\right)\delta_{\alpha\beta} & (\Lambda_x)_{\alpha\alpha} \leq 0 \\ 0 & (\Lambda_x)_{\alpha\alpha} > 0 \end{cases} \tag{5.46}$$

$$(P^{+}_{x})_{\alpha\beta} = \begin{cases} \left(\frac{\Delta t}{\Delta x}(\Lambda_x)_{\alpha\alpha} - 1\right)\delta_{\alpha\beta} & (\Lambda_x)_{\alpha\alpha} \geq 0 \\ 0 & (\Lambda_x)_{\alpha\alpha} < 0 \end{cases} \tag{5.47}$$

$$(P^{-}_{z})_{\alpha\beta} = \begin{cases} \left(\frac{\Delta t}{\Delta z}(\Lambda_z)_{\alpha\alpha} + 1\right)\delta_{\alpha\beta} & (\Lambda_z)_{\alpha\alpha} \leq 0 \\ 0 & (\Lambda_z)_{\alpha\alpha} > 0 \end{cases} \tag{5.48}$$

$$(P^{+}_{z})_{\alpha\beta} = \begin{cases} \left(\frac{\Delta t}{\Delta z}(\Lambda_z)_{\alpha\alpha} - 1\right)\delta_{\alpha\beta} & (\Lambda_z)_{\alpha\alpha} \geq 0 \\ 0 & (\Lambda_z)_{\alpha\alpha} < 0 \end{cases} \tag{5.49}$$

Thus four approximate edge values are calculated for every cell (i, j). The values at edges shared by neighboring cells are used to pose Riemann problems. A Riemann problem is an initial values problem with a jump between constant left and right states. For example, at

the $(i+1/2, j)$ edge, the initial left and right states are given by $\mathbf{q}_{xL,i+1/2,j}$ (calculated from the (i,j) cell) and $\mathbf{q}_{xR,i+1/2,j}$ (calculated from the $(i+1,j)$ cell), respectively. This case is illustrated in Figure 5.2. Computationally, when looping through each cell (i,j) there are

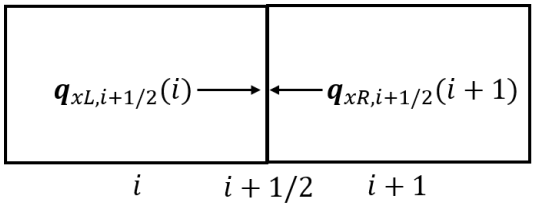

Figure 5.2: A Riemann problem is posed at each cell edge. In the x direction, the left (L) and right (R) states at the $(i+1/2)$ edge are derived from the (i) and $(i+1)$ cells, respectively.

two Riemann problems solved: one at the $(i+1/2, j)$ edge and one at the $(i, j+1/2)$ edge. The solution to the Riemann problems are approximated by decomposing the jumps between the left and right states in terms of the eigenvectors of A_x and A_z. For the $(i+1/2, j)$ edge, this is given by

$$\mathbf{q}^{n+1/2}_{xR,i+1/2,j} - \mathbf{q}^{n+1/2}_{xL,i+1/2,j} = X_x \boldsymbol{\phi}_x, \tag{5.50}$$

where the columns of X_x are evaluated with L or cell (i,j) properties if the corresponding eigenvalue is of the form $v_x - c$ or with R or cell $(i+1,j)$ properties if the corresponding eigenvalue is of the form $v_x + c$. The constructed X_x is then

$$X_x = \begin{bmatrix} 1 & 0 & -M_{xp}\rho_{ij} & 0 & -M_{xp}\rho_{i+1,j} & 0 \\ 0 & 0 & M_{xp}(c_p)_{ij} & 0 & -M_{xp}(c_p)_{i+1,j} & 0 \\ 0 & 0 & 0 & M_{xs}(c_s)_{ij} & 0 & -M_{xs}(c_s)_{i+1,j} \\ 0 & 0 & M_{xp}(\lambda_{ij}+2\mu_{ij}) & 0 & M_{xp}(\lambda_{i+1,j}+2\mu_{i+1,j}) & 0 \\ 0 & 1 & M_{xp}\lambda_{ij} & 0 & M_{xp}\lambda_{i+1,j} & 0 \\ 0 & 0 & 0 & M_{xs}\mu_{ij} & 0 & M_{xs}\mu_{i+1,j} \end{bmatrix}. \tag{5.51}$$

Likewise, at the $(i, j+1/2)$ edge, the decomposition is given by

$$\mathbf{q}^{n+1/2}_{zR,i,j+1/2} - \mathbf{q}^{n+1/2}_{zL,i,j+1/2} = X_z \boldsymbol{\phi}_z, \tag{5.52}$$

where

$$X_z = \begin{bmatrix} 1 & 0 & -M_{zp}\rho_{ij} & 0 & -M_{zp}\rho_{i,j+1} & 0 \\ 0 & 0 & 0 & M_{zs}(c_s)_{ij} & 0 & -M_{zs}(c_s)_{i,j+1} \\ 0 & 0 & M_{zp}(c_p)_{ij} & 0 & -M_{zp}(c_p)_{i,j+1} & 0 \\ 0 & 1 & M_{zp}\lambda_{ij} & 0 & M_{zp}\lambda_{i,j+1} & 0 \\ 0 & 0 & M_{zp}(\lambda_{ij}+2\mu_{ij}) & 0 & M_{zp}(\lambda_{i,j+1}+2\mu_{i,j+1}) & 0 \\ 0 & 0 & 0 & M_{zs}\mu_{ij} & 0 & M_{zs}\mu_{i,j+1} \end{bmatrix}. \tag{5.53}$$

It is assumed the constants M_{xp}, M_{xs}, M_{zp}, and M_{zs} remain unchanged between the left and right states.

The coefficients of the jump decomposition, $\boldsymbol{\phi}_x$ and $\boldsymbol{\phi}_z$, are used to determine the normal velocity of the edge discontinuities, $v^*_{x,i+1/2,j}$ and $v^*_{z,i,j+1/2}$, by adding to the left state the contribution of the $v-c$ group, or by subtracting from the right state the contribution of the $v+c$ group. For the $(i+1/2, j)$ edge this is

$$v^*_{x,i+1/2,j} = v^{*L}_x = v_{xL,i+1/2,j} + \phi_{x,3}(X_x)_{2,3} + \phi_{x,4}(X_x)_{2,4} \tag{5.54}$$

or

$$v^*_{x,i+1/2,j} = v^{*R}_x = v_{xR,i+1/2,j} - \phi_{x,5}(X_x)_{2,5} + \phi_{x,6}(X_x)_{2,6}, \tag{5.55}$$

and for the $(i, j+1/2)$ edge it is

$$v^*_{z,i,j+1/2} = v^{*L}_z = v_{zL,i,j+1/2} + \phi_{z,3}(X_x)_{3,3} + \phi_{z,4}(X_x)_{3,4} \tag{5.56}$$

or

$$v^*_{z,i,j+1/2} = v^{*R}_z = v_{zR,i,j+1/2} - \phi_{z,5}(X_x)_{3,5} + \phi_{z,6}(X_x)_{3,6}. \tag{5.57}$$

The normal direction edge velocities are taken to be the average of the L and R velocities:

$$v^*_{x,i+1/2,j} = \frac{1}{2}\left(v^{*L}_x + v^{*R}_x\right) \tag{5.58}$$

$$v^*_{z,i,j+1/2} = \frac{1}{2}\left(v^{*L}_z + v^{*R}_z\right). \tag{5.59}$$

These edge velocities are used to determine the appropriate upwind characteristics for reconstructing the remaining edge variables. If the edge velocity is positive, the variables are evaluated from the L state or from the R state if the edge velocity is negative. If the velocity is approximately zero then the L and R states are averaged. The variables for the $(i+1/2, j)$ edge are

$$\mathbf{q}^*_{i+1/2,j} = \begin{cases} \mathbf{q}_{xL,i+1/2,j} + \sum_1^6 w_{xL,\alpha}\phi_{x,\alpha}(\mathbf{x}_x)_\alpha & v^*_{x,i+1/2,j} > \epsilon \\ \mathbf{q}_{xR,i+1/2,j} - \sum_1^6 w_{xR,\alpha}\phi_{x,\alpha}(\mathbf{x}_x)_\alpha & v^*_{x,i+1/2,j} < -\epsilon \\ \frac{1}{2}\left(\mathbf{q}_{xL,i+1/2,j} + \mathbf{q}_{xR,i+1/2,j} + \sum_1^6 (w_{L,\alpha} - w_{R,\alpha})\phi_{x,\alpha}(\mathbf{x}_x)_\alpha\right) & |v^*_{x,i+1/2,j}| \le \epsilon \end{cases} \tag{5.60}$$

and for the $(i, j+1/2)$ edge the variables are

$$\mathbf{q}^*_{i,j+1/2} = \begin{cases} \mathbf{q}_{zL,i,j+1/2} + \sum_1^6 w_{zL,\alpha}\phi_{z,\alpha}(\mathbf{x}_z)_\alpha & v^*_{z,i,j+1/2} > \epsilon \\ \mathbf{q}_{zR,i,j+1/2} - \sum_1^6 w_{zR,\alpha}\phi_{z,\alpha}(\mathbf{x}_z)_\alpha & v^*_{z,i,j+1/2} < -\epsilon \\ \frac{1}{2}\left(\mathbf{q}_{zL,i,j+1/2} + \mathbf{q}_{zR,i,j+1/2} + \sum_1^6 (w_{L,\alpha} - w_{R,\alpha})\phi_{z,\alpha}(\mathbf{x}_z)_\alpha\right) & |v^*_{z,i,j+1/2}| \le \epsilon \end{cases} \tag{5.61}$$

where $\mathbf{x}_x$ and $\mathbf{x}_z$ are the column vectors of X_x and X_z, respectively, ϵ is a small parameter taken to be 10^{-9} in this work, and the filtering coefficients, w_{xL}, w_{xR}, w_{zL}, and w_{zR} are given

by

$$w_{xL,\alpha} = \begin{cases} 1 & (\Lambda_x)_{\alpha\alpha,L} - v_{x,i,j} + v^*_{x,i+1/2,j} < -\epsilon \\ 0 & \text{otherwise} \end{cases} \tag{5.62}$$

$$w_{xR,\alpha} = \begin{cases} 1 & (\Lambda_x)_{\alpha\alpha,R} - v_{x,i+1,j} + v^*_{x,i+1/2,j} > \epsilon \\ 0 & \text{otherwise} \end{cases} \tag{5.63}$$

$$w_{zL,\alpha} = \begin{cases} 1 & (\Lambda_z)_{\alpha\alpha,L} - v_{z,i,j} + v^*_{z,i,j+1/2} < -\epsilon \\ 0 & \text{otherwise} \end{cases} \tag{5.64}$$

$$w_{zR,\alpha} = \begin{cases} 1 & (\Lambda_z)_{\alpha\alpha,R} - v_{z,i,j+1} + v^*_{z,i,j+1/2} > \epsilon \\ 0 & \text{otherwise} \end{cases} \tag{5.65}$$

This procedure yields edge variable estimates ρ^*, v^*_x, v^*_z, σ^*_{xx}, σ^*_{zz}, and σ^*_{xz} at the $(i+1/2, j)$ and $(i, j+1/2)$ edges. These edge estimates are used to generate predictor fluxes $\tilde{F}$ and $\tilde{G}$ by

$$\tilde{F}_{i+1/2,j} = \begin{pmatrix} \rho^*_{i+1/2,j} v^*_{x,i+1/2,j} \\ \rho^*_{i+1/2,j} (v^*_{x,i+1/2,j})^2 - \sigma^*_{xx,i+1/2,j} \\ \rho^*_{i+1/2,j} v^*_{x,i+1/2,j} v^*_{z,i+1/2,j} - \sigma^*_{xz,i+1/2,j} \\ v^*_{x,i+1/2,j} \sigma^*_{xx,i+1/2,j} - (\lambda_{i+1/2,j} + 2\mu_{i+1/2,j}) v^*_{x,i+1/2,j} \\ v^*_{x,i+1/2,j} \sigma^*_{zz,i+1/2,j} - \lambda_{i+1/2,j} v^*_{x,i+1/2,j} \\ v^*_{x,i+1/2,j} \sigma^*_{xz,i+1/2,j} - \mu_{i+1/2,j} v^*_{z,i+1/2,j} \end{pmatrix} \tag{5.66}$$

$$\tilde{G}_{i,j+1/2} = \begin{pmatrix} \rho^*_{i,j+1/2} v^*_{z,i,j+1/2} \\ \rho^*_{i,j+1/2} v^*_{x,i,j+1/2} v^*_{z,i,j+1/2} - \sigma^*_{xz,i,j+1/2} \\ \rho^*_{i,j+1/2} (v^*_{z,i,j+1/2})^2 - \sigma^*_{zz,i,j+1/2} \\ v^*_{z,i,j+1/2} \sigma^*_{xx,i,j+1/2} - \lambda_{i,j+1/2} v^*_{z,i,j+1/2} \\ v^*_{z,i,j+1/2} \sigma^*_{zz,i,j+1/2} - (\lambda_{i,j+1/2} + 2\mu_{i,j+1/2}) v^*_{z,i,j+1/2} \\ v^*_{z,i,j+1/2} \sigma^*_{xz,i,j+1/2} - \mu_{i,j+1/2} v^*_{x,i,j+1/2} \end{pmatrix}, \tag{5.67}$$

where $\lambda_{i+1/2,j} = (\lambda_{i+1,j} + \lambda_{i,j})/2$, $\mu_{i+1/2,j} = (\mu_{i+1,j} + \mu_{i,j})/2$, $\lambda_{i,j+1/2} = (\lambda_{i,j+1} + \lambda_{i,j})/2$, and $\mu_{i,j+1/2} = (\mu_{i,j+1} + \mu_{i,j})/2$ are edge estimates of the elastic parameters. Likewise the nonlinear adjustment fluxes F^c and G^c are generated with

$$F^c_{i+1/2,j} = \begin{pmatrix} 0 \\ \rho^*_{i+1/2,j}(v^*_{x,i+1/2,j})^2 - \sigma^*_{xx,i+1/2,j} + \sigma^*_{xx,i+1/2,j}/\rho^*_{i+1/2,j} \\ \rho^*_{i+1/2,j} v^*_{x,i+1/2,j} v^*_{z,i+1/2,j} - \sigma^*_{xz,i+1/2,j} + \sigma^*_{xz,i+1/2,j}/\rho^*_{i+1/2,j} \\ 0 \\ 0 \\ 0 \end{pmatrix} \tag{5.68}$$

$$G^c_{i,j+1/2} = \begin{pmatrix} 0 \\ \rho^*_{i,j+1/2} v^*_{x,i,j+1/2} v^*_{z,i,j+1/2} - \sigma^*_{xz,i,j+1/2} + \sigma^*_{xz,i,j+1/2}/\rho^*_{i,j+1/2} \\ \rho^*_{i,j+1/2}(v^*_{z,i,j+1/2})^2 - \sigma^*_{zz,i,j+1/2} + \sigma^*_{zz,i,j+1/2}/\rho^*_{i,j+1/2} \\ 0 \\ 0 \\ 0 \end{pmatrix}. \tag{5.69}$$

These initial predictor and nonlinear adjustment fluxes are used to compute the corrector edge values by

$$\mathbf{q}'^{n+1/2}_{xR,i+1/2,j} = \mathbf{q}^{n+1/2}_{xR,i+1/2,j} - \frac{\Delta t}{2\Delta z}\left(\tilde{G}_{i,j+1/2} - \tilde{G}_{i,j-1/2}\right) + \frac{\Delta t}{2\Delta z}\left(G^c_{i,j+1/2} - G^c_{i,j-1/2}\right) \tag{5.70}$$

$$\mathbf{q}'^{n+1/2}_{xL,i+1/2,j} = \mathbf{q}^{n+1/2}_{xL,i+1/2,j} - \frac{\Delta t}{2\Delta z}\left(\tilde{G}_{i,j+1/2} - \tilde{G}_{i,j-1/2}\right) + \frac{\Delta t}{2\Delta z}\left(G^c_{i,j+1/2} - G^c_{i,j-1/2}\right) \tag{5.71}$$

$$\mathbf{q}'^{n+1/2}_{zR,i,j+1/2} = \mathbf{q}^{n+1/2}_{zR,i,j+1/2} - \frac{\Delta t}{2\Delta x}\left(\tilde{F}_{i+1/2,j} - \tilde{F}_{i-1/2,j}\right) + \frac{\Delta t}{2\Delta x}\left(F^c_{i+1/2,j} - F^c_{i-1/2,j}\right) \tag{5.72}$$

$$\mathbf{q}'^{n+1/2}_{zL,i,j+1/2} = \mathbf{q}^{n+1/2}_{zL,i,j+1/2} - \frac{\Delta t}{2\Delta x}\left(\tilde{F}_{i+1/2,j} - \tilde{F}_{i-1/2,j}\right) + \frac{\Delta t}{2\Delta x}\left(F^c_{i+1/2,j} - F^c_{i-1/2,j}\right). \tag{5.73}$$

The corrector edge values are used to pose two additional Riemann problems at the $(i+1/2, j)$ and $(i, j+1/2)$ edges in the same manner described previously. Approximate solutions to the Riemann problems are used to calculate the corrector fluxes, F and G, which are used in the final time update to compute cell-centered variables $\mathbf{U}$. The final time update is performed in two steps:

$$\tilde{\mathbf{U}}^{n+1}_{ij} = \mathbf{U}^n_{ij} - \frac{\Delta t}{\Delta x}\left(F_{i+1/2,j} - F_{i-1/2,j}\right) - \frac{\Delta t}{\Delta z}\left(G_{i,j+1/2} - G_{i,j-1/2}\right) \tag{5.74}$$

$$\mathbf{U}^{n+1}_{ij} = \tilde{\mathbf{U}}^{n+1}_{ij} + \Delta t S_{ij}. \tag{5.75}$$

The source terms, S_{ij}, are discretized as

$$S_{ij} = \begin{pmatrix} 0 \\ \rho^{n+1/2}_{ij} f^{n+1/2}_{x,ij} \\ \rho^{n+1/2}_{ij} f^{n+1/2}_{z,ij} \\ \sigma^{n+1/2}_{xx,ij}\left(\frac{v^*_{x,i+1/2,j} - v^*_{x,i-1/2,j}}{\Delta x} + \frac{v^*_{z,i,j+1/2} - v^*_{x,i,j-1/2}}{\Delta z}\right) \\ \sigma^{n+1/2}_{zz,ij}\left(\frac{v^*_{x,i+1/2,j} - v^*_{x,i-1/2,j}}{\Delta x} + \frac{v^*_{z,i,j+1/2} - v^*_{x,i,j-1/2}}{\Delta z}\right) \\ \sigma^{n+1/2}_{xz,ij}\left(\frac{v^*_{x,i+1/2,j} - v^*_{x,i-1/2,j}}{\Delta x} + \frac{v^*_{z,i,j+1/2} - v^*_{x,i,j-1/2}}{\Delta z}\right) \end{pmatrix}, \tag{5.76}$$

where the time-centered terms at the cell centers, $\mathbf{q}_{ij}^{n+1/2}$, are approximated with

$$\mathbf{q}_{ij}^{n+1/2} \approx \frac{1}{2}\left(\mathbf{q}_{ij}^{n} + \tilde{\mathbf{q}}_{ij}^{n+1}\right), \tag{5.77}$$

and the edge velocities, v^*, are components of the corrector Riemann solutions. Thus the solution is updated for the current time step.

5.3.2 Boundary Conditions

The numerical procedure as described requires transverse predictor fluxes to generate the solution. Therefore, the cells at the edge of the computational domain rely upon nonphysical, "ghost" fluxes directly outside the domain. The predictor fluxes are calculated using a high-order, 9-point stencil to approximate spatial slopes, so the ghost fluxes directly outside the boundaries require additional unphysical cells. In all, the procedure requires three additional ghost cells outside of every boundary. Boundary conditions are thus applied by adjusting variable values at the ghost cells. In what follows, boundary cell naming conventions follow that of Figure 5.3.

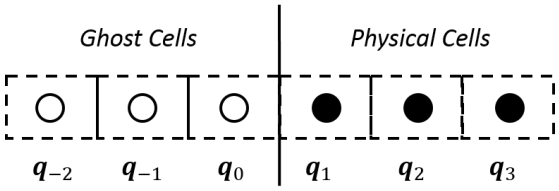

Figure 5.3: Ghost cell geometry and subscript notation.

In the case of an outflow boundary, all waves exit the boundary as if continuing into an infinite medium. The ghost cell values for this case are given by

$$\mathbf{q}_0 = \mathbf{q}_1, \quad \mathbf{q}_{-1} = \mathbf{q}_1, \quad \mathbf{q}_{-2} = \mathbf{q}_1. \tag{5.78}$$

In the case of a specified motion boundary, the velocity of the boundary is known throughout time. Let the velocity of the boundary be denoted by (U, V). The ghost cell values are

$$
\begin{aligned}
\text{for } \mathbf{q}_0: \quad & \rho_0 = \rho_1, \qquad v_{x,0} = 2U - v_{x,1}, \qquad v_{z,0} = 2V - v_{z,1}, \\
& \sigma_{xx,0} = \sigma_{xx,1}, \qquad \sigma_{zz,0} = \sigma_{zz,1}, \qquad \sigma_{xz,0} = \sigma_{xz,1}; \\
\text{for } \mathbf{q}_{-1}: \quad & \rho_{-1} = \rho_2, \qquad v_{x,-1} = 2U - v_{x,2}, \qquad v_{z,-1} = 2V - v_{z,2}, \\
& \sigma_{xx,-1} = \sigma_{xx,2}, \qquad \sigma_{zz,-1} = \sigma_{zz,2}, \qquad \sigma_{xz,-1} = \sigma_{xz,2}; \\
\text{for } \mathbf{q}_{-2}: \quad & \rho_{-2} = \rho_3, \qquad v_{x,-2} = 2U - v_{x,3}, \qquad v_{z,-2} = 2V - v_{z,3}, \\
& \sigma_{xx,-2} = \sigma_{xx,3}, \qquad \sigma_{zz,-2} = \sigma_{zz,3}, \qquad \sigma_{xz,-2} = \sigma_{xz,3}.
\end{aligned}
\tag{5.79}
$$

In the case of a specified traction boundary, the surface stress (traction) of the boundary is known throughout time. Let the normal stress of the boundary be denoted by T_{xx} and the parallel stress by T_{xz}. Note that σ_{xx} is the stress normal to the surface in the geometry presented in Figure 5.3; horizontal boundaries require specifying T_{zz}. The ghost cell values are

$$
\begin{aligned}
\text{for } \mathbf{q}_0: \quad & \rho_0 = \rho_1, \qquad v_{x,0} = v_{x,1}, \qquad v_{z,0} = v_{z,1}, \\
& \sigma_{xx,0} = 2T_{xx} - \sigma_{xx,1}, \qquad \sigma_{zz,0} = \sigma_{zz,1}, \qquad \sigma_{xz,0} = 2T_{xz} - \sigma_{xz,1}; \\
\text{for } \mathbf{q}_{-1}: \quad & \rho_{-1} = \rho_2, \qquad v_{x,-1} = v_{x,2}, \qquad v_{z,-1} = v_{z,2}, \\
& \sigma_{xx,-1} = 2T_{xx} - \sigma_{xx,2}, \qquad \sigma_{zz,-1} = \sigma_{zz,2}, \qquad \sigma_{xz,-1} = 2T_{xz} - \sigma_{xz,2}; \\
\text{for } \mathbf{q}_{-2}: \quad & \rho_{-2} = \rho_3, \qquad v_{x,-2} = v_{x,3}, \qquad v_{z,-2} = v_{z,3}, \\
& \sigma_{xx,-2} = 2T_{xx} - \sigma_{xx,3}, \qquad \sigma_{zz,-2} = \sigma_{zz,3}, \qquad \sigma_{xz,-2} = 2T_{xz} - \sigma_{xz,3}.
\end{aligned}
\tag{5.80}
$$

A special case of specified traction is the traction-free boundary where $T_{xx} = T_{xz} = 0$. Such is the case when the media encounters a free surface.

Finally, the last boundary considered in this work is that of a symmetry boundary. A symmetry boundary is one in which no flux can pass through and often is used to define a symmetry plane.

$$
\begin{aligned}
\text{for } \mathbf{q}_0: \quad & \rho_0 = \rho_1, \qquad v_{x,0} = -v_{x,1}, \qquad v_{z,0} = v_{z,1}, \\
& \sigma_{xx,0} = \sigma_{xx,1}, \qquad \sigma_{zz,0} = \sigma_{zz,1}, \qquad \sigma_{xz,0} = \sigma_{xz,1}; \\
\text{for } \mathbf{q}_{-1}: \quad & \rho_{-1} = \rho_2, \qquad v_{x,-1} = -v_{x,2}, \qquad v_{z,-1} = v_{z,2}, \\
& \sigma_{xx,-1} = \sigma_{xx,2}, \qquad \sigma_{zz,-1} = \sigma_{zz,2}, \qquad \sigma_{xz,-1} = \sigma_{xz,2}; \\
\text{for } \mathbf{q}_{-2}: \quad & \rho_{-2} = \rho_3, \qquad v_{x,-2} = -v_{x,3}, \qquad v_{z,-2} = v_{z,3}, \\
& \sigma_{xx,-2} = \sigma_{xx,3}, \qquad \sigma_{zz,-2} = \sigma_{zz,3}, \qquad \sigma_{xz,-2} = \sigma_{xz,3}.
\end{aligned}
\tag{5.81}
$$

Note that horizontal boundaries would require v_z to be negative across the boundary rather than v_x.

Artificial Absorbing Layer In certain situations the outflow boundary condition is incapable of absorbing all of the exiting wave energy. Specifically, in cases when waves are propagating parallel to the boundary or during long simulations the outflow boundary condition can "leak" unrealistic energy into the domain which eventually contaminates the entire calculation (Zhou & Wang, 2010). One method to prevent this numerical reflection is to apply an absorbing sponge zone (ASZ) to the outflowing boundaries. Within the ASZ, the solution is slowly translated into a target solution. This is done by adding the following expression to the source term within the governing equations:

$$-\tau_s(\mathbf{U} - \bar{\mathbf{U}}), \tag{5.82}$$

where τ_s is the sponge strength and $\bar{\mathbf{U}}$ is the reference or target solution within the ASZ, taken to be equal to the unperturbed state of the medium which represents the physically correct radiation condition. The sponge strength τ_s is equal to zero within the physical domain and grows smoothly within the ASZ. It can be shown that the convergence rate to the target solution is inversely proportional to the sponge strength (Bodony, 2006). Numerically, the ASZ is implemented by changing Eq. (5.75) to

$$\mathbf{U}_{ij}^{n+1} = \tilde{\mathbf{U}}_{ij}^{n+1} + \Delta t[S_{ij} - \tau_{s,ij}(\tilde{\mathbf{U}}_{ij} - \bar{\mathbf{U}}_{ij})]. \tag{5.83}$$

5.3.3 Model Verification

Sample calculations are performed to verify the stationary elastic model. Example problems are chosen to illustrate various aspects of the model such as shock steepening, scattering, refraction, and diffraction of pressure and shear waves. Ultimately, these are the aspects desired in a long-range shock propagation model.

The equation of state applied to the example problems is a linear sound speed formulation given by

$$\rho = \frac{1}{c_p}(p - p_0) + \rho_0, \tag{5.84}$$

where c_p is the p-wave speed of the medium (small-signal acoustic sound speed) and ρ_0 is the density at a given ambient pressure p_0. For a two-dimensional solid, the pressure is approximated as an average of the normal stresses, $p = -\frac{1}{2}(\sigma_{xx} + \sigma_{zz})$.

In general, this equation of state is only accurate at lower pressures, so solutions presented here may not necessarily capture the true physics of the problem. However, the aspects of the model being examined will remain largely unaffected by the choice of the equation of state. More advanced equations of state are currently being implemented.

Pressure Relaxation Example A simple pseudo-one-dimensional problem is analyzed to investigate the effect of relaxing a pre-stressed medium. In this example, parameter values are unitless but are assumed to be consistent with each other. A Gaussian pressure pulse is applied at the center of the domain which is then allowed to dissipate starting at $t = 0$. The length of the domain is 8 and the x direction grid spacing (cell width) is 0.01. The left and right sides of the domain are set to outflowing boundaries. The stationary model is two-dimensional, so to recreate a one-dimensional situation the height of the domain is set to 0.1 and the top and bottom boundaries are set to symmetry boundaries. The material parameters are $\rho = 1$, $\lambda = 2$, $\mu = 1$. Results of the simulation are given in Figure 5.4 below. The plots show the pressure pulse decay and transform into right and left traveling waves. As the waves travel down the domain, the effect of nonlinear steepening is clearly observed as shocks develop at the pulse fronts.

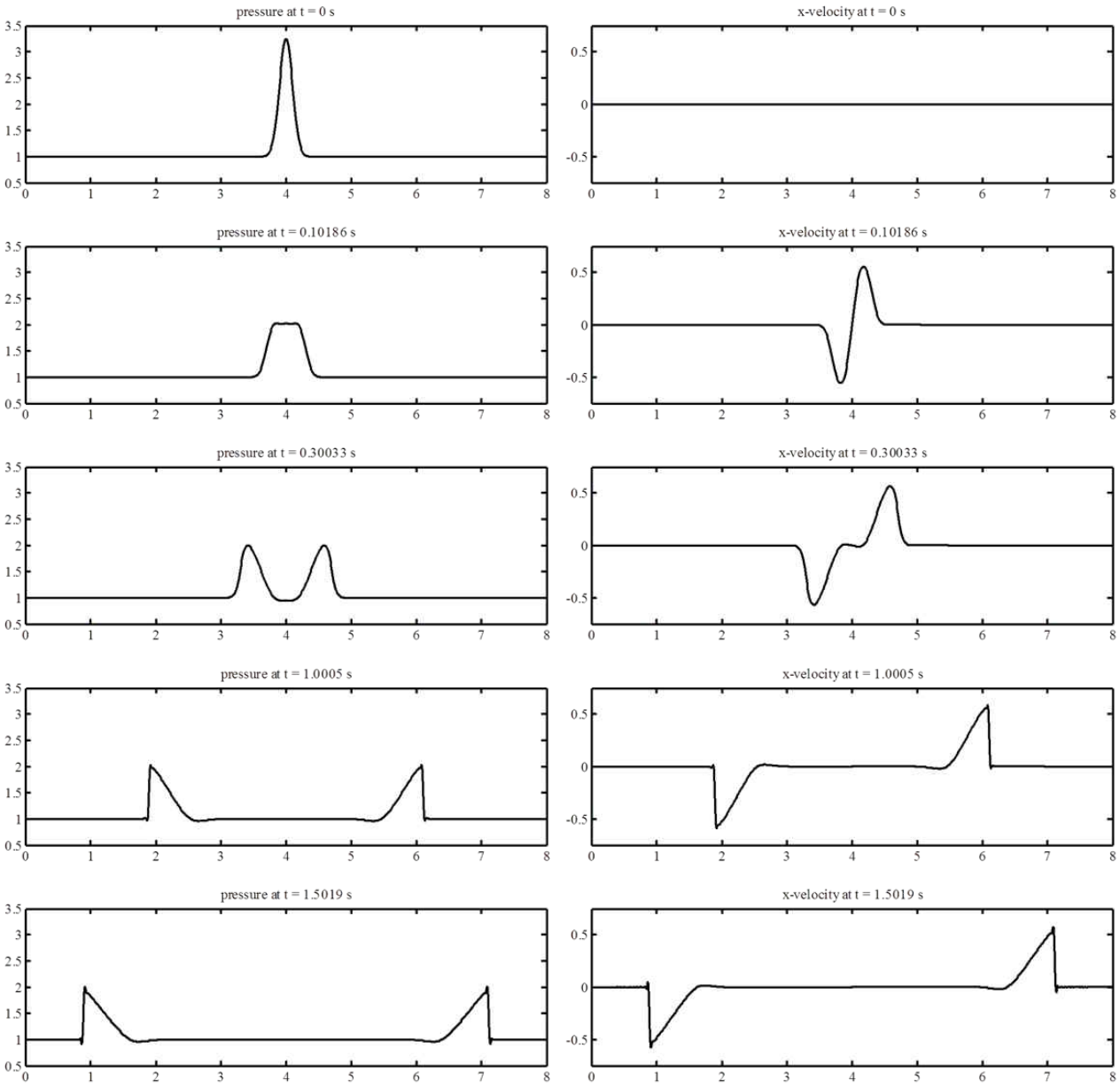

Figure 5.4: Verification example illustrating the dissipation of an initial Gaussian pressure distribution. Left column: pressure. Right column: x velocity

Wave Propagation in a Heterogeneous Medium A two-dimensional problem is considered here to demonstrate elastic wave propagation in a discontinuous, heterogeneous medium. The numerical scheme is based on a high-order Godunov approach which can not only treat jumps in variable states but also jumps in elastic properties. This example is taken from *Finite Volume Methods for Hyperbolic Problems* (LeVeque, 2002) in order to qualitatively compare results. It is noted, however, that results from (LeVeque, 2002) are based on the linear elastic wave equation solution and therefore do not include nonlinear steepening and shock formation.

Consider a wave propagating into a solid that has embedded within it an inclusion made out of a stiffer material. The elastic properties of the less stiff material are $\lambda = 2$ and $\mu = 1$, and the properties of the stiff material are $\lambda = 200$ and $\mu = 100$. The density is the same everywhere, $\rho = 1$. The computational grid has a length of 2 and a height of 1, and the x and z direction grid spacing (cell width and height) are both 0.01. The top and bottom of the domain are set to traction-free boundaries, and the right-hand side of the domain is set to an outflowing boundary. At the left-hand side of the domain, at $x = 0$, the x velocity is specified as

$$v_x(t) = \begin{cases} 0.001 \sin(\pi t/0.025) & t<0.025 \\ 0 & t \geq 0.025 \end{cases} \tag{5.85}$$

Thus, the left boundary is pushed a small amount to induce a traveling compressional wave. The resulting wave motion is shown in the plots of Figure 5.5. The plots show pressure and shear fields as the compressional wave interacts with the stiffer material. When the initial pressure wave hits the stiff material it generates a reflected pressure and shear wave and a weaker set of transmitted pressure and shear waves into the stiff material. The plots also show how the traction-free boundaries cause development of shear waves at the points where the compressional wave contacts. These results compare well to (LeVeque, 2002) with a few minor differences. The stationary elastic model includes nonlinear steepening so the waves are slightly faster than the text's results.

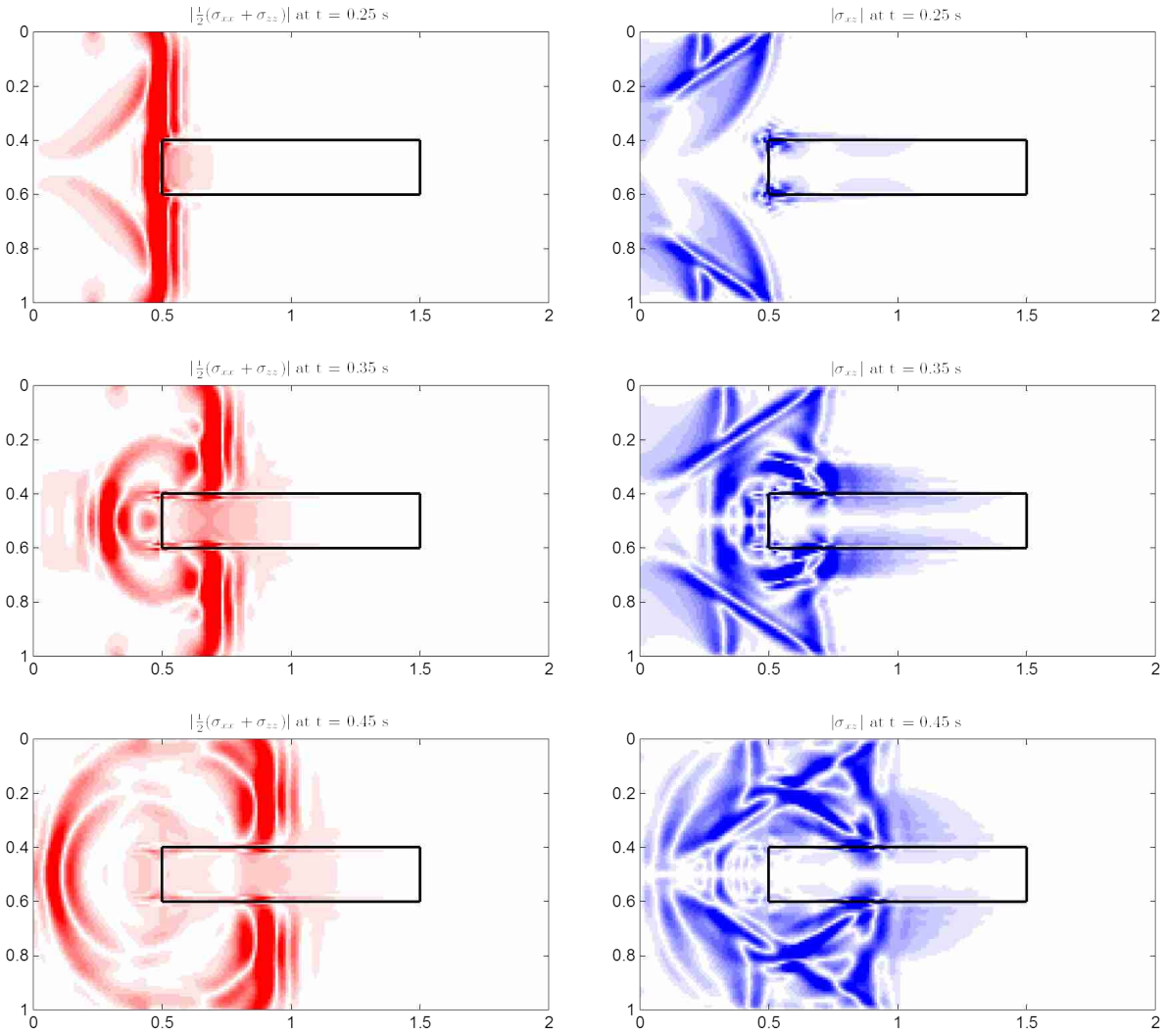

Figure 5.5: Elasticity example for comparing to results in *Finite Volume Methods for Hyperbolic Problems*, (LeVeque, 2002). Left column: average normal stress, $|\frac{1}{2}(\sigma_{xx}+\sigma_{zz})|$. Right column: shear stress, $|\sigma_{xz}|$.

Surface Explosion over Layered Media As a final example, blast wave propagation through layered media is analyzed with the stationary elastic model. This example is more in line with the final application towards shock propagation in ocean waveguides. The environment of the problem is a layered rock half space, 100 m deep and 200 m long such as seen in Figure 5.6. Material 1 has elastic properties $\lambda = 15$ GPa, $\mu = 33$ GPa, and $\rho = 2.7$ g/cm^3. Values such as these are representative of a dense hard rock such as granite. Material 2 has elastic properties $\lambda = 5$ GPa, $\mu = 30$ GPa, and $\rho = 2.6$ g/cm^3 which are representative of a slightly less dense rock such as limestone. Linear elastic material models are not entirely accurate as solid rock often exhibits varying degrees of anisotropy. However, at the length scale of interest, an isotropic linear elastic assumption provides adequate results and have been employed in numerous ocean acoustic and geophysics models (Jensen *et al.*, 2005), (Collins, 1993b), (Zahradnik & Priolo, 1995).

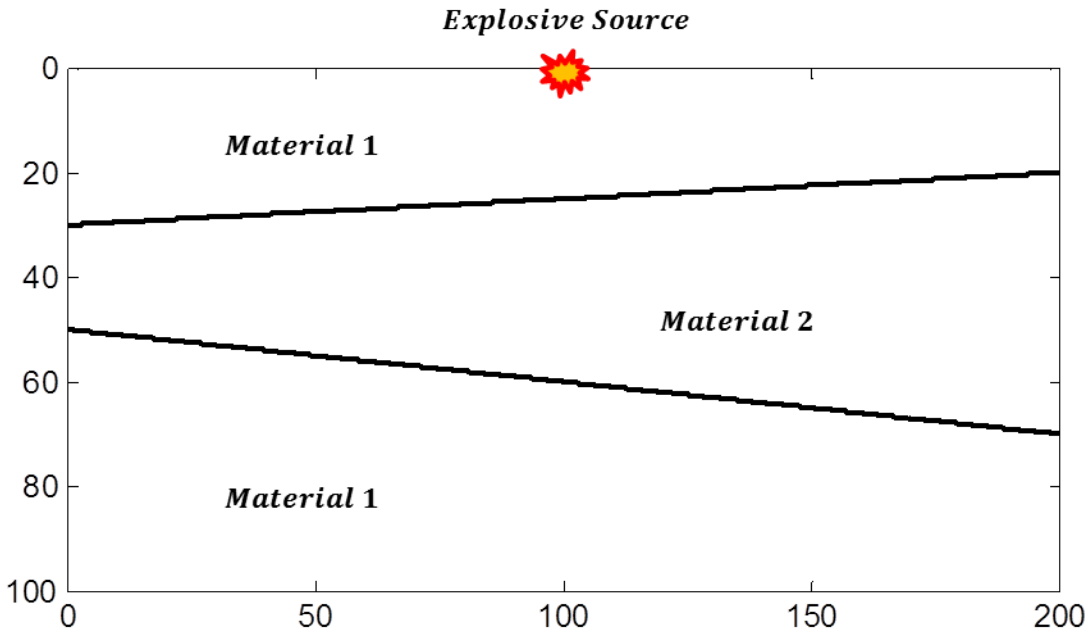

Figure 5.6: Environment used in the surface explosion example (axis gradations are in meters). Material 1 properties are similar to that of a dense rock such as granite. Material 2 properties are similar to that of a more porous rock such as limestone.

The explosion is simulated using a forcing input source. The source is located at the surface of the domain, halfway down range at $(100, 0)$. The shape of the source is a semicircle with a 5 m radius. The forcing function is applied to all cells that fall on the perimeter of the semicircle source and is given by

$$\mathbf{f}(t) = 10e^{-t/t^*}(1 - t/t^*)\mathbf{e}_n, \tag{5.86}$$

where the positive phase duration $t^* = 0.2$ ms and $\mathbf{e}_n$ represents the vector normal to the perimeter of the semicircle. The forcing function is decomposed into its x and z direction components to attain f_x and f_z. A pressure release condition is imposed on the top boundary of the computational domain, and outflow conditions are applied to the left, right, and lower boundaries to allow for wave energy to propagate out of the domain. Artificial absorbing layers are not applied to the outflow boundaries here because the simulation time is short enough to prevent unrealistic energy "leakage". Finally, a cell width and height of 0.5 m is used for the entire computational domain.

The results of the simulation, presented in Figure 5.7, show the explosion generates both pressure and shear waves which propagate into the half space. When the waves first encounter Material 2 there is not an appreciable reflection as almost all energy is transmitted to the less dense material. When the waves encounter the bottom Material 1, however, a more substantial reflection is generated. Note that an s-wave is generated at any point along an interface or boundary where a p-wave has contact, a physically accurate result. The results also illustrate the effect refraction as the wave appears to change shape in between areas of different velocities. This example exhibits the effectiveness of the stationary elastic model in describing shock propagation through an environment that may be encountered in the ocean bottom.

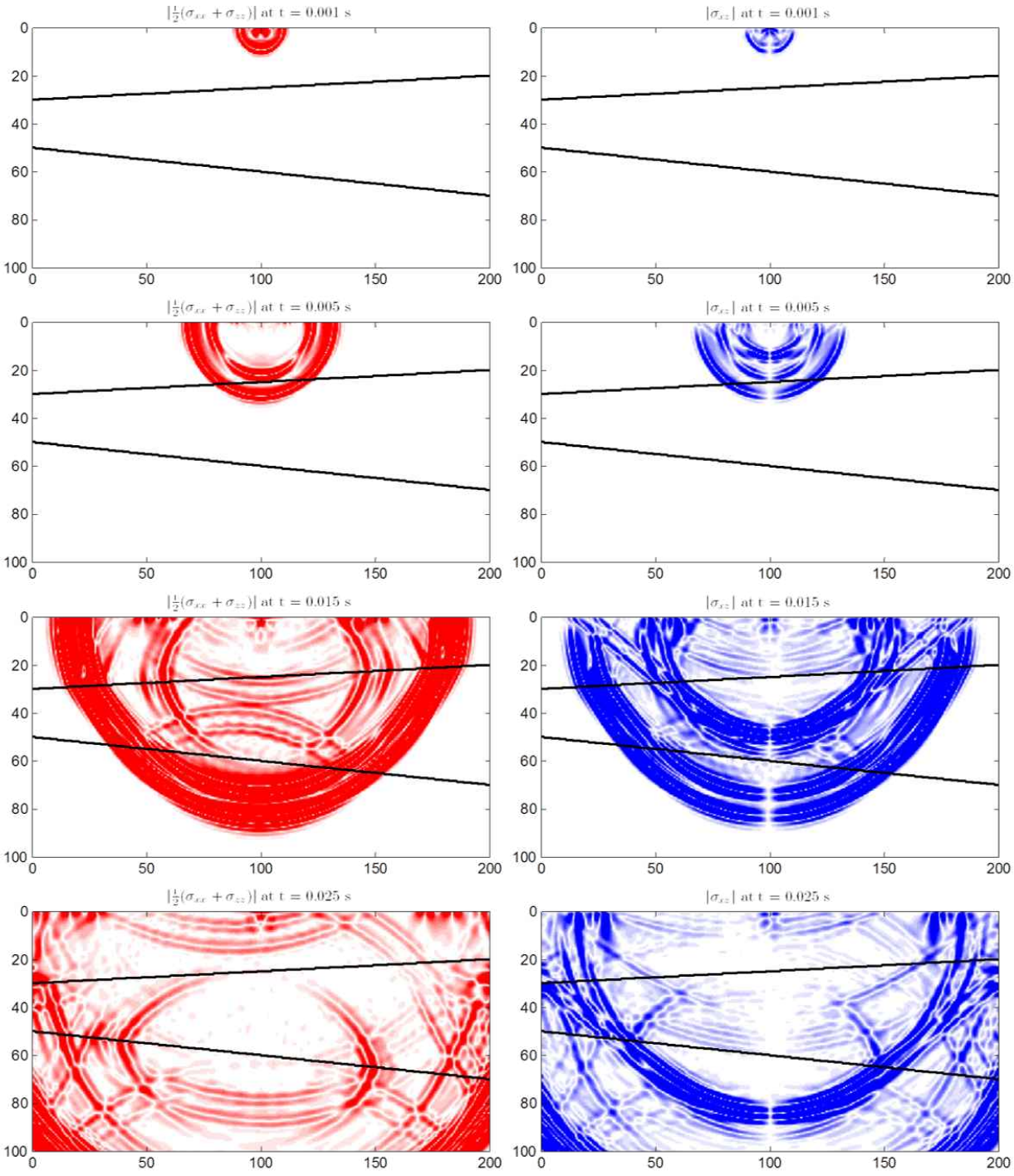

Figure 5.7: Blast wave propagation in an environment containing dissimilar material layers. Left column: average normal stress, $|\frac{1}{2}(\sigma_{xx}+\sigma_{zz})|$. Right column: shear stress, $|\sigma_{xz}|$.

5.4 Elastic Progressive Model

The stationary model is capable of accurately describing nonlinear elastic wave propagation in discontinuous, heterogeneous media. However, it is not effective modeling large distances because the number of computational cells needed becomes unmanageable. Here, the stationary model is adapted to a progressive one in which the governing equations are recast in a moving computational domain that tracks the wavefront. This allows the shock front and initial reflections to be captured at far distances, but at the expense of losing back-scattered energy.

Consider a two-dimensional, rectangular domain that propagates along the x axis at a specified velocity, c_{win}. The governing equations are recast into the computational domain by replacing the time derivative with its material derivative counterpart:

$$\frac{D}{Dt} = \frac{\partial}{\partial t} - c_{\text{win}} \frac{\partial}{\partial x}. \tag{5.87}$$

The set of quasi-conservative governing equations, (5.10), now become

$$\frac{\partial}{\partial t}\begin{pmatrix} \rho \\ \rho v_x \\ \rho v_z \\ \sigma_{xx} \\ \sigma_{zz} \\ \sigma_{xz} \end{pmatrix} + \frac{\partial}{\partial x}\begin{pmatrix} \rho v_x - c_{\text{win}}\rho \\ \rho v_x^2 - \sigma_{xx} - c_{\text{win}}\rho v_x \\ \rho v_x v_z - \sigma_{xz} - c_{\text{win}}\rho v_z \\ v_x\sigma_{xx} - (\lambda+2\mu)v_x - c_{\text{win}}\sigma_{xx} \\ v_x\sigma_{zz} - \lambda v_x - c_{\text{win}}\sigma_{zz} \\ v_x\sigma_{xz} - \mu v_z - c_{\text{win}}\sigma_{xz} \end{pmatrix} + \frac{\partial}{\partial z}\begin{pmatrix} \rho v_z \\ \rho v_x v_z - \sigma_{xz} \\ \rho v_z^2 - \sigma_{zz} \\ v_z\sigma_{xx} - \lambda v_z \\ v_z\sigma_{zz} - (\lambda+2\mu)v_z \\ v_z\sigma_{xz} - \mu v_x \end{pmatrix} = \begin{pmatrix} 0 \\ \rho f_x \\ \rho f_z \\ \sigma_{xx}\dot{\Delta} \\ \sigma_{zz}\dot{\Delta} \\ \sigma_{xz}\dot{\Delta} \end{pmatrix}, \tag{5.88}$$

where $\dot{\Delta} = \left(\frac{\partial v_x}{\partial x} + \frac{\partial v_z}{\partial z}\right)$. The temporal material derivative is also applied to the linearized equations, (5.13), (presented in the vector form for simplicity) by

$$\frac{\partial \mathbf{q}}{\partial t} + (A_x - c_{\text{win}} I)\frac{\partial \mathbf{q}}{\partial x} + A_z \frac{\partial \mathbf{q}}{\partial z} = \mathbf{s}. \tag{5.89}$$

A new progressive x direction matrix, A_{xp}, is defined by $A_{xp} = A_x - c_{\text{win}}I$. The eigenvalue decomposition of this matrix is given by

$$A_{xp} = X_x \Lambda_{xp} X_x^{-1}, \tag{5.90}$$

where left and right eigenvector matrices, X_x and X_x^{-1}, remain the same and are given by (5.17) and (5.19), respectively. The diagonal matrix of eigenvalues does change, however, and is given by

$$\Lambda_{xp} = \begin{bmatrix} v_x - c_{\text{win}} & 0 & 0 & 0 & 0 & 0 \\ 0 & v_x - c_{\text{win}} & 0 & 0 & 0 & 0 \\ 0 & 0 & v_x - c_{\text{win}} - c_p & 0 & 0 & 0 \\ 0 & 0 & 0 & v_x - c_{\text{win}} - c_s & 0 & 0 \\ 0 & 0 & 0 & 0 & v_x - c_{\text{win}} + c_p & 0 \\ 0 & 0 & 0 & 0 & 0 & v_x - c_{\text{win}} + c_s \end{bmatrix}. \tag{5.91}$$

Therefore, the characteristics of wave propagation in the x direction can be interpreted as being equal to those of the stationary case but with an effective velocity of $v_x - c_{\text{win}}$. Following a procedure similar to that of the stationary elastic model, a new nonlinear adjustment flux is composed for the x direction:

$$F_p^c = \begin{pmatrix} 0 \\ \rho v_x (v_x - c_{\text{win}}) - \sigma_{xx} + \sigma_{xx}/\rho \\ \rho v_z (v_x - c_{\text{win}}) - \sigma_{xz} + \sigma_{xz}/\rho \\ 0 \\ 0 \\ 0 \end{pmatrix}. \tag{5.92}$$

The expressions for the z direction remain unchanged from those of the stationary model

because the depth operator is unaffected by the transformation into a moving domain.

5.4.1 Numerical Implementation

Numerical implementation follows the same method as for the stationary elastic model, described in the previous section. The aspects affected by the coordinate transformation are noted here. Generally speaking, these aspects are resolved by applying an effective x velocity, $v_x - c_{\text{win}}$, to the operations.

First, the maximum time step can be computed by determining if left-going waves are present. If so, the time step must be short enough to resolve these waves according to a CFL condition. If no left-going waves are present, then only right-going waves and waves in the z direction must be captured. This leads to the following three conditions:

$$L = \frac{\Delta t_1 \left(|\min_{ij}(v_{x,ij})| + c_{\max} + c_{\text{win}}\right)}{\min(\Delta x, \Delta z)} \tag{5.93a}$$

$$L = \frac{\Delta t_2 \left(|\max_{ij}(v_{x,ij})| + c_{\max} - c_{\text{win}}\right)}{\min(\Delta x, \Delta z)} \tag{5.93b}$$

$$L = \frac{\Delta t_3 \left(\max_{ij}(|v_{z,ij}|) + c_{\max}\right)}{\min(\Delta x, \Delta z)}, \tag{5.93c}$$

where the Courant number, L, is set to 0.5. The time step is taken to be the minimum step satisfied by the conditions: $\Delta t = \min(\Delta t_1, \Delta t_2, \Delta t_3)$.

The slopes are computed in the same manner as before, using Eqs. (5.31) – (5.35). Next, the time-centered estimates of the primitive variables at the cell edges are calculated in the same way, except the diagonal eigenvalue matrix, Λ_x, is replaced with the progressive matrix, Λ_{xp}, in Eqs. (5.46) and (5.47). These edge value estimates are again used to pose Riemann problems at the cells edges. However, the interfacial velocity must be augmented to account for the velocity of the moving domain. The variables for the $(i + 1/2, j)$ edge are computed by Eq. (5.60), however the filtering coefficients, w_{xL} and w_{xR}, are now given by

$$w_{xL,\alpha} = \begin{cases} 1 & (\Lambda_{xp})_{\alpha\alpha,L} - v_{x,i,j} + v^*_{x,i+1/2,j} < -\epsilon \\ 0 & \text{otherwise} \end{cases} \tag{5.94}$$

$$w_{xR,\alpha} = \begin{cases} 1 & (\Lambda_{xp})_{\alpha\alpha,R} - v_{x,i+1,j} + v^*_{x,i+1/2,j} > \epsilon \\ 0 & \text{otherwise} \end{cases} \tag{5.95}$$

Solutions to the Riemann problem yeild edge variable estimates ρ^*, v^*_x, v^*_z, σ^*_{xx}, σ^*_{zz}, and σ^*_{xz} at the $(i+1/2, j)$ edge. These edge estimates are used to form the predictor flux for the progressive interface, $\tilde{F}_p$:

$$\tilde{F}_{p,i+1/2,j} = \begin{pmatrix} \rho^*_{i+1/2,j}(v^*_{x,i+1/2,j} - c_{\text{win}}) \\ \rho^*_{i+1/2,j} v^*_{x,i+1/2,j}(v^*_{x,i+1/2,j} - c_{\text{win}}) - \sigma^*_{xx,i+1/2,j} \\ \rho^*_{i+1/2,j} v^*_{z,i+1/2,j}(v^*_{x,i+1/2,j} - c_{\text{win}}) - \sigma^*_{xz,i+1/2,j} \\ (v^*_{x,i+1/2,j} - c_{\text{win}})\sigma^*_{xx,i+1/2,j} - (\lambda_{i+1/2,j} + 2\mu_{i+1/2,j}) v^*_{x,i+1/2,j} \\ (v^*_{x,i+1/2,j} - c_{\text{win}})\sigma^*_{zz,i+1/2,j} - \lambda_{i+1/2,j} v^*_{x,i+1/2,j} \\ (v^*_{x,i+1/2,j} - c_{\text{win}})\sigma^*_{xz,i+1/2,j} - \mu_{i+1/2,j} v^*_{z,i+1/2,j} \end{pmatrix}, \tag{5.96}$$

where the elastic parameters are taken to be averages of the values from the left and right states. Likewise, the progressive nonlinear adjustment flux, F^c_p, is computed with

$$F^c_{p,i+1/2,j} = \begin{pmatrix} 0 \\ \rho^*_{i+1/2,j} v^*_{x,i+1/2,j}(v^*_{x,i+1/2,j} - c_{\text{win}}) - \sigma^*_{xx,i+1/2,j} + \sigma^*_{xx,i+1/2,j}/\rho^*_{i+1/2,j} \\ \rho^*_{i+1/2,j} v^*_{z,i+1/2,j}(v^*_{x,i+1/2,j} - c_{\text{win}}) - \sigma^*_{xz,i+1/2,j} + \sigma^*_{xz,i+1/2,j}/\rho^*_{i+1/2,j} \\ 0 \\ 0 \\ 0 \end{pmatrix} \tag{5.97}$$

The Riemann solver does not change for the $(i, j+1/2)$ edge as the characteristic speeds in the z direction and the velocity of the interface are not affected by the coordinate transformation.

Again, corrector edge values are computed with Eqs. (5.70) – (5.73), however, the new progressive fluxes are employed where necessary. The final step is updating the conserved

variables, $\mathbf{U}$, which is done with

$$\tilde{\mathbf{U}}_{ij}^{n+1} = \mathbf{U}_{ij}^{n} - \frac{\Delta t}{\Delta x}\left(F_{p,i+1/2,j} - F_{p,i-1/2,j}\right) - \frac{\Delta t}{\Delta z}\left(G_{i,j+1/2} - G_{i,j-1/2}\right) \tag{5.98}$$

$$\mathbf{U}_{ij}^{n+1} = \tilde{\mathbf{U}}_{ij}^{n+1} + \Delta t S_{ij}, \tag{5.99}$$

where S_{ij} is unchanged and is given by Eq. (5.76).

5.4.2 Model Verification

Sample calculations are presented here to verify that the physics captured with the stationary elastic model have not been lost with the coordinate transformation into a progressive model. The first simulation describes the transformation of a square shock wave as it propagates in an unbounded medium, and the second simulation recreates the results of the stationary heterogeneous medium example presented prior. Both example problems use a linear, sound speed-based equation of state and assume thermal effects at the shock front are negligible.

Decay of a Strong Square Shock A study is presented here to verify the computation of the decay of a strong square shock. This problem will also serve as a mesh convergence study to determine what effect the resolution of the mesh has on the solution. The environment used in the study is an elastic solid with a density of $\rho_0 = 2700$ kg/m^3 and elastic parameters $\lambda = 15$ GPa and $\mu = 33$ GPa. The initial waveform used in the study, displayed in Figure 5.8 below, is a 10 m long square shock with the following primitive variable values:

$$\begin{aligned} \rho &= 1.1\rho_0 & v_x &= 1.1\sqrt{\frac{\lambda+2\mu}{\rho_0}} & v_z &= 0 \\ \sigma_{xx} &= -1.1(\lambda+2\mu) & \sigma_{zz} &= -1.1\lambda & \sigma_{xz} &= 0. \end{aligned} \tag{5.100}$$

The 1D computational domain is 50 m long and the grid spacing is set to 1.0, 0.5, 0.25, and 0.125 m to allow for 50, 100, 200, and 400 points in the mesh, respectively. The length of the time step is set according to a CFL number of 0.5, and the shock is propagated for a total of 5 ms. The results are given below in Figure 5.9 and show that the solution does not have a strong dependence on the mesh. The rate of convergence computed using the L^1 of the pressure profiles is found to be 1.01. It should be noted that the square shock devolves into its shocked-up form much faster than seen with the NPE models because two-way propagation is captured with the finite-volume models described in this chapter.

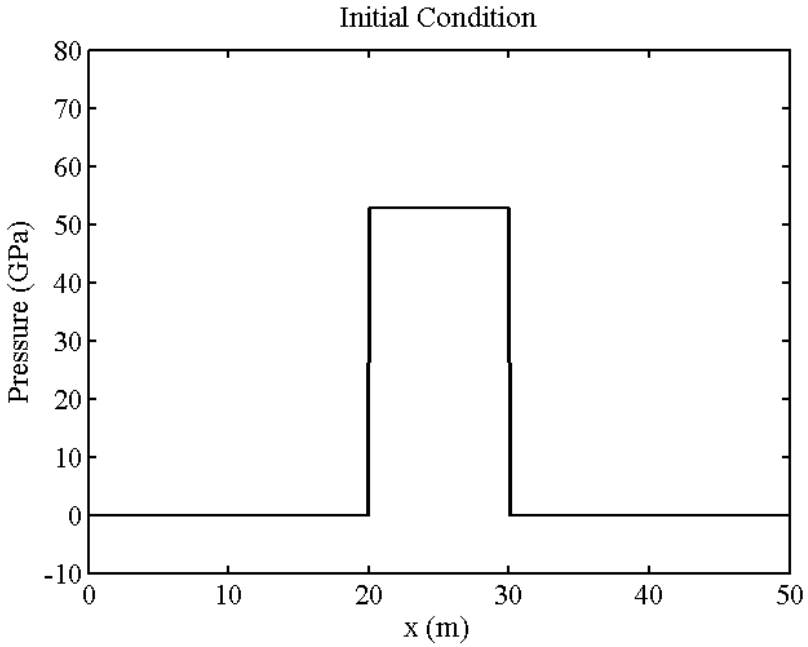

Figure 5.8: Initial condition for mesh convergence study.

Wave Propagation in a Heterogeneous Medium The same problem presented in Section 5.3.3 for an elastic wave propagating in a discontinuous, heterogeneous medium is evaluated using the elastic progressive model. The same environment is used, but now the computational grid has a length of 0.4 and a height of 1. The same x and z direction grid spacing of 0.01 is employed, and traction-free boundary conditions are applied to the top

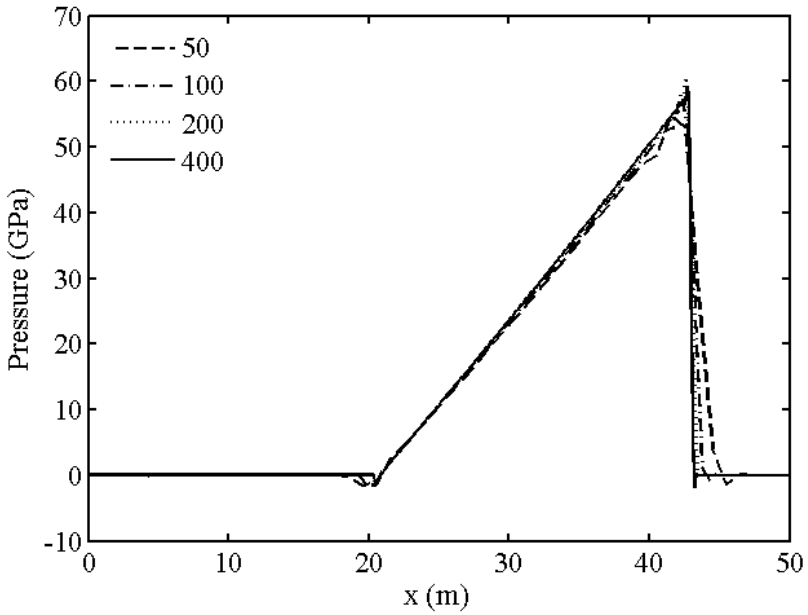

Figure 5.9: Waveform at t = 5 ms for the mesh convergence study.

and bottom boundaries. The right-hand side of the domain is set to an outflowing boundary. When t<0.115, the domain is stationary with $c_{\text{win}} = 0$ and the left-hand side of the domain has a specified velocity condition described by Eq. (5.85). At $t = 0.115$, the domain becomes progressive and traverses down the x direction with a velocity $c_{\text{win}} = 2$, which is equal to the compressional wave speed of the less stiff outer material. The left-hand side of the domain is then set to an outflowing boundary. The outflowing boundaries on the left and right sides are complemented with an absorbing sponge zone with a thickness of 0.06. The results are given in Figure 5.10 and show that general wave motion is captured when compared to the stationary model's results. The progressive model is much more efficient, but it is only able to compute the solution within a narrow range. The reflected wave that travels to the left and fast wave that runs through the stiff material are lost. However, the main compressional wave is accurately captured, which is the main interest for long-range underwater shock problems.

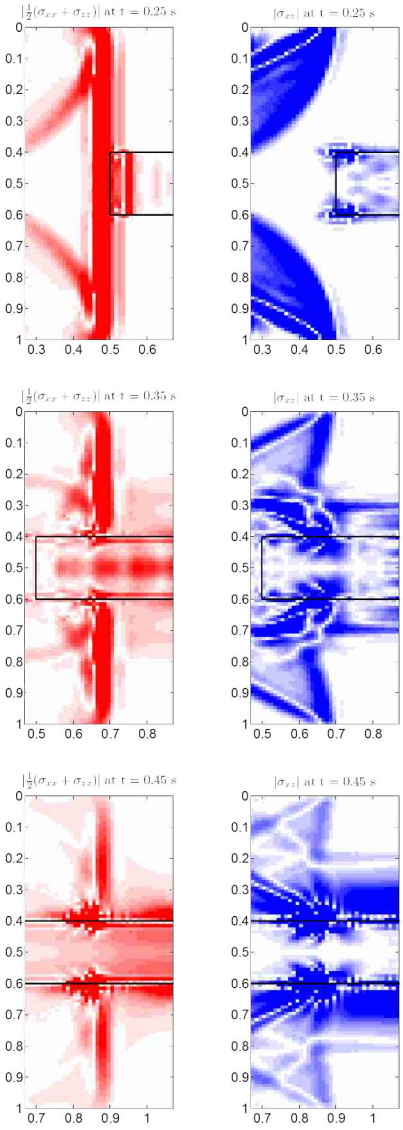

Figure 5.10: Progressive model example for comparing to results in *Finite Volume Methods for Hyperbolic Problems*, (LeVeque, 2002). Left column: average normal stress, $|\frac{1}{2}(\sigma_{xx}+\sigma_{zz})|$. Right column: shear stress, $|\sigma_{xz}|$.

5.5 Elastic-Fluid Progressive Model

The elastic progressive model has shown to be accurate in fully elastic media, but an ocean waveguide model must be able to describe wave propagation in the water column as well. In this section, the elastic model is coupled with a fluid shock model using appropriate interface conditions, and then cast into a progressive computational domain. Numerical procedures remain unchanged, and this final model is then benchmarked against experimental results as a final validation.

The governing equations for a fluid media can be seen as a special case of the fully elastic equations wherein shear stress is not supported and the components of the normal stresses are equal to the hydrostatic pressure. The governing equations for nonlinear wave propagation in a fluid, in two dimensions are given by

$$\frac{\partial}{\partial t}\begin{pmatrix}\rho\\ \rho v_x\\ \rho v_z\\ P\end{pmatrix}+\frac{\partial}{\partial x}\begin{pmatrix}\rho v_x\\ \rho v_x^2+P\\ \rho v_x v_z\\ v_x P+K v_x\end{pmatrix}+\frac{\partial}{\partial z}\begin{pmatrix}\rho v_z\\ \rho v_x v_z\\ \rho v_z^2+P\\ v_z P+K v_z\end{pmatrix}=\begin{pmatrix}0\\ \rho f_x\\ \rho f_z\\ P\left(\frac{\partial v_x}{\partial x}+\frac{\partial v_z}{\partial z}\right)\end{pmatrix}, \tag{5.101}$$

where K is the bulk modulus of the fluid and P is the pressure within the fluid. The equations can be abbreviated as

$$\frac{\partial \mathbf{U}}{\partial t}+\frac{\partial \mathcal{F}(\mathbf{U})}{\partial x}+\frac{\partial \mathcal{G}(\mathbf{U})}{\partial z}=\mathcal{S}(\mathbf{U}), \tag{5.102}$$

where $\mathbf{U}$ is the vector of conserved variables. The final equation for pressure, P, in Eq. (5.101) is not required as the pressure value can be determined from the density using the equation of state, but it is included here to depict how the linearized equations are formulated. It may be possible to use this equation for a conservation of mass check after computational advection steps, but this is not implemented in this work.

The equations in (5.101) are recast into a moving domain by applying the material derivative in time, Eq. (5.87), to yield

$$\frac{\partial}{\partial t}\begin{pmatrix}\rho\\ \rho v_x\\ \rho v_z\\ P\end{pmatrix}+\frac{\partial}{\partial x}\begin{pmatrix}\rho v_x - c_{\text{win}}\rho\\ \rho v_x^2 + P - c_{\text{win}}\rho v_x\\ \rho v_x v_z - c_{\text{win}}\rho v_z\\ v_x P + K v_x - c_{\text{win}} P\end{pmatrix}+\frac{\partial}{\partial z}\begin{pmatrix}\rho v_z\\ \rho v_x v_z\\ \rho v_z^2 + P\\ v_z P + K v_z\end{pmatrix}=\begin{pmatrix}0\\ \rho f_x\\ \rho f_z\\ P\left(\frac{\partial v_x}{\partial x}+\frac{\partial v_z}{\partial z}\right)\end{pmatrix}, \quad (5.103)$$

where c_{win} is the velocity of the domain. The quasi-conservation equations are solved numerically using the same high-order Godunov scheme described earlier which requires a set of linearized equations as well as the eigenvalue decomposition of the linearized matrices. The set of linearized equations is given by

$$\frac{\partial}{\partial t}\begin{pmatrix}\rho\\ v_x\\ v_z\\ P\end{pmatrix}+\mathcal{A}_{xp}\frac{\partial}{\partial x}\begin{pmatrix}\rho\\ v_x\\ v_z\\ P\end{pmatrix}+\mathcal{A}_{z}\frac{\partial}{\partial z}\begin{pmatrix}\rho\\ v_x\\ v_z\\ P\end{pmatrix}=\begin{pmatrix}0\\ f_x\\ f_z\\ 0\end{pmatrix}, \quad (5.104)$$

where

$$\mathcal{A}_{xp}=\begin{bmatrix}v_x - c_{\text{win}} & \rho & 0 & 0\\ 0 & v_x - c_{\text{win}} & 0 & -1/\rho\\ 0 & 0 & v_x - c_{\text{win}} & 0\\ 0 & K & 0 & v_x - c_{\text{win}}\end{bmatrix} \quad (5.105)$$

and

$$\mathcal{A}_{z}=\begin{bmatrix}v_z & 0 & \rho & 0\\ 0 & v_z & 0 & 0\\ 0 & 0 & v_z & -1/\rho\\ 0 & 0 & K & v_z\end{bmatrix}. \quad (5.106)$$

The eigenvalue decomposition of $\mathcal{A}_{xp}$ is given by $\mathcal{A}_{xp} = \mathcal{X}_x \Lambda^F_{xp} \mathcal{X}_x^{-1}$, where

$$\mathcal{X}_x = \begin{bmatrix} 1 & 0 & N_x\rho & N_x\rho \\ 0 & 0 & -N_x c & N_x c \\ 0 & 1 & 0 & 0 \\ 0 & 0 & N_x K & N_x K \end{bmatrix}, \tag{5.107}$$

$$\Lambda^{\mathsf{F}}_{xp} = \begin{bmatrix} v_x - c_{\text{win}} & 0 & 0 & 0 \\ 0 & v_x - c_{\text{win}} & 0 & 0 \\ 0 & 0 & v_x - c_{\text{win}} - c & 0 \\ 0 & 0 & 0 & v_x - c_{\text{win}} + c \end{bmatrix}, \tag{5.108}$$

and

$$\mathcal{X}_x^{-1} = \begin{bmatrix} 1 & 0 & 0 & \rho/K \\ 0 & 0 & 1 & 0 \\ 0 & -1/(2N_x c) & 0 & 1/(2N_x K) \\ 0 & 1/(2N_x c) & 0 & 1/(2N_x K) \end{bmatrix}. \tag{5.109}$$

In the equations above, c is the sound speed of the fluid given by $c = \sqrt{K/\rho}$ and N_x is an arbitrary constant taken to be one in this work. Likewise, in the z direction the decomposition is given by $\mathcal{A}_z = \mathcal{X}_z \Lambda^F_z \mathcal{X}_z^{-1}$, where

$$\mathcal{X}_z = \begin{bmatrix} 1 & 0 & N_z\rho & N_z\rho \\ 0 & 1 & 0 & 0 \\ 0 & 0 & -N_z c & N_z c \\ 0 & 0 & N_z K & N_z K \end{bmatrix}, \tag{5.110}$$

$$\Lambda_z^{\mathsf{F}} = \begin{bmatrix} v_z & 0 & 0 & 0 \\ 0 & v_z & 0 & 0 \\ 0 & 0 & v_z - c & 0 \\ 0 & 0 & 0 & v_z + c \end{bmatrix}, \tag{5.111}$$

and

$$\mathcal{X}_z^{-1} = \begin{bmatrix} 1 & 0 & 0 & \rho/K \\ 0 & 1 & 0 & 0 \\ 0 & 0 & -1/(2N_z c) & 1/(2N_z K) \\ 0 & 0 & 1/(2N_z c) & 1/(2N_z K) \end{bmatrix}, \tag{5.112}$$

where N_z is also an arbitrary constant taken to be one.

For the corrector scheme used in the numerical method, the nonlinear adjustment fluxes are computed in much the same way as for the elastic case and are given by

$$\mathcal{F}^c = \begin{pmatrix} 0 \\ \rho v_x(v_x - c_{\text{win}}) + P - P/\rho \\ \rho v_z(v_x - c_{\text{win}}) \\ 0 \end{pmatrix} \quad \text{and} \quad \mathcal{G}^c = \begin{pmatrix} 0 \\ \rho v_x v_z \\ \rho v_z^2 + P - P/\rho \\ 0 \end{pmatrix}. \tag{5.113}$$

For the solid portion of the domain, the equations used to describe wave motion remain the same and are given in the previous sections. At the interface between fluid and solid portions, interface conditions must be imposed. The conditions are given by

$$\begin{aligned} \sigma_{nn}^{\mathsf{S}} &= -P^{\mathsf{F}} \\ v_n^{\mathsf{S}} &= v_n^{\mathsf{F}} \\ \sigma_{xz}^{\mathsf{S}} &= 0 \end{aligned} \tag{5.114}$$

where n represents the direction normal to the interface (x or z in this implementation). These conditions represent the conservation of normal stress and particle velocity at a slip interface.

5.5.1 Numerical Implementation

The governing equations are evaluated numerically on a rectangular computational grid which is discretized into cells. Each cell is specified as a fluid or solid cell. In the solid cells, the equations being approximately solved are

$$\frac{\partial \mathbf{U}^{\mathsf{S}}}{\partial t} + \frac{\partial F\left(\mathbf{U}^{\mathsf{S}}\right)}{\partial x} + \frac{\partial G\left(\mathbf{U}^{\mathsf{S}}\right)}{\partial z} = S\left(\mathbf{U}^{\mathsf{S}}\right), \tag{5.115}$$

where the conserved variables are $\mathbf{U}^{\mathsf{S}} = [\rho\ \rho v_x\ \rho v_z\ \sigma_{xx}\ \sigma_{zz}\ \sigma_{xz}]^T$. In the fluid cells, the governing equations being evaluated are

$$\frac{\partial \mathbf{U}^{\mathsf{F}}}{\partial t} + \frac{\partial \mathcal{F}\left(\mathbf{U}^{\mathsf{F}}\right)}{\partial x} + \frac{\partial \mathcal{G}\left(\mathbf{U}^{\mathsf{F}}\right)}{\partial z} = \mathcal{S}\left(\mathbf{U}^{\mathsf{F}}\right), \tag{5.116}$$

where the conserved variables are $\mathbf{U}^{\mathsf{F}} = [\rho\ \rho v_x\ \rho v_z\ P]^T$. Throughout this section the calligraphic letters will be associated with the fluid equations and a standard font is associated with the solid equations.

The numerical procedure for evaluating the equations follows the same high order Godunov scheme presented earlier. All aspects of the numerical procedure are the same except for in the direct vicinity of the fluid-solid interface. At the interface, care must be taken when computing the slopes and cross-cell fluxes. The differences are outlined in the paragraphs below.

Interface Slopes At the interface, only the normal stress and normal velocity are continuous and the other primitive variables can be discontinuous. Slopes for the discontinuous variables need to be computed using the correct cell values of like materials. As an example, the slopes for contacting fluid and solid cells are given below, where the fluid cell lies directly to the left of the solid cell. The initial van Leer slope at the fluid cell (i, j) is computed with

$$\left(\frac{\partial \hat{\mathbf{q}}^{\mathsf{F}}}{\partial x}\right)_{ij}^{vL} = \frac{2(\hat{\mathbf{q}}^{\mathsf{F}}_{i,j} - \hat{\mathbf{q}}^{\mathsf{F}}_{i-1,j})}{\Delta x} \tag{5.117}$$

, where $\hat{\mathbf{q}}^{\mathsf{F}} = [\rho\ v_z]^{\mathsf{T}}$ is the vector of discontinuous primitive fluid variables.The van Leer slope at the solid cell $(i+1, j)$ is computed with

$$\left(\frac{\partial \hat{\mathbf{q}}^{\mathsf{S}}}{\partial x}\right)^{vL}_{i+1,j} = \frac{2(\hat{\mathbf{q}}^{\mathsf{S}}_{i+2,j} - \hat{\mathbf{q}}^{\mathsf{S}}_{i+1,j})}{\Delta x}, \tag{5.118}$$

where $\hat{\mathbf{q}}^{\mathsf{S}} = [\rho\ v_z\ \sigma_{zz}\ \sigma_{xz}]^{\mathsf{T}}$ is the vector of discontinuous primitive solid variables. The van Leer slopes are then used to construct the third-order slopes are given by

$$\left(\frac{\partial \hat{\mathbf{q}}^{\mathsf{F}}}{\partial x}\right)^{\text{3rd}}_{ij} = \frac{\left(\left[\hat{\mathbf{q}}^{\mathsf{F}}_{i,j} + \frac{1}{4}\Delta x \left(\frac{\partial \hat{\mathbf{q}}^{\mathsf{F}}}{\partial x}\right)^{vL}_{i,j}\right] - \left[\hat{\mathbf{q}}^{\mathsf{F}}_{i-1,j} + \frac{1}{4}\Delta x \left(\frac{\partial \hat{\mathbf{q}}^{\mathsf{F}}}{\partial x}\right)^{vL}_{i-1,j}\right]\right)}{\Delta x} \tag{5.119}$$

and

$$\left(\frac{\partial \hat{\mathbf{q}}^{\mathsf{S}}}{\partial x}\right)^{\text{3rd}}_{i+1,j} = \frac{\left(\left[\hat{\mathbf{q}}^{\mathsf{S}}_{i+2,j} - \frac{1}{4}\Delta x \left(\frac{\partial \hat{\mathbf{q}}^{\mathsf{S}}}{\partial x}\right)^{vL}_{i+2,j}\right] - \left[\hat{\mathbf{q}}^{\mathsf{S}}_{i+1,j} - \frac{1}{4}\Delta x \left(\frac{\partial \hat{\mathbf{q}}^{\mathsf{S}}}{\partial x}\right)^{vL}_{i+1,j}\right]\right)}{\Delta x}. \tag{5.120}$$

The slopes are then limited in order to prevent oscillations from strong shocks by Eq. (5.35). Slopes computed in this fashion lose an order of accuracy (3rd order versus 4th order accuracy), but still provide ample accuracy for the waveforms studied in this work.

Interface Riemann Problem Another aspect that requires special attention at the interface is the flux calculations. The interface between solid and fluid cells is evaluated using an approximate Riemann solution that decomposes the jump between the dissimilar equations using invariants defined by Eq. (5.114). There are two possible orientations that can arise in the interface problem: the fluid to the left of the solid and the solid to the left of the fluid. Each case requires a different jump decomposition.

For the case when the fluid cell is to the left (or above) the solid cell, the primitive variables at the interface are determined using the shock waves in the solid and the rarefaction wave in the fluid. Figure 5.11 shows the schematic representation of this situation. The

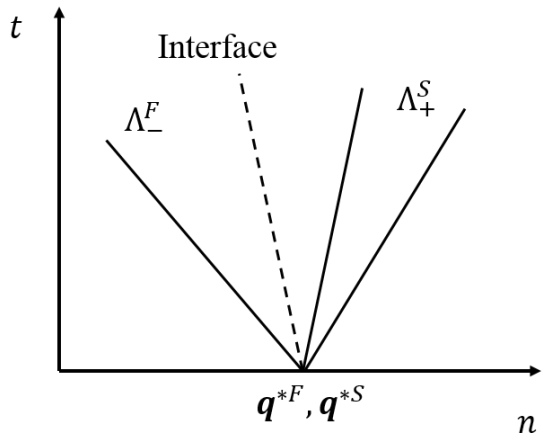

Figure 5.11: $n-t$ plot (n indicating the direction normal to the interface) for a fluid-solid Riemann problem where the fluid is to the left of the solid.

interfacial values of the primitive variables in the solid are approximated by

$$\mathbf{q}^{*\mathsf{S}} = \mathbf{q}_R - \phi_1 \mathbf{x}_{R,5} - \phi_2 \mathbf{x}_{R,6} \tag{5.121}$$

where $\mathbf{x}_{R,5}$ and $\mathbf{x}_{R,6}$ are the eigenvectors associated with the shock waves in the right, solid cell. The primitive variables of the fluid, at the interface, are approximated as

$$\mathbf{q}^{*\mathsf{F}} = \mathbf{q}_L + \phi_3 \boldsymbol{x}_{L,3} \tag{5.122}$$

where $\boldsymbol{x}_{L,3}$ is the eigenvector associated with the rarefaction wave in the left, fluid cell. The ϕ values represent unknowns in the interface problem, and are solved for using the interface conditions, Eq. (5.114), which can be rewritten as invariants of the Riemann problem:

$$\begin{aligned} \sigma_{nn}^{*\mathsf{S}} &= -P^{*\mathsf{F}} = \sigma_{nn}^* \\ v_n^{*\mathsf{S}} &= v_n^{*\mathsf{F}} = v_n^* \\ \sigma_{xz}^{*\mathsf{S}} &= 0 \end{aligned} \tag{5.123}$$

Applying (5.123) to (5.121) leads to

$$\begin{pmatrix} \sigma^*_{nn} \\ 0 \end{pmatrix} = \begin{pmatrix} \sigma_{nnR} \\ \sigma_{xzR} \end{pmatrix} - \phi_1 \begin{pmatrix} (X_R)_{j,5} \\ (X_R)_{6,5} \end{pmatrix} - \phi_2 \begin{pmatrix} (X_R)_{j,6} \\ (X_R)_{6,6} \end{pmatrix}, \tag{5.124}$$

where the index j is 4 or 5 if the flux direction is the x or z direction, respectively. Inverting the square matrix leads to expressions for the unknowns, ϕ_1 and ϕ_2,

$$\begin{pmatrix} \phi_1 \\ \phi_2 \end{pmatrix} = \begin{bmatrix} (X_R)^{-1}_{j,5} & 0 \\ 0 & (X_R)^{-1}_{6,6} \end{bmatrix} \begin{pmatrix} \sigma_{nnR} - \sigma^*_{nn} \\ \sigma_{xzR} \end{pmatrix}. \tag{5.125}$$

Solving (5.121) for the normal interface velocity, in the solid, leads to

$$v^*_n = v_{nR} - \phi_1 (X_R)_{i,5} - \phi_2 (X_R)_{i,6} \tag{5.126}$$

where the index i corresponds to 2 or 3 depending on whether the normal direction $n = x$ or z, respectively. Using the expression for ϕ_1 in (5.125) leads to an equation for the normal velocity in terms of the normal stress:

$$v^*_n = v_{nR} - (X_R)^{-1}_{j,5} (\sigma_{nnR} - \sigma^*_{nn})(X_R)_{i,5} - \phi_2 (X_R)_{i,6}. \tag{5.127}$$

The unknown ϕ_3 is determined by by solving for the interfacial normal stress in the fluid,

$$P^{*\mathsf{F}} = -\sigma^*_{nn} = P_L + \phi_3 (X_L)_{4,3} \quad \Rightarrow \quad \phi_3 = -(X_L)^{-1}_{4,3} (\sigma^*_{nn} + P_L). \tag{5.128}$$

This expression is used to write an equation for the interfacial normal velocity in the fluid in terms of the normal stress,

$$v^*_n = v_{nL} - (X_L)^{-1}_{4,3} (\sigma^*_{nn} + P_L)(X_L)_{i,3}. \tag{5.129}$$

According to the interface conditions, the normal velocity at the interface must be equal in the fluid and the solid. Therefore, Eqs. (5.126) and (5.129) are set equal to each other to solve for the unknown interfacial normal stress, σ^*_{nn}. Upon simplifying, the normal stress is written as

$$\sigma^*_{nn} = \frac{v_{nL} - v_{nR} + (X_R)^{-1}_{j,5}(X_R)_{i,5}\sigma_{nnR} - (X_L)^{-1}_{4,3}(X_L)_{i,3}P_L + \phi_2(X_R)_{i,6}}{(X_L)^{-1}_{4,3}(X_L)_{i,3} + (X_R)^{-1}_{j,5}(X_R)_{i,5}}. \tag{5.130}$$

The steps for determining the solution to the interface Riemann problem are then to first solve $\phi_2 = (X_R)^{-1}_{6,6}\sigma_{xzR}$, use ϕ_2 to solve for σ^*_{nn} via Eq. (5.130), and then solve for ϕ_1 using (5.125) and ϕ_3 using (5.128). Once the unknown ϕ values are computed, the primitive variables at the interface can be calculated using Eq. (5.121) for the solid variables and Eq. (5.122) for the fluid variables.

For the case when the fluid cell is to the right (or below) the solid cell, the primitive variables at the interface are determined using the rarefaction waves in the solid and the shock waves in the solid. Figure 5.12 gives the schematic representation of this situation. The interfacial values of the primitive variables in the solid and fluid are now approximated

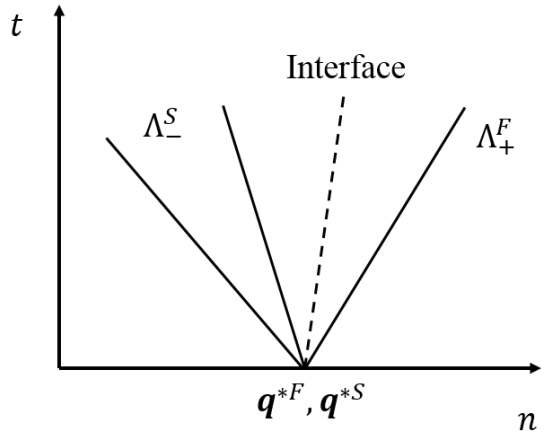

Figure 5.12: $n - t$ plot (n indicating the direction normal to the interface) for a fluid-solid Riemann problem where the fluid is to the right of the solid.

by

$$\mathbf{q}^{*\mathsf{S}} = \mathbf{q}_L + \phi_1 \mathbf{x}_{L,3} + \phi_2 \mathbf{x}_{L,4} \tag{5.131}$$

and

$$\mathbf{q}^{*\mathsf{F}} = \mathbf{q}_R - \phi_3 \boldsymbol{x}_{R,4}. \tag{5.132}$$

Following the same process as was done for the reverse case, the unknown ϕ values and the interfacial normal stress are given by

$$\begin{aligned} \phi_1 &= (X_L)^{-1}_{j,3}(\sigma^*_{nn} - \sigma_{nnL}) \\ \phi_2 &= -(X_L)^{-1}_{6,4}\sigma_{xzL} \\ \phi_3 &= (X_R)^{-1}_{4,4}(\sigma^*_{nn} + P_R) \end{aligned} \tag{5.133}$$

and

$$\sigma^*_{nn} = \frac{v_{nR} - v_{nL} - (X_R)^{-1}_{4,4}(X_R)_{i,4}P_R + (X_L)^{-1}_{j,3}(X_L)_{i,3}\sigma_{nnL} - \phi_2(X_L)_{i,4}}{(X_L)^{-1}_{j,3}(X_L)_{i,3} + (X_R)^{-1}_{4,4}(X_R)_{i,4}}. \tag{5.134}$$

Once the system of equations is solved, the primitive variables at the interface are calculated using (5.131) and (5.132).

The interface variables, $\mathbf{q}^{*\mathsf{S}}$ and $\mathbf{q}^{*\mathsf{F}}$, are used to generate the fluxes for both the fluid and solid calculations. The interface fluxes are computed assuming the boundary between the fluid and solid cells exactly tracks the fluid-solid interface. In the x direction, the interfacial fluxes at the $(i+1/2, j)$ edge are given by

$$F_{i+1/2,j} = \begin{pmatrix} -c_{\text{win}}\rho^{*\mathsf{S}}_{i+1/2,j} \\ -\sigma^*_{xx,i+1/2,j} - c_{\text{win}}\rho^{*\mathsf{S}}_{i+1/2,j}v^*_{x,i+1/2,j} \\ -c_{\text{win}}\rho^{*\mathsf{S}}_{i+1/2,j}v^{*\mathsf{S}}_{z,i+1/2,j} \\ v^*_{x,i+1/2,j}\sigma^{\mathsf{S}}_{xx} - (\lambda^{\mathsf{S}} + 2\mu^{\mathsf{S}})v^*_{x,i+1/2,j} - c_{\text{win}}\sigma^*_{xx,i+1/2,j} \\ v^*_{x,i+1/2,j}\sigma^{\mathsf{S}}_{zz} - \lambda^{\mathsf{S}}v^*_{x,i+1/2,j} - c_{\text{win}}\sigma^{*\mathsf{S}}_{zz,i+1/2,j} \\ v^*_{x,i+1/2,j}\sigma^{\mathsf{S}}_{xz} - \mu^{\mathsf{S}}v^{*\mathsf{S}}_{z,i+1/2,j} \end{pmatrix} \tag{5.135}$$

and

$$\mathcal{F}_{i+1/2,j} = \begin{pmatrix} -c_{\text{win}}\rho^{*\mathsf{F}}_{i+1/2,j} \\ P^*_{i+1/2,j} - c_{\text{win}}\rho^{*\mathsf{F}}_{i+1/2,j} v^*_{x,i+1/2,j} \\ -c_{\text{win}}\rho^{*\mathsf{F}}_{i+1/2,j} v^{*\mathsf{F}}_{z,i+1/2,j} \\ v^*_{x,i+1/2,j} P^{\mathsf{F}} + K^{\mathsf{F}} v^*_{x,i+1/2,j} - c_{\text{win}} P^*_{i+1/2,j} \end{pmatrix}, \tag{5.136}$$

where the terms without a subscript denote cell-centered values for the appropriate material (at either the (i, j) or $(i+1, j)$ cell). Note that the stress/pressure fluxes include cell-centered terms; this is to correct for the source terms which should be absent at the interface. For the z direction, the fluxes at the $(i, j + 1/2)$ edge are given by

$$G_{i,j+1/2} = \begin{pmatrix} 0 \\ 0 \\ -\sigma^*_{zz,i,j+1/2} \\ v^*_{z,i,j+1/2}\sigma^{\mathsf{S}}_{xx} - \lambda^{\mathsf{S}} v^*_{z,i,j+1/2} \\ v^*_{z,i,j+1/2}\sigma^{\mathsf{S}}_{zz} - (\lambda^{\mathsf{S}} + 2\mu^{\mathsf{S}}) v^*_{z,i,j+1/2} \\ v^*_{z,i,j+1/2}\sigma^{\mathsf{S}}_{xz} - \mu^{\mathsf{S}} v^{*\mathsf{S}}_{x,i,j+1/2} \end{pmatrix} \tag{5.137}$$

and

$$\mathcal{G}_{i,j+1/2} = \begin{pmatrix} 0 \\ 0 \\ P^*_{i,j+1/2} \\ v^*_{z,i,j+1/2} P^{\mathsf{F}} + K^{\mathsf{F}} v^*_{z,i,j+1/2} \end{pmatrix}, \tag{5.138}$$

where the terms without a subscript again denote a cell-center value at either (i, j) or $(i, j + 1)$, whichever is the correct material type. Fluxes are applied throughout the numerical procedure in the same manner as described in previous sections.

5.5.2 Model Verification

The progressive elastic-fluid model is benchmarked against experimental results to validate the implementation and to illustrate the effects of elasticity on long-range pulse propagation. The experiment considered is a tank test in which wave propagation over flat and sloped configurations represents a scaled model of a typical ocean environment. Results of the experiment have previously been shown to agree well with the elastic parabolic equation solution, but disagree with the fluid parabolic equation solution (Collis *et al.*, 2007a).

Tank Experiment A series of laboratory experiments with scale models of an elastic ocean bottom were performed at the Naval Research Laboratory. The particular experiment used in this comparison is the first Elastic Parabolic Equation Experiment (EPE-1) which was carried out in April 2004 inside a large fresh water tank at NRL (Soukup *et al.*, 2004). An elastic bottom was modeled using a PVC slab (122 $\times$ 122 $\times$ 10 cm) from San Diego plastics. The slab was suspended in water by cables which were attached to its corners to minimize reflections. Source and receiver hydrophones were positioned over the slab using a robotic apparatus that allowed for accurate positioning. The source, closer to the edge of the slab, is fixed while the receiver moved at prescribed increments away from the source. The experimental configuration is presented in Figure 5.13.

During EPE-1 the water temperature was maintained so that the sound speed remained within $\pm$ 1 m/s of 1482 m/s. As discussed in the experimental report, (Soukup *et al.*, 2004), estimates for the elastic properties of the PVC slab in the band 300 kHz - 1.5 MHz were obtained by transmitting pulses through a sample of the material. Results at 300 kHz are summarized in Table 5.1, with estimated relative errors given in the second column. Physical values at this frequency were used because it represented the upper limit of the frequency band of the source pulse.

The transmitted waveform was an impulse with a flat frequency spectrum over the band 100-300 kHz. A reference measurement was made by positioning the source and receiver

Figure 5.13: The experimental configuration: the PVC slab is suspended in water by cables attached to its corners. The source hydrophone remains in a fixed position while a robotic arm controls the position of the receiver hydrophone.

1 m apart and measuring the pressure produced from the source pulse. Figure 5.14 shows the temporal and frequency responses for the reference measurement. Measurements were recorded at 8192 points with a 0.5 μs sampling interval. Windowing was applied to eliminate reflections from the hardware and the walls of the tank thus ensuring a 2D axisymmetric model was sufficient for describing the physics.

Experimental runs were conducted in two environments with different source and receiver configurations. To show the analogy between propagation in the tank and an ocean waveguide, the acoustic propagation calculations are presented at a scale of 1000:1 in Figure 5.15, where the lengths have been appropriately modified. The first environment is essentially range independent (nearly horizontal slab), where the geometry is shown in Figure 5.15(a). Also shown are the geometrical parameters: source depth z_s which is near the middle of the water column, depth of the slab below the source z_0, depth of the opposite edge of the slab z_1, and depth of the receiver array z_r. Values for these geometrical parameters are

Table 5.1: Estimated physical values, with associated error estimates, of elastic PVC properties at 300 kHz (see (Soukup *et al.*, 2004)).

Parameter	Value	Relative Error (±%)	Absolute Error
Density (kg/m^3)	1378	0.5	7
Compressional speed (m/s)	2290	0.5	10
Compressional attenuation (dB/m)	0.33	2	0.01
Shear speed (m/s)	1050	0.5	5
Shear attenuation (dB/m)	1.00	4	0.04

given in Table 5.2. Collis *et al.* determined corrected values for the geometrical parameters using inversion techniques such as iteration and simulated annealing, where the simulated annealing values produced the best agreement (Collis *et al.*, 2007a). These corrected values are also provided in Table 5.2. For the first run, the slab was suspended nearly parallel to the air-water interface. The propagation track was centered on the slab, with the source 15 cm away from the edge. The receiver was moved horizontally between 25 and 135 cm from the edge of the slab nearest the source to produce a virtual horizontal array with a spacing of 2 mm. The slab attenuated acoustic energy sufficiently to prevent spurious reflections from the slab bottom.

Table 5.2: Geometric parameters for the flat case including corrected values determined by simulated annealing. Errors are between reported and simulated annealing results.

Flat case	Reported	Simulated annealing	Relative error (± %)
z_s (m)	75.0	69.1	7.9
z_r (m)	145.5	137.1	5.8
z_0 (m)	150.0	144.7	3.6
z_1 (m)	150.0	145.4	3.1

For the second run, the environment is range dependent, with the slab sloping upwards as illustrated in Figure 5.15(b). Reported and corrected values of the geometrical parameters are given in Table 5.3. The increased error in the parameters may be due to evaporation of water from the tank during the time in between runs.

Table 5.3: Geometric parameters for the sloped case including corrected values determined by simulated annealing. Errors are between reported and simulated annealing results.

Sloped case	Reported	Simulated annealing	Relative error (± %)
z_s (m)	69.0	63.4	8.2
z_r (m)	20.0	15.6	22
z_0 (m)	138.0	132.9	3.7
z_1 (m)	49.5	45.4	8.2

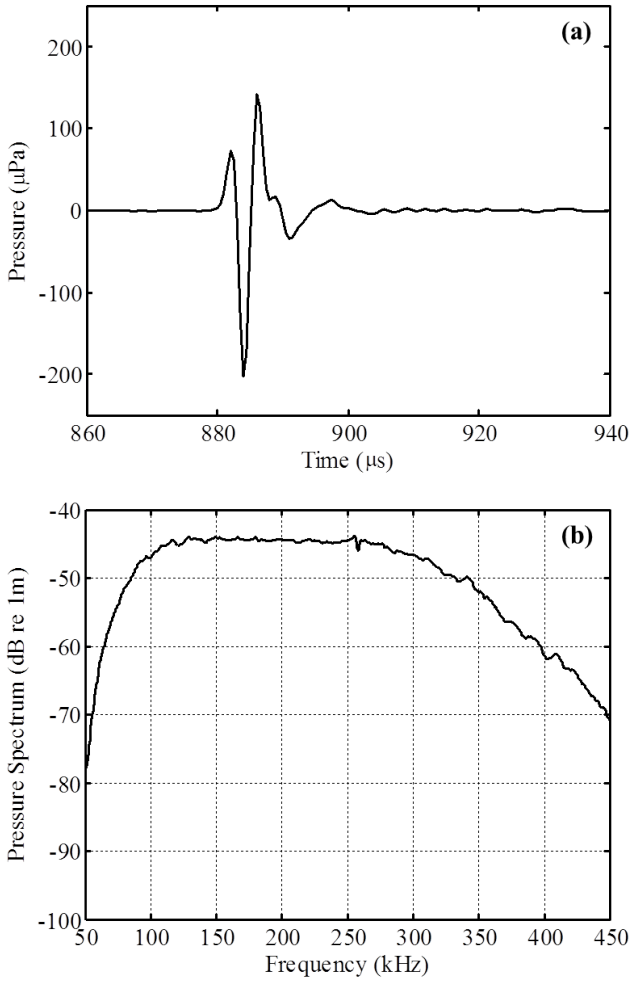

Figure 5.14: Reference measurement of the source and receiver separated by 1 m. (a) Temporal response plot of pressure (μPa) vs time (μs). (b) The frequency response plotted as power spectral density vs frequency (kHz).

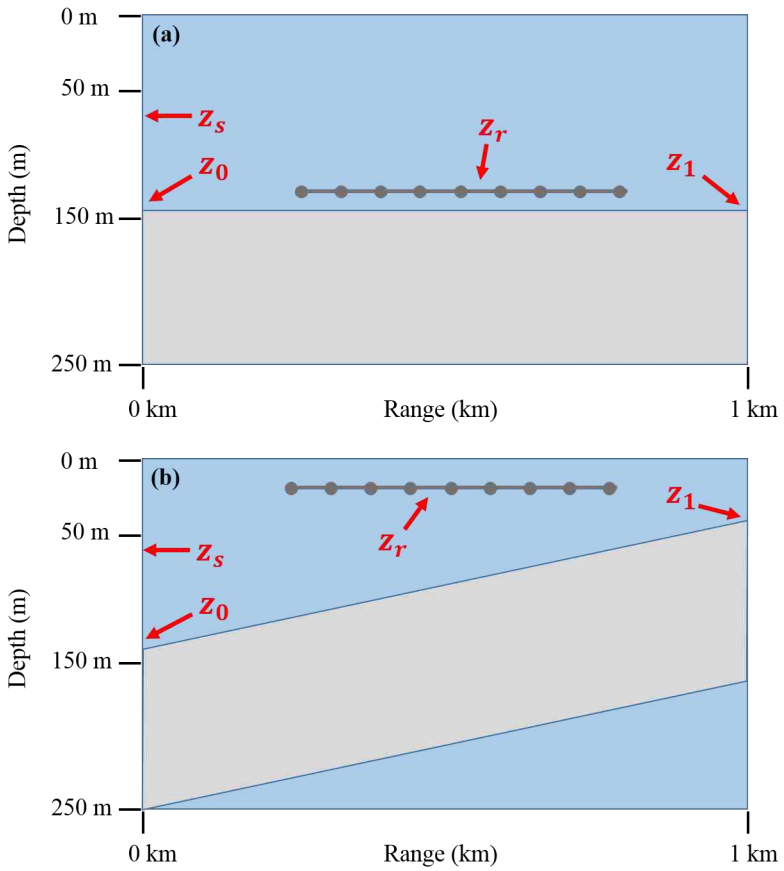

Figure 5.15: Environments studied in the tank experiment. (a) Flat case. (b) Sloped case.

Propagation Simulations Experimental data is compared with calculations from both the progressive elastic-fluid and the weakly-elastic NPE (WENPE) models described in the previous sections. The scaled environments are modeled using the corrected, simulated annealing values for the geometrical parameters, and the initial pulse is temporally adjusted to reflect the scaling. Attenuation within the bottom layer is neglected in these runs because the energy loss due to the interface scattering dominates over dissipation. Details of the simulations are provided here.

The computational domain used in all simulations has a width of 65 m and a depth of 160 m. The width is set as such in order to resolve the entire duration of the initial pulse prior to the progression stage. Roughly the first 150 m of depth is water, modeled with a

density of 1000 kg/m^3 and a bulk modulus of $K = 2.196$ GPa. The following 10 m represents the PVC slab which is only a fraction of the total slab thickness. It is assumed that the majority of the acoustic energy will be reflected from this interface and so only a few meters are required to capture relevant energy penetration. For the elastic-solid model, the final 10 m of the domain are modeled as a linearly elastic solid with a density of 1378 kg/m^3 and elastic parameters given by $\lambda = 4.188$ GPa and $\mu = 1.519$ GPa. For the WENPE model, the final 10 m are modeled as a fluid with a density of 1378 kg/m^3 and a bulk modulus of $K = 7.226$ GPa – this value leads to the correct compressional speed for the PVC. For both the models, the domain is discretized into a grid with x direction grid spacing of 0.4 m and z direction grid spacing of 0.6 m, and the time step is generated based on a CFL condition number of 0.5.

The initial condition is based on the reference pulse given in Figure 5.14(a), but with the amplitude scaled, and then shifted in time. The scaling factor and time shift value are determined by iterating the solution until the numerical result at the first receiver position agreed well with the data. The source location is set at the far left edge of the computational domain. The speed of the computational domain, c_{win}, is set to zero for the first 25 ms of the simulation. This allows the pulse to become fully developed prior to the window progressing down range. After 25 ms, the speed of the window is set to 1465 m/s. This velocity is slightly less than the sound speed of the water which allows the x direction velocity to stay above zero as the pulse slowly advances within the domain. This helps prevent errors that can develop with very small x velocities for long running simulations. The top boundary has a pressure-release condition, $P = 0$, and the right and bottom boundaries have outflow conditions. The left boundary initially has a symmetry boundary condition, but is changed to an outflow condition once the domain starts to progress down range. All outflow boundaries are complemented with 4 m thick absorbing sponge zone (artificial absorbing layer). The simulations run for approximately 800 ms to resolve the entire 1000 m of propagation.

Comparisons of Measurements and Calculations Data is recorded at two receiver positions (500 m and 1000 m), vertically located at the horizontal receiver array depth, z_r. For the flat case, the receivers are located near the bottom of the water column just above the ocean-bottom interface. Data from this area gives insight into the accuracy of the computational treatment of the interface conditions. Comparisons for the elastic, fluid, and experimental results are given in Figure 5.16 and Figure 5.17 on the following pages. For the sloped case, the receivers are located towards the top of the domain. Comparisons for the elastic, fluid, and experimental results are given in Figure 5.18 and Figure 5.19. The pressure fields throughout the entire simulation time are given in Appendix D for both test cases.

Results show that the progressive elastic-fluid solution aligns well with the experimental data for both the flat and sloped environments. The WENPE (fluid) solution appears to have fairly good agreement with the experiment for the first receiver position in the flat environment, but there are slight phase errors that develop at the second position. For the sloped case, the WENPE solution does not have good agreement. This is due to increased reflections within the narrowing waveguide, and this increase in ocean-bottom interaction leads to errors within the WENPE model, as seen in the previous chapter.

5.6 Discussion

A new long-range shock propagation model based on finite-volume techniques has been developed, implemented, and benchmarked against experimental data. The model is able to treat fully elastic media, but at the expense of additional computational resources. A high order Godunov scheme originally used in detonation physics calculations was adapted for the long-range shock propagation problem by translating the governing equations into a progressive domain, implementing fluid-solid interface conditions, and correctly implementing boundary conditions. The model has many advantages when compared to the traditional NPE model, but it also has some drawbacks; the advantages and disadvantages of this model

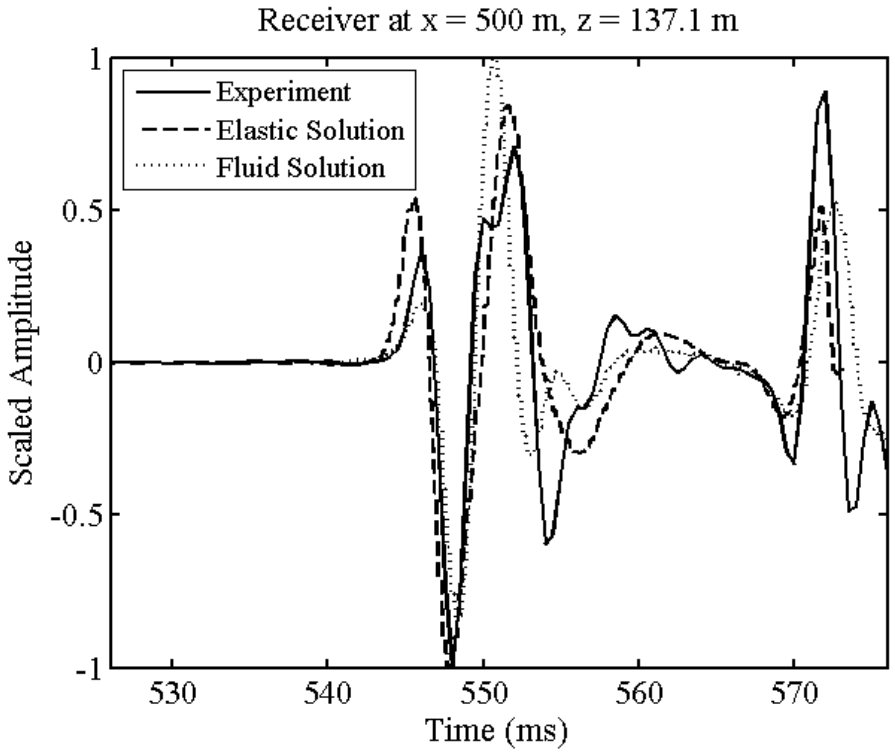

Figure 5.16: Results at the first receiver position for the flat case.

are summarized here.

The main advantage the progressive elastic-fluid model has is that it is able to treat shock in fully elastic media, the purpose for which it was developed. However, there are many other improvements when compared to the original NPE model. For one, it is capable of capturing much stronger shock than the NPE because the Godunov scheme does not introduce as much numerical dissipation as flux-corrected transport schemes. The Godunov scheme also allows for the natural treatment of discontinuous media because it not only resolves jumps in state variables but also jumps in medium properties. This means the model can handle range-dependent environments characterized by variably sloping ocean bottoms and spatially varying medium properties. Another advantage is the new model is able to accurately capture back-scattered energy and vertically-traveling wave energy because it is not biased towards the direction of propagation like the NPE is with its narrow angle assumption. The progressive nature of this model is also more versatile. The velocity of the

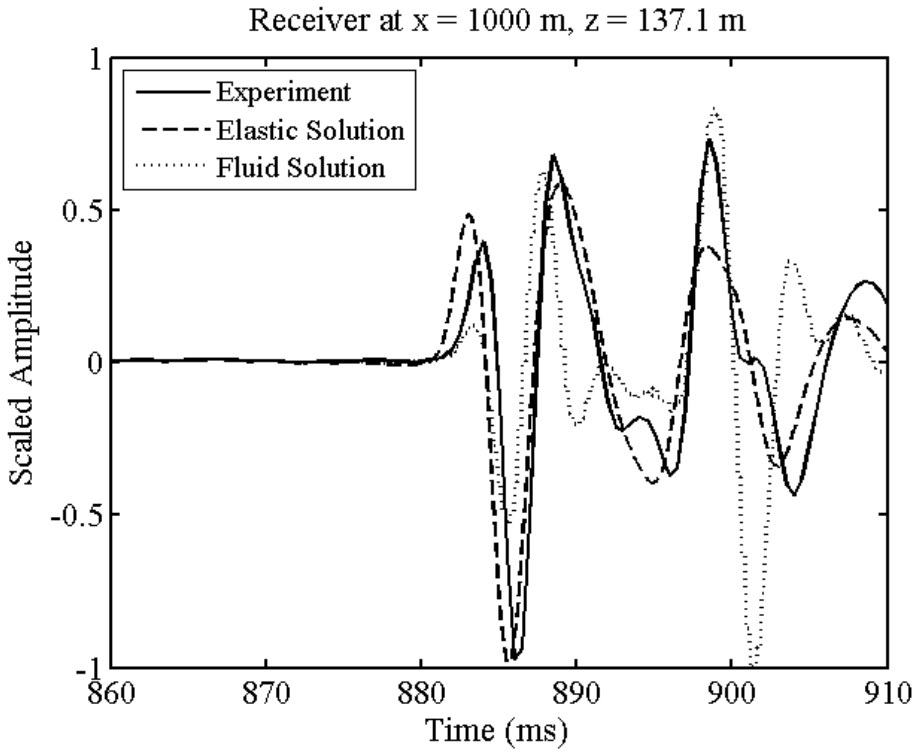

Figure 5.17: Results at the second receiver position for the flat case.

domain c_{win} can be set to arbitrary values and is not defined by the medium properties. This allows for effective treatment of initial conditions by allowing an initial pulse to develop prior to marching the domain down range. Finally, the progressive elastic-fluid model is much more adaptable than the NPE: different equations of state can be applied easily, new conservation equations can be implemented into the framework with relative ease, and information about all state variables is readily available (no post processing is required to back out information).

The progressive elastic-fluid model has some drawbacks as well. The main disadvantage is that the new model lacks the efficiency that the NPE possesses. A total of six variable fields must be solved for simultaneously at every step as compared to a single variable field with the NPE. The moving window formulation allows for vastly increased efficiency but still not near that of NPE-based models. The numerical schemes used are also much more difficult to implement due to that advanced nature of the methods employed. This makes it more difficult to update the model or to find errors in the code. Another disadvantage is that

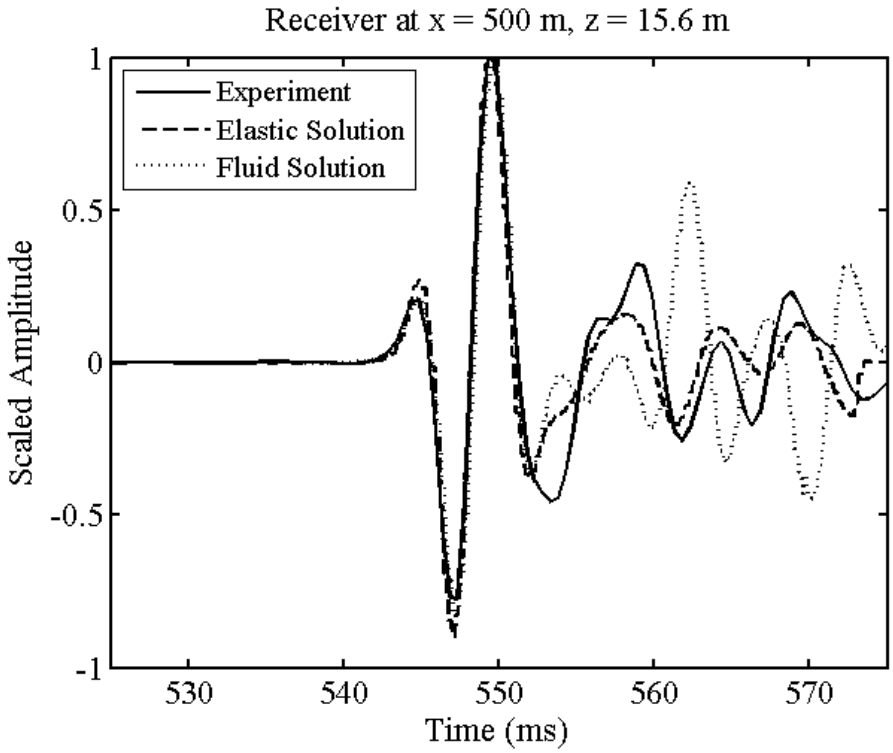

Figure 5.18: Results at the first receiver position for the sloped case.

outflowing boundaries must be handled with extreme care in long-running simulations. The outflowing boundaries tend to leak in energy which will eventually deteriorate the solution. This means the correct type of absorbing sponge zone must be applied which is not always obvious. In addition to errors developing at the boundaries, errors can also develop at strong wave fronts where the particle velocity is nearly equal to that of the moving window. This is caused by machine precision errors in the flux calculations. The remedy is to set the moving window velocity slightly lower or higher than the sound speed of the medium, depending on the problem. This means the user must be more adept in setting up the simulation. Finally, the new model is more prone to numerical error growth. If a numerical error develops it can grow and make the solution unstable since there is no built in artificial dissipation mechanism besides the flux limiting which only prevents shock ringing.

Despite these drawbacks, the new progressive elastic-fluid model is still quite useful for long-range shock problems. The model is not only able to describe shock propagation in

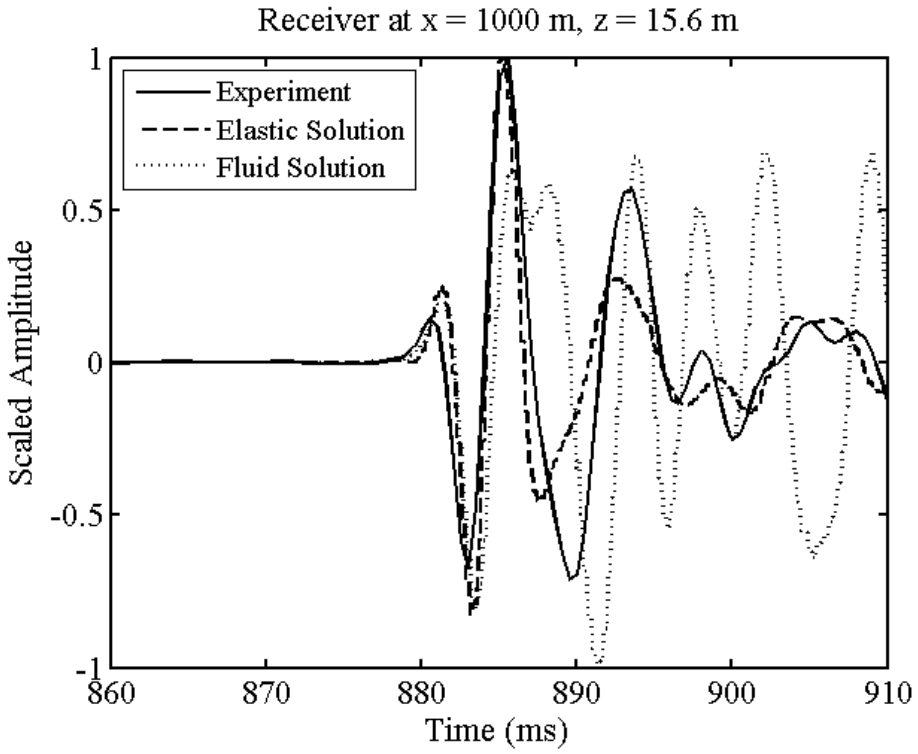

Figure 5.19: Results at the second receiver position for the sloped case.

ocean environments, but geological environments as well. This makes it useful for modeling situations the NPE was never intended for. These include modeling pulse propagation in the ocean when the source originates on land, modeling ground shock in the absence of any water whatsoever, and modeling coupled geological-ocean events such as earthquakes.

CHAPTER 6

CONCLUSIONS AND FUTURE WORK

Various numerical models have been developed to treat long-range shock propagation problems in ocean waveguides. The models are able to describe shock propagation in realistic ocean environments that include dispersive sediments and fully elastic basement layers. These models have been benchmarked and shown to accurately describe the physics of propagation.

6.1 Conclusions

The first model developed in this work was the fractional nonlinear linear progressive wave equation that allowed for frequency-dependent attenuation in the ocean bottom. NPE-based models exist that include an attenuation term, but none have allowed the attenuation to be described by a frequency power law, the behavior of which is prevalent in ocean sediments. This was accomplished here through the use of a fractional operator. This new model allows for accurate treatment of dispersive sediments but at the cost of a decrease in efficiency.

The next model devised was the weakly-elastic NPE which was developed by adapting the original NPE derivation to allow for a small amount of shear stress in the medium. The resulting equation was a modified form of the NPE that correctly transcribed elastic parameters into fluid parameters. This gives a mathematical justification for approximating low shear speed sediments as fluids for NPE-based models. Comparisons with the progressive elastic-fluid model verified this analysis for a typical ocean environment and gave an estimation of the elastic properties for which the fluid approximation is valid.

The final set of models were developed using finite-volume methods to solve coupled sets of nonlinear equations. The resulting models are much more robust and accurate than the NPE model, but are much less efficient. The final model, the progressive elastic-fluid model, is able to describe shock propagation in range-dependent, discontinuous environments that

include fully elastic layers. The velocity of the domain can be set to any value which allows for greater versatility. The model also includes a forcing term which can be used to generate sources as a function of time anywhere in the medium. This is as opposed to the NPE model which can only propagate an initial pressure disturbance which makes it difficult to analyze problems where a source is located next to an interface or boundary.

The models developed in this work offer a significant contribution to both ocean acoustic and shock propagation research. In addition to shock propagation in ocean waveguides, these models can be applied to ground shock problems, medical ultrasound research, sonic boom modeling in the atmosphere, earthquake simulations, and many other interesting and practical problems.

6.2 Future Work

There are a number of enhancements and validations of interest that could be applied to the models in this work. Certain models require addition benchmarking to comprehensively validate all aspects of their formulation, and enhancements can be made to nearly all the models to allow for greater efficiency and accuracy. The following paragraphs outline the future work that can further advance this research.

The fractional NPE was shown to agree well with the parabolic equation solution for the linear case, but more work is needed to verify that the model accurately captures attenuation for the nonlinear case as well. This would most likely need to be done by comparing the fractional model to experimental data. Also, blast waves tend to be broadband in frequency but the frequency power law in an attenuating sediment tends to change for different frequency regimes, so it may be necessary to generalize the fractional NPE even further to allow γ to vary with frequency. This may lead to multiple fractional operations which may be difficult to implement numerically.

The weakly-elastic NPE was compared against the progressive elastic-fluid model for a single typical ocean waveguide. However, it is necessary to study more environments such as

multiple layers and sloping ocean bottoms to make a better judgment towards the validity of the fluid approximation. If enough environments are analyzed it may be possible to make an empirical rule that defines the fluid approximation validation based on environment configuration and Poisson ratio.

The progressive elastic-fluid model was benchmarked against experimental data for the linear case, but it is necessary to benchmark the nonlinear capabilities as well. This can be done for strong shocks near the source by comparing to a hydrocode result, but the hydrocode solution will deteriorate at longer ranges when the shock becomes weak. At longer distances the model can be compared against the NPE solution for a fluid medium, but this does not validate the elastic case. The long-range elastic shock would need to be compared to experiment, but no high quality experimental data of this sort exists to the author's knowledge. In addition to benchmarking, there are some enhancements that can be made to the progressive elastic-fluid model. The most important enhancement would be to implement a frequency-dependent attenuation mechanism for both the compressional and shear wave fields. This would allow for correct energy dissipation in the the elastic portion of the waveguide. Another enhancement that would be useful is to implement adaptive mesh refinement (AMR) in the model to increase the efficiency. Finally, the nature of the model would make parallelism easy to implement which may greatly increase efficiency.

Overall, it would be beneficial to couple the NPE to the progressive elastic model to allow for greatly increased efficiency while still allowing for elasticity treatment. In general, only a small thickness of the elastic bottom is required to model pulse propagation in ocean waveguides that include elastic basements. This is because wave energy does not easily penetrate the dense solid, and the energy that does penetrate is usually dissipated quickly. That means the very efficient NPE can be applied in the water column, which constitutes the majority of the domain, and then it can be coupled, via interface conditions, to the progressive elastic model in the elastic bottom layer. Within the elastic bottom layer it may be possible to apply AMR to increase efficiency further.

REFERENCES CITED

Ambrosiano, J. J., Plante, D. R., McDonald, B. E., & Kuperman, W. A. 1990. Nonlinear propagation in an ocean acoustic waveguide. *J. Acoust. Soc. Am.*, **87**, 1473–1481.

Anderson, R. S., & Blackman, A. 1971. Attenuation of low-frequency sound waves in sediments. *J. Acoust. Soc. Am.*, **49**, 786–791.

Arora, M., & Roe, P. L. 1997. On postshock oscillations due to shock capturing schemes in unsteady flows. *J. Comp. Phys.*, **130**, 25–40.

Blackstock, D. T. 1967. Transient solution for sound radiated into a viscous fluid. *J. Acoust. Soc. Am.*, **41**, 1312–1319.

Bodony, D. J. 2006. Analysis of sponge zones for computational fluid mechanics. *J. Comp. Phys.*, **212**, 681–702.

Bowles, F. A. 1997. Observations on attenuation and shear-wave velocity in fine-grained, marine sediments. *J. Acoust. Soc. Am.*, **101**, 3385–3397.

Buchan, S., Dewes, F. C. D., McCann, D. M., & Smith, D. T. 1967. Measurements of the Acoustic and Geotechnical Properties of Marine Sediment Cores. *In:* Richards, A. F. (ed), *Marine Geotechnique*. University of Illinois, Institute for Oceanography.

Caine, P., & West, M. 1995. A tutorial on the non-linear progressive wave equation (NPE). Part 2. Derivation of the three-dimensional cartesian version without use of perturbation expansions. *Applied Acoustics*, **45**, 155–165.

Castor, K., McDonald, B. E., & Kuperman, W. A. 2002. Equations of nonlinear acoustics and weak shock propagation. *In: 16th International Symposium on Nonlinear Acoustics.*

Castor, K., Gerstoft, P., Roux, P., Kuperman, W. A., & McDonald, B. E. 2004. Long-range propagation of finite-amplitude acoustic waves in an ocean waveguide. *J. Acoust. Soc. Am.*, **116**, 2004–2010.

Chen, W., & Holm, S. 2002. *Fractional Laplacian, Levy stable distribution, and time-space models for linear and nonlinear frequency-dependent lossy media.* Tech. rept. Simula Research Laboratory.

Chen, W., & Holm, S. 2004. Fractional Laplacian time-space models for linear and nonlinear lossy media exhibiting arbitrary frequency power-law dependency. *J. Acoust. Soc. Am.*, **115**, 1424–1430.

Collins, M. D. 1989. A higher-order parabolic equation for wave propagation in an ocean overlying an elastic bottom. *J. Acoust. Soc. Am.*, **86**, 1459–1464.

Collins, M. D. 1993a. A split-step Padé solution for the parabolic equation method. *J. Acoust. Soc. Am.*, **93**, 1736–1742.

Collins, M. D. 1993b. A two-way parabolic equation for elastic media. *J. Acoust. Soc. Am.*, **93**, 1815–1825.

Collis, J. M., Siegmann, W. L., Collins, M. D., Simpson, H. J., & Soukup, R. J. 2007a. Comparison of simulations and data from a seismo-acoustic tank experiment. *J. Acoust. Soc. Am.*, **122**, 1987–1993.

Collis, J. M., Carey, W. M., & Pierce, A. D. 2007b. A physical explanation for less than quadratic recorded attenuation values. *Pages 1–3 of: OCEANS - 2007 Europe*. IEEE.

Collis, J. M., Siegmann, W. L., Zampolli, M., & Collins, M. D. 2009. Extension of the rotated elastic parabolic equation to beach and island propagation. *IEEE Journal of Oceanic Engineering*, **34**, 617–623.

Gilbert, F. 1998. Elastic waves in a transitional solid with arbitrary small rigidity. *Geophys. J. Int.*, **133**, 230–232.

Godunov, S. K. 1959. A difference method for numerical calculation of discontinuous solutions of the equations of hydrodynamics. *Mat. Sb*, **89**, 271–306.

Gorenflo, R., & Mainardi, F. 1998. Random walk models for space-fractional diffusion processes. *Fract. Calc. Appl. Anal.*, **1**, 167–191.

Graves, R. W. 1996. Simulating seismic wave propagation in 3D elastic media using staggered-grid finite differences. *Bull. Seis. Soc. Am.*, **86**, 1091–1106.

Hamilton, E. L. 1980. Geoacoustic modeling of the sea floor. *J. Acoust. Soc. Am.*, **68**, 1313–1340.

Hamilton, M. F., & Blackstock, D. T. 1997. *Nonlinear Acoustics*. Academic Press.

Hampton, L. D. 1967. Acoustic properties of sediments. *J. Acoust. Soc. Am.*, **42**, 882–890.

Hertel, E. S. 1997. A survey of numerical methods for shock physics applications. *In: 1997 International Workshop on New Models and Numerical codes for Shock Wave Processes in Condensed Media*.

Holm, S., & Näsholm, S. P. 2011. Linking multiple relaxation, power-law attenuation, and fractional wave equations. *J. Acoust. Soc. Am.*, **130**, 3038–3045.

Holm, S., & Näsholm, S. P. 2014. Comparison of fractional wave equations for power law attenuation in ultrasound and elastography. *Ultrasound Med. Biol.*, **40**, 695–703.

Jensen, F. B., Kuperman, W. A., Porter, M. B., & Schmidt, H. 2005. *Computational Ocean Acoustics*. American Institute of Physics.

Jing, Y., & Cleveland, R. O. 2007. Modeling the propagation of nonlinear three-dimensional acoustic beams in inhomogeneous media. *J. Acoust. Soc. Am.*, **122**, 1352–1364.

Kamegai, M., & White, J. W. 1994. *A study of near-surface and underwater explosions by computer simulations*. Tech. rept. Lawrence Livermore National Laboratory, Livermore, CA.

Kusel, E. T. 2005. *New Parabolic Equation Solutions for High Frequency and Elastic Media Problems*. Ph.D. thesis, Rensselaer Polytechnic Institute.

LeVeque, R. J. 2002. *Finite Volume Methods for Hyperbolic Problems*. Cambridge University Press.

Lighthill, J. 1980. *Waves in Fluids*. Cambridge University Press, Cambridge.

Maestas, J. T., Taylor, L. F., & Collis, J. M. 2014. Shock wave propagation along constant sloped ocean bottoms. *J. Acoust. Soc. Am.*, **136**, 2987–2997.

McDonald, B. E., & Ambrosiano, J. 1984. High-order upwind flux correction methods for hyperbolic conservation laws. *J. Comp. Phys.*, **56**, 448–460.

McDonald, B. E., & Kuperman, W. A. 1987. Time domain formulation for pulse propagation including nonlinear behavior at a caustic. *J. Acoust. Soc. Am.*, **81**, 1406–1417.

McDonald, B. E., & Orris, G. J. 1998. *High-angle formulation for the nonlinear progressive-wave equation (NPE) model*. Tech. rept. NRL/FR/7140–98-9859. Naval Research Laboratory.

McDonald, B. E., & Piacsek, A. A. 2011. Nonlinear progressive wave equation for stratified atmospheres. *J. Acoust. Soc. Am.*, **130**, 2648–2653.

McDonald, B. E., Caine, P., & West, M. 1994. A tutorial on the nonlinear progressive wave equation (NPE) – part 1. *Applied Acoustics*, **43**, 159–167.

Miller, G. H., & Colella, P. 2001. A high-order eulerian Godunov method for elastic-plastic flow in solids. *J. Comp. Phys.*, **167**, 131–176.

Nachman, A. I., III, J. F. Smith, & Waag, R. C. 1990. An equation for acoustic propagation in inhomogeneous media with relaxation losses. *J. Acoust. Soc. Am.*, **88**, 1585–1595.

Ortigueira, M. D. 2011. *Fractional Calculus for Scientists and Engineers*. Springer.

Outing, D. A. 2004. *Parabolic equation methods for range dependent layered elastic media*. Ph.D. thesis, Rensselaer Polytechnic Institute.

Pierce, A. D. 1989. *Acoustics, an Introduction to its Physical Principles and Applications*. Acoustical Society of America, Woodbury, NY.

Prier, F., & Holm, S. 2011. Nonlinear acoustic wave equations with fractional loss operators. *J. Acoust. Soc. Am.*, **130**, 1125–1132.

Richards, R. 2000. *Principles of Solid Mechanics*. CRC Press.

Rinehart, J. S. 1975. *Stress Transients in Solids*. HyperDynamics.

Samko, S. 2013. Fractional integration and differentiation of variable order: an overview. *Nonlinear Dyn.*, **71**, 653–662.

Soukup, R. J., Simpson, H. J., & Porse, E. C. 2004. *Geoacoustic physical modeling elastic parabolic equation 1 (GPM EPE1) experiment: measurement report and acoustic data*. Tech. rept. NRL/MR-MM/7140–04-8826. Naval Research Laboratory.

Stoll, R. D. 1985. Marine sediment acoustics. *J. Acoust. Soc. Am.*, **77**, 1789–1799.

Stoll, R. D., & Bryan, G. M. 1970. Wave attenuation in saturated sediments. *J. Acoust. Soc. Am.*, **47**, 1440–1447.

Swisdak, M. M. 1978. *Explosion effects and properties: Part II - Explosion effects in water*. Tech. rept. NSWC/WOL TR 76-116. Naval Surface Weapons Center, Silver Spring, MD.

Szabo, T. L. 1993. Time domain nonlinear wave equations for lossy media. *Pages 89–94 of:* Hobaek, H. (ed), *Advances in Nonlinear Acoustics: Proceedings of the 13th ISNA*. World Scientific, Singapore.

Szabo, T. L. 1994. Time domain wave equations for lossy media obeying a frequency power law. *J. Acoust. Soc. Am.*, **96**, 491–500.

Taraldsen, G. 2001. A generalized Westervelt equation for nonlinear medical ultrasound. *J. Acoust. Soc. Am.*, **109**, 1329–1333.

Too, G. P. J., & Lee, S. T. 1995. Thermoviscous effects on transient and steady-state sound beams using nonlinear progressive wave equation models. *J. Acoust. Soc. Am.*, **97**, 867–874.

Toro, E. F. 2009. *Riemann Solvers and Numerical Methods for Fluid Dynamics: A Practical Introduction*. Third edn. Springer.

Tóth, G., & Odstrčil, D. 1996. Comparison of some flux corrected transport and total variation diminishing numerical schemes for hydrodynamic and magnetohydrodynamic problems. *J. Comp. Phys.*, **128**, 82–100.

Treeby, B. E., & Cox, B. T. 2010. Modeling power law absorption and dispersion for acoustic propagation using the fractional Laplacian. *J. Acoust. Soc. Am.*, **127**, 2741–2748.

van Leer, B. 1979. Towards the ultimate conservative difference scheme. V. A second-order sequel to Godunov's method. *J. Comp. Phys.*, **32**, 101–136.

Yang, X., & Cleveland, R. O. 2005. Time domain simulation of nonlinear acoustic beams generated by rectangular pistons with application to harmonic imaging. *J. Acoust. Soc. Am.*, **117**, 113–123.

Zabolotskaya, E. A., & Khokhlov, R. V. 1969. Quasi-plane waves in the nonlinear acoustics of confined beams. *Sov. Phys. Acoust.*, **15**, 35–40.

Zahradnik, J., & Priolo, E. 1995. Heterogeneous formulations of elastodynamic equations and finite-difference schemes. *Geophys. J. Int.*, **120**, 663–676.

Zhou, J. X., Zhang, X. Z., & Rogers, P. H. 1987. Effect of frequency dependence of sea-bottom attenuation on the optimum frequency for acoustic propagation in shallow water. *J. Acoust. Soc. Am.*, **82**, 287–292.

Zhou, Y., & Wang, Z. J. 2010. Absorbing boundary conditions for the Euler and Navier-Stokes equations with the spectral difference method. *J. Comp. Phys.*, **229**, 8733–8749.

APPENDIX A - THE FRACTIONAL LAPLACIAN

The following discussion provides a definition of the fractional Laplacian as defined by Chen and Holm (Chen & Holm, 2004). The operator's definition naturally includes boundary conditions and the formulation allows the relaxation of the hypersingularity normally found in the integral. It is therefore more useful in engineering modeling.

Historically, there have been various interpretations of the fractional derivatives including the fractional Laplacian (Ortigueira, 2011). A common approach is to define the fractional Laplacian in terms of the Riesz potential (Gorenflo & Mainardi, 1998). The Riesz potential I_d^s of order s and d dimensions is given by (Samko, 2013)

$$I_d^s\phi(x) = \frac{\Gamma[(d-s)/2]}{\pi^{s/2}2^s\Gamma(s/2)}\int_\Omega \frac{\phi(\xi)}{||x-\xi||^{d-s}}\mathrm{d}\Omega(\xi), \quad 0<s<2, \tag{A.1}$$

where Γ represents the gamma function and Ω is the domain of integration. The fractional Laplacian (derivative) is then defined as

$$(-\nabla^2)_*^{s/2}\varphi(x) = -\nabla^2[I_d^{2-s}\varphi(x)], \tag{A.2}$$

which gives

$$(-\nabla^2)_*^{s/2}\varphi(x) = -\frac{\Gamma[(d-2+s)/2]}{\pi^{(2-s)/2}2^{2-s}\Gamma[(2-s)/2]}\nabla^2\int_\Omega \frac{\varphi(\xi)}{||x-\xi||^{d-2+s}}\mathrm{d}\Omega(\xi). \tag{A.3}$$

For d dimensions, the Laplacian operator has the following expression

$$\nabla^2\varphi(x) = \frac{\partial^2\varphi}{\partial r^2} + \frac{d-1}{r}\frac{\partial\varphi}{\partial r}, \tag{A.4}$$

where $r = ||x-\xi||$. Applying this expression to Eq. (A.3) yields

$$(-\nabla^2)_*^{s/2}\varphi(x) = -\frac{(d-2+s)s\Gamma[(d-2+s)/2]}{\pi^{(2-s)/2}2^{2-s}\Gamma[(2-s)/2]}\int_\Omega \frac{\varphi(\xi)}{||x-\xi||^{d+s}}\mathrm{d}\Omega(\xi). \tag{A.5}$$

This definition of the fractional Laplacian includes a detrimental hypersingularity of $d+s$. Therefore, an alternative definition of Chen and Holm is presented. The new definition is given by

$$(-\nabla^2)^{s/2}\varphi(x) = -I_d^{2-s}[\nabla^2\varphi(x)], \tag{A.6}$$

which gives

$$(-\nabla^2)^{s/2}\varphi(x) = -\frac{\Gamma[(d-2+s)/2]}{\pi^{(2-s)/2}2^{2-s}\Gamma[(2-s)/2]}\int_\Omega \frac{\nabla^2\varphi(\xi)}{||x-\xi||^{d-2+s}}\mathrm{d}\Omega(\xi). \tag{A.7}$$

Equation (A.7) contains only a weak singularity of $d-2+s$. Equations (A.5) and (A.7) can be related to each other using Green's second identity:

$$\int_\Omega v\nabla^2\varphi \,\mathrm{d}\xi = \int_\Omega \varphi\nabla^2 v \,\mathrm{d}\Omega(\xi) - \int_S \left(\varphi\frac{\partial v}{\partial n} - v\frac{\partial\varphi}{\partial n}\right)\mathrm{d}S(\xi), \tag{A.8}$$

where S represents the surface of the domain and n is the unit outward normal vector to the surface. Let $v = 1/||x-\xi||^{d-2+s}$, and

$$\varphi(x)|_{x\in S} = D(x), \tag{A.9a}$$

$$\frac{\partial\varphi(x)}{\partial n}|_{x\in S} = N(x), \tag{A.9b}$$

which represent boundary conditions. Using Green's identity, (A.7) reduces to

$$\begin{aligned}(-\nabla^2)^{s/2}\varphi(x) = &-\frac{(d-2+s)s\Gamma[(d-2+s)/2]}{\pi^{(2-s)/2}2^{2-s}\Gamma[(2-s)/2]}\int_\Omega \frac{\varphi(\xi)}{||x-\xi||^{d+s}}\mathrm{d}\Omega(\xi)\\ &+ h\int_S\left[\varphi(\xi)\frac{\partial}{\partial n}\left(\frac{1}{||x-\xi||^{d+s-2}}\right) - \frac{1}{||x-\xi||^{d+s-2}}\frac{\partial\varphi(\xi)}{\partial n}\right]\mathrm{d}S(\xi),\end{aligned} \tag{A.10}$$

where

$$h = \frac{\Gamma[(d-2+s)/2]}{\pi^{(2-s)/2}2^{2-s}\Gamma[(2-s)/2]}. \tag{A.11}$$

This new definition of the fractional Laplacian given by Chen and Holm is seen as the original

definition (A.5) augmented by a boundary integral:

$$(-\nabla^2)^{s/2}\varphi(x) = (-\nabla^2)_*^{s/2}\varphi(x) + h\int_S \left[D(\xi)\frac{\partial}{\partial n}\left(\frac{1}{||x-\xi||^{d+s-2}}\right) - \frac{N(\xi)}{||x-\xi||^{d+s-2}}\right] \mathrm{d}S(\xi). \tag{A.12}$$

The definition is not biased towards any particular direction (isotropic), and incorporates boundary conditions provides that the boundary functions $D(x)$ and $N(x)$ are well behaved. The rectangular domains and standard boundary conditions (Dirichlet and Neumann) employed in this work allow this definition of the fractiona Laplacian to be used.

APPENDIX B - COMPLETE WEAK ELASTICITY STUDY RESULTS

All comparisons performed in the weak elasticity study (Section 4.5) are provided below. Results at the receivers as well as entire pressure fields are given.

CASE 1

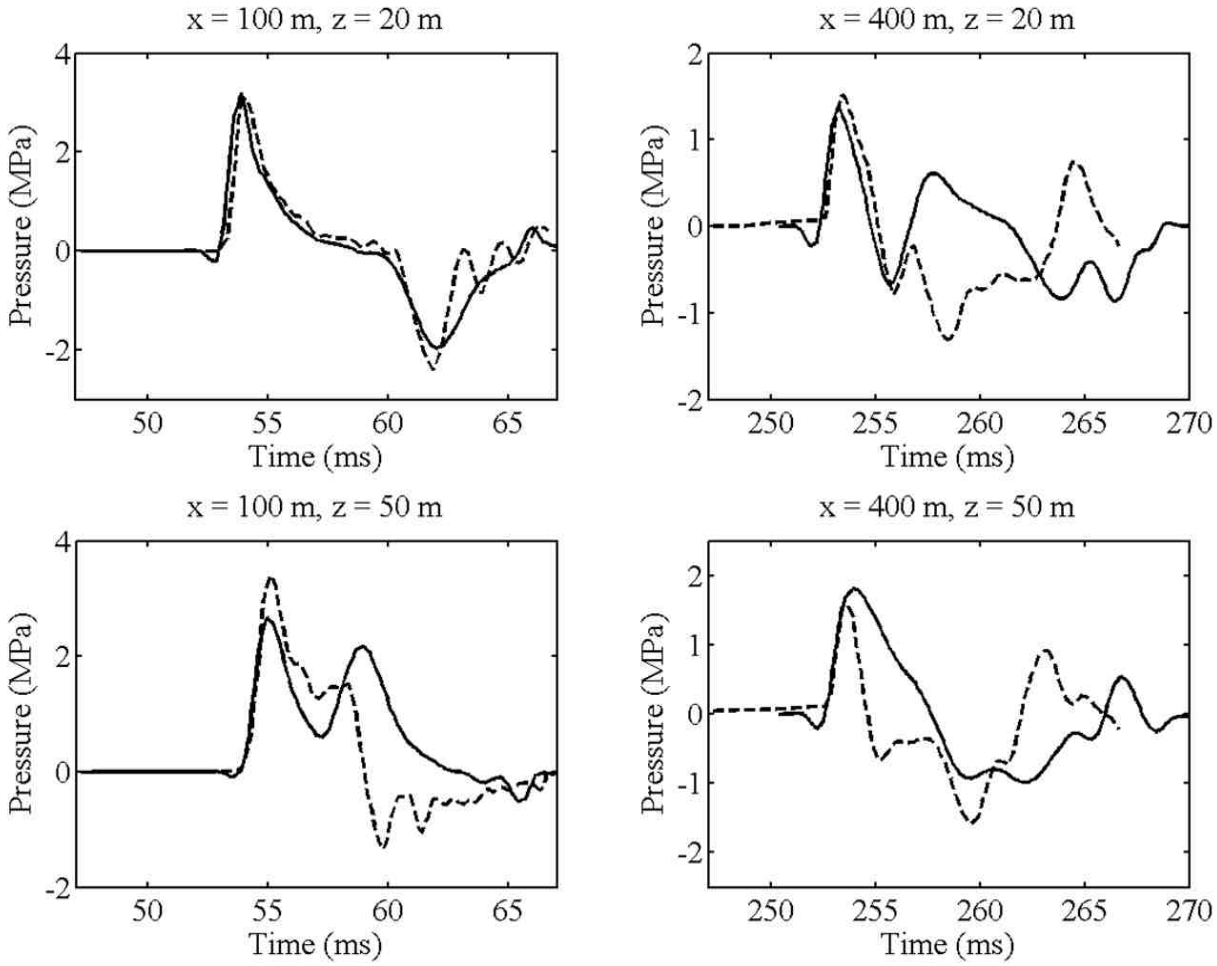

Figure B.1: Weakly-elastic nonlinear progressive wave equation and progressive elastic-fluid solutions for Case 1 comparison ($\nu = 0.493$). Dashed line: WENPE solution; solid line: progressive elastic-fluid solution.

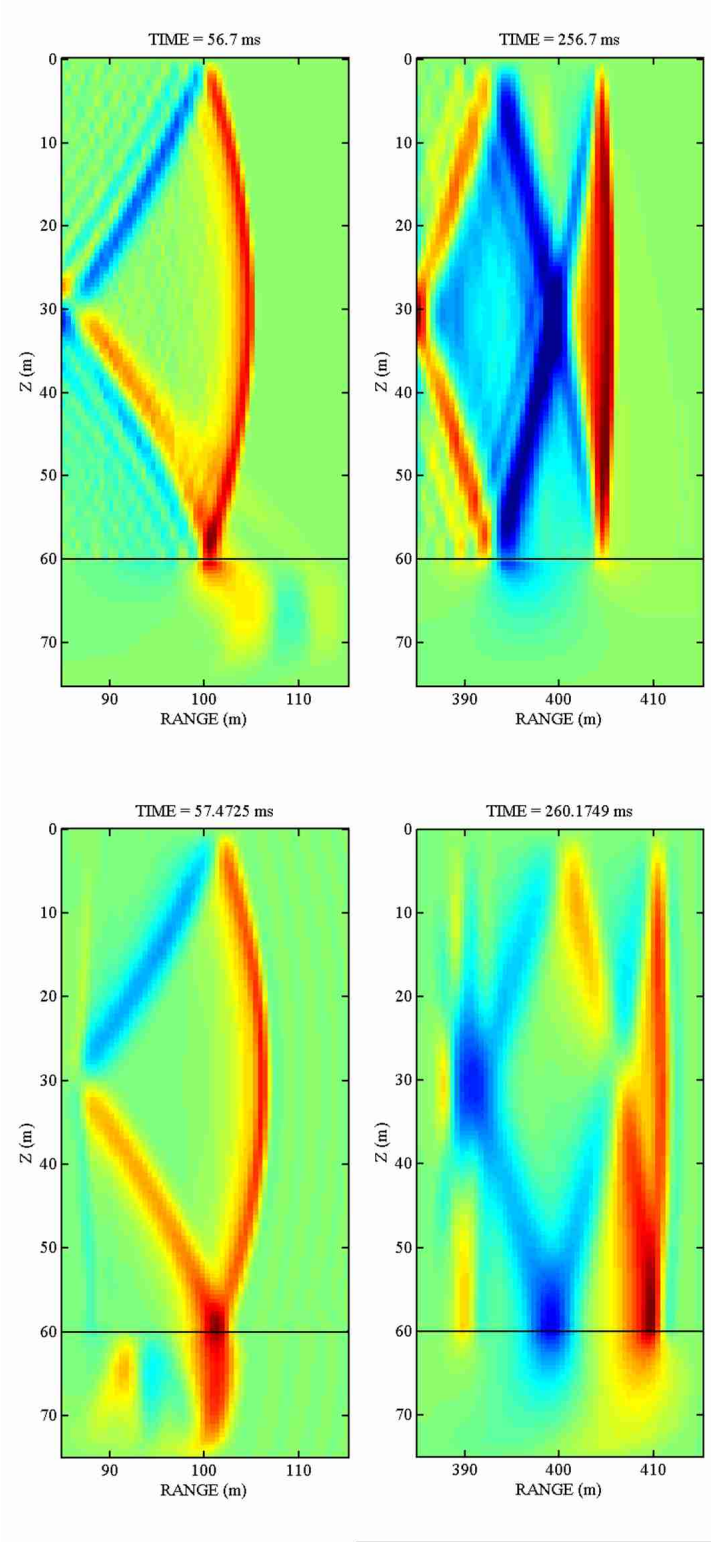

Figure B.2: Pressure fields near receiver locations for Case 1. Top row represents weakly-elastic nonlinear progressive wave equation results and bottom row represents progressive elastic-fluid results.

CASE 2

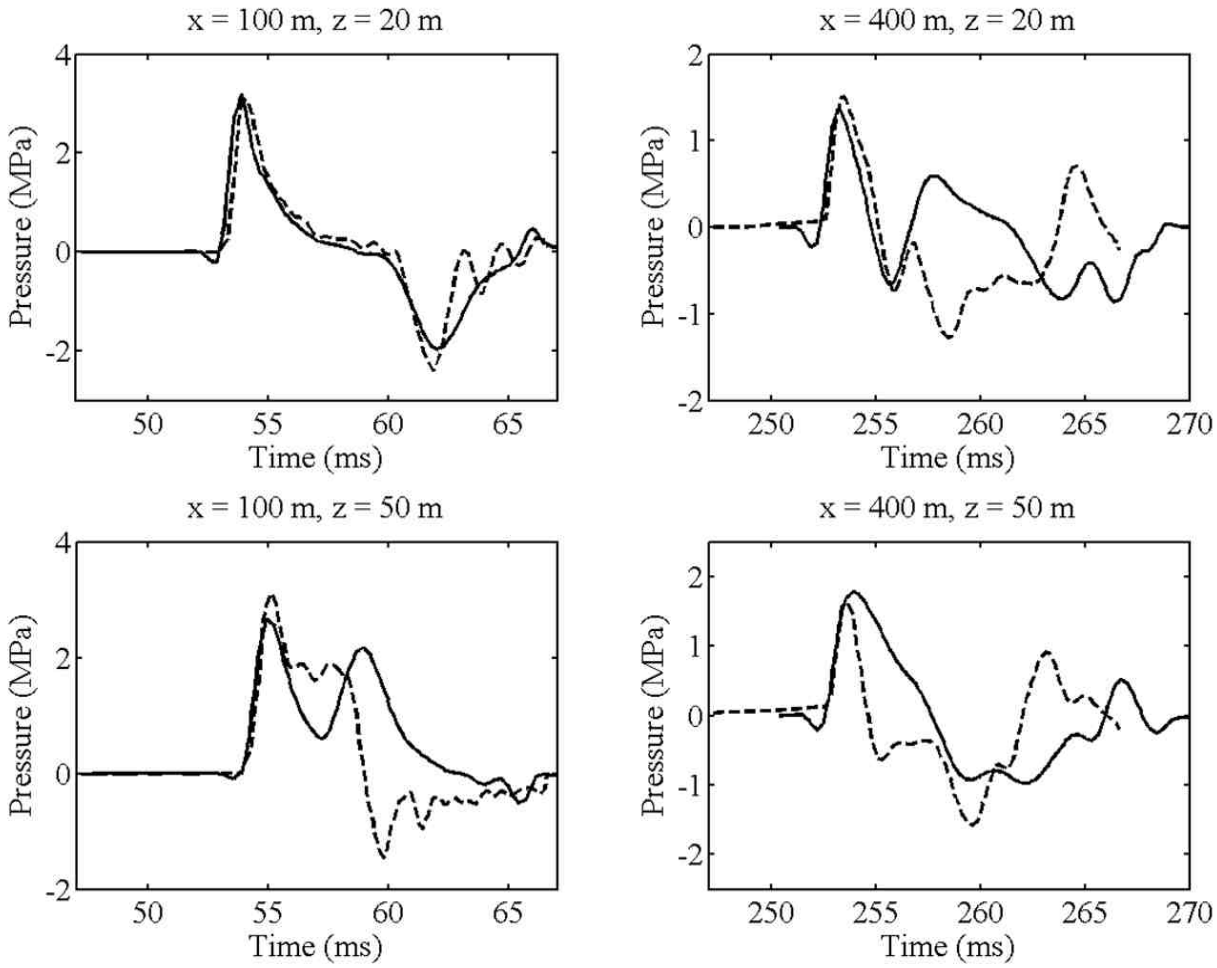

Figure B.3: Weakly-elastic nonlinear progressive wave equation and progressive elastic-fluid solutions for Case 2 comparison ($\nu = 0.469$). Dashed line: WENPE solution; solid line: progressive elastic-fluid solution.

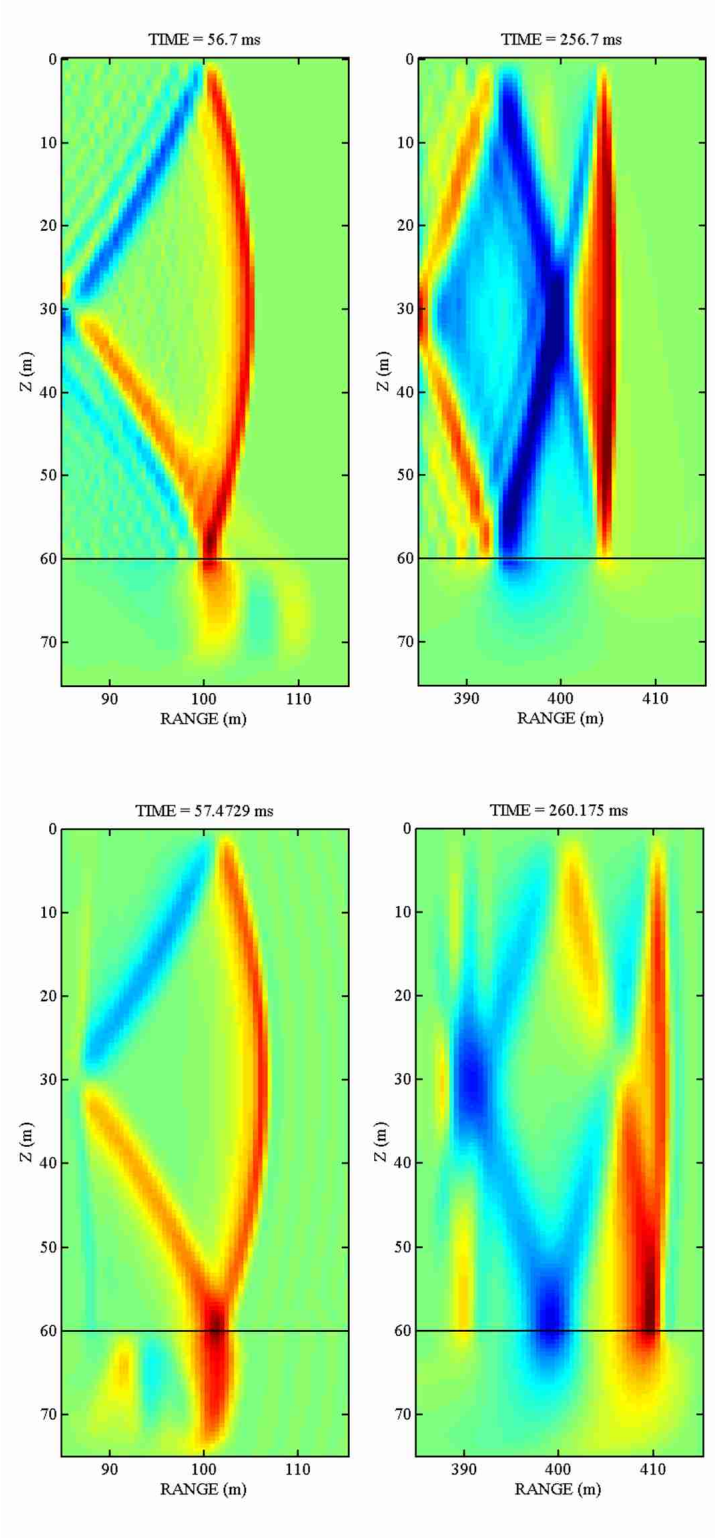

Figure B.4: Pressure fields near receiver locations for Case 2. Top row represents weakly-elastic nonlinear progressive wave equation results and bottom row represents progressive elastic-fluid results.

CASE 3

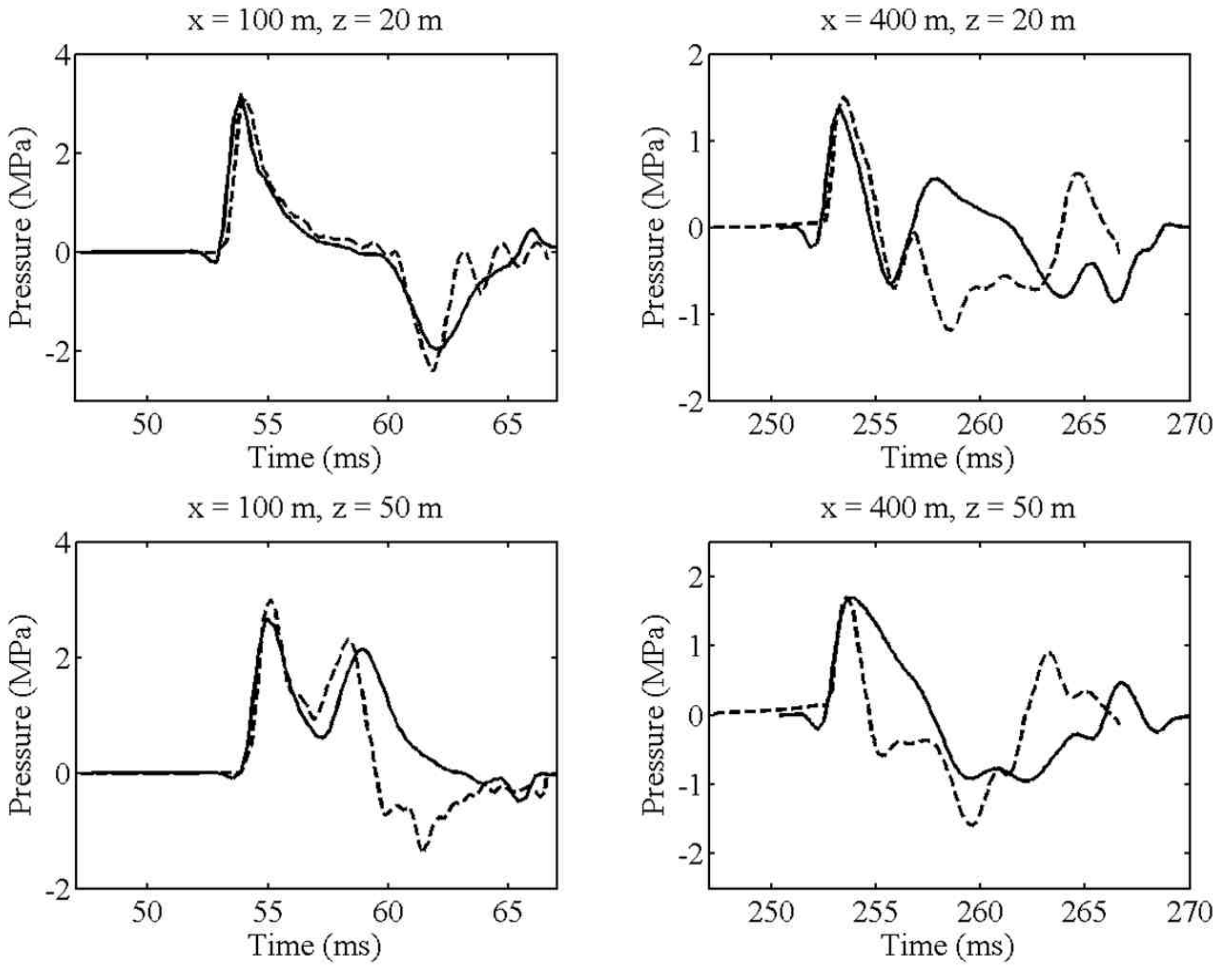

Figure B.5: Weakly-elastic nonlinear progressive wave equation and progressive elastic-fluid solutions for Case 3 comparison ($\nu = 0.424$). Dashed line: WENPE solution; solid line: progressive elastic-fluid solution.

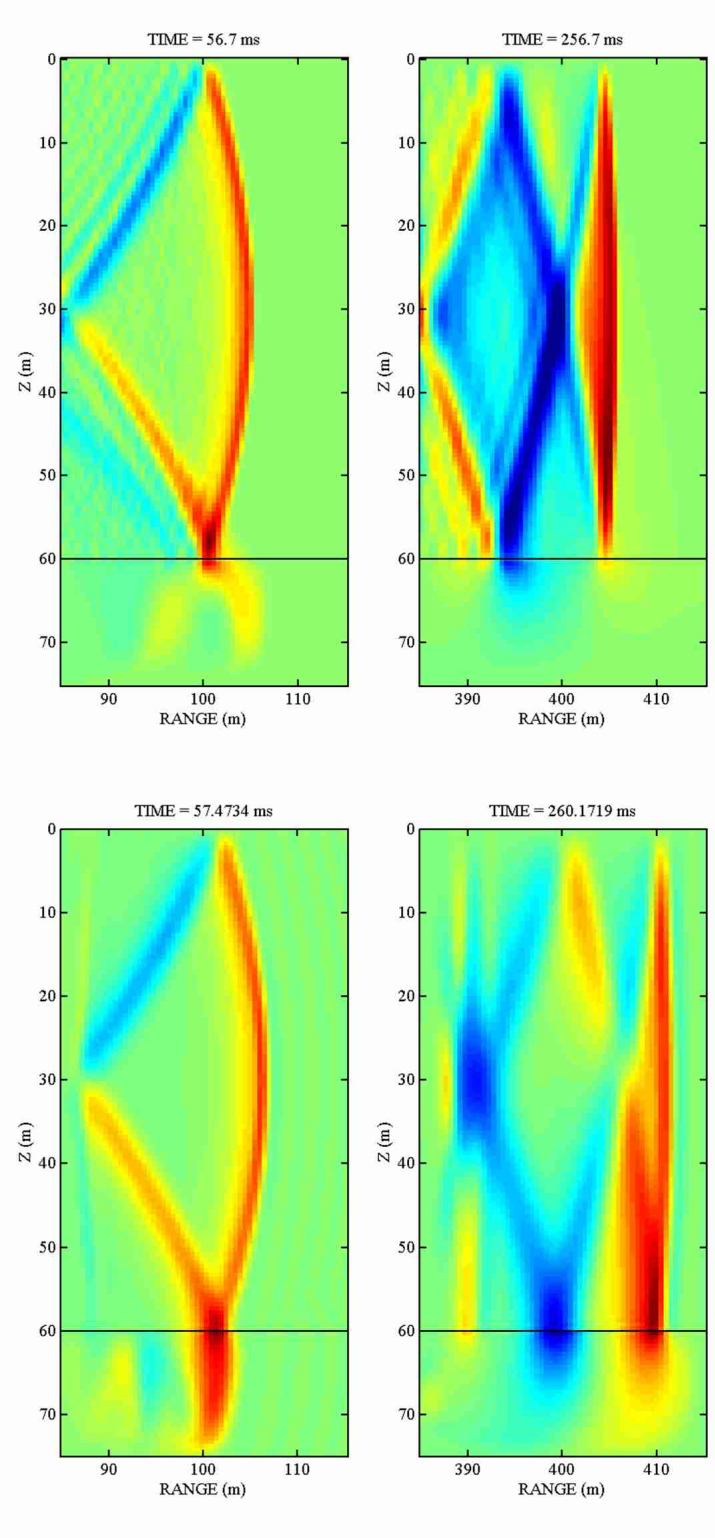

Figure B.6: Pressure fields near receiver locations for Case 3. Top row represents weakly-elastic nonlinear progressive wave equation results and bottom row represents progressive elastic-fluid results.

CASE 4

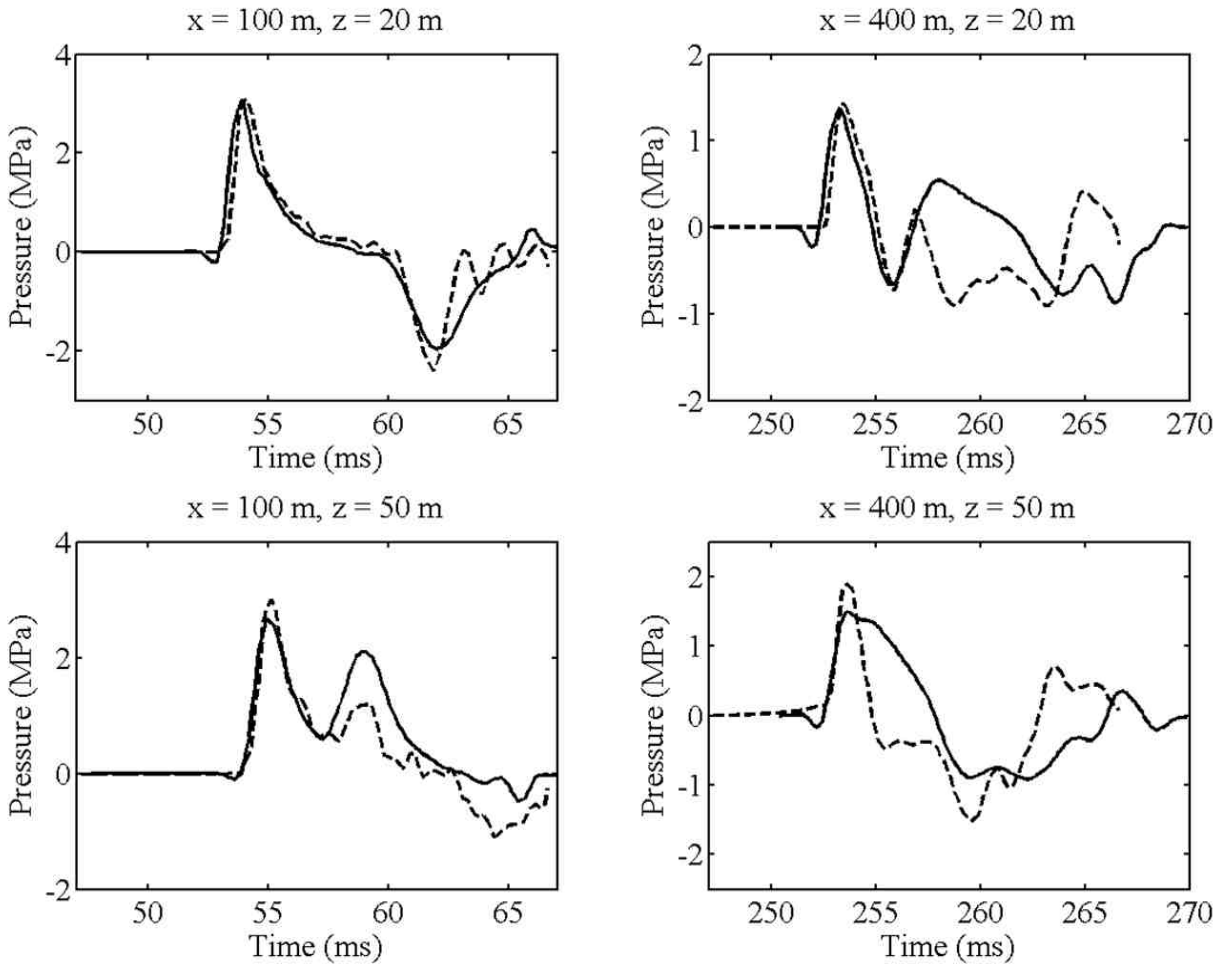

Figure B.7: Weakly-elastic nonlinear progressive wave equation and progressive elastic-fluid solutions for Case 4 comparison ($\nu = 0.346$). Dashed line: WENPE solution; solid line: progressive elastic-fluid solution.

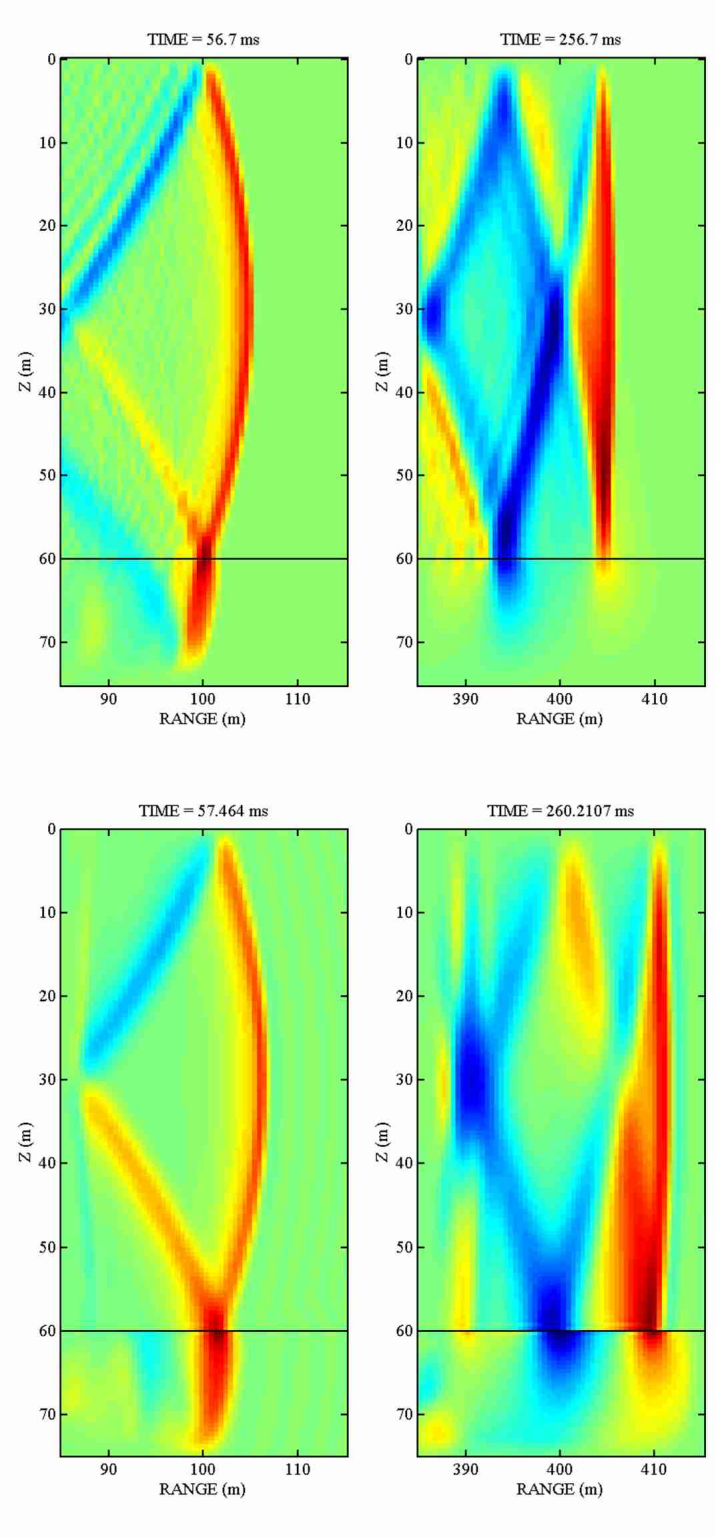

Figure B.8: Pressure fields near receiver locations for Case 4. Top row represents weakly-elastic nonlinear progressive wave equation results and bottom row represents progressive elastic-fluid results.

CASE 5

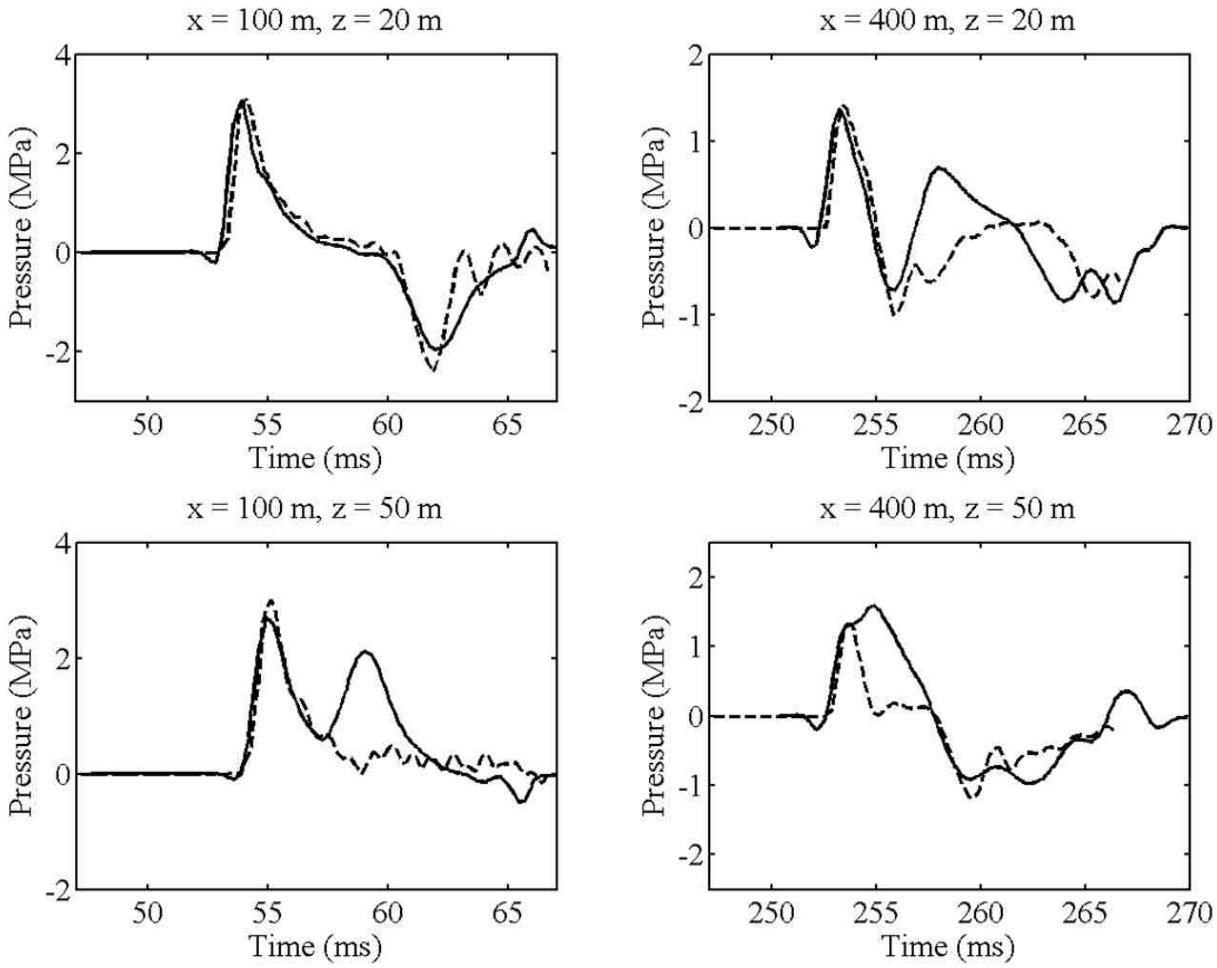

Figure B.9: Weakly-elastic nonlinear progressive wave equation and progressive elastic-fluid solutions for Case 5 comparison ($\nu = 0.210$). Dashed line: WENPE solution; solid line: progressive elastic-fluid solution.

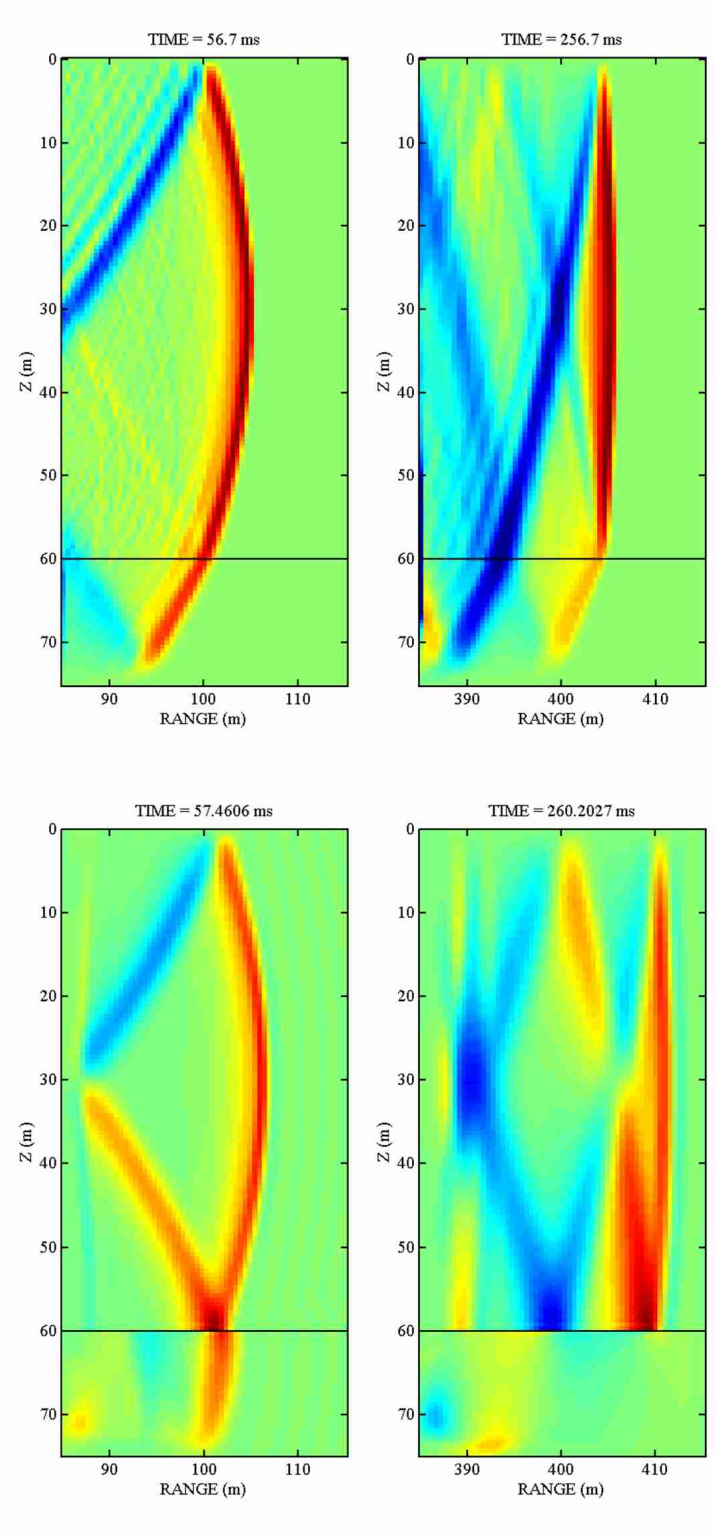

Figure B.10: Pressure fields near receiver locations for Case 5. Top row represents weakly-elastic nonlinear progressive wave equation results and bottom row represents progressive elastic-fluid results.

CASE 6

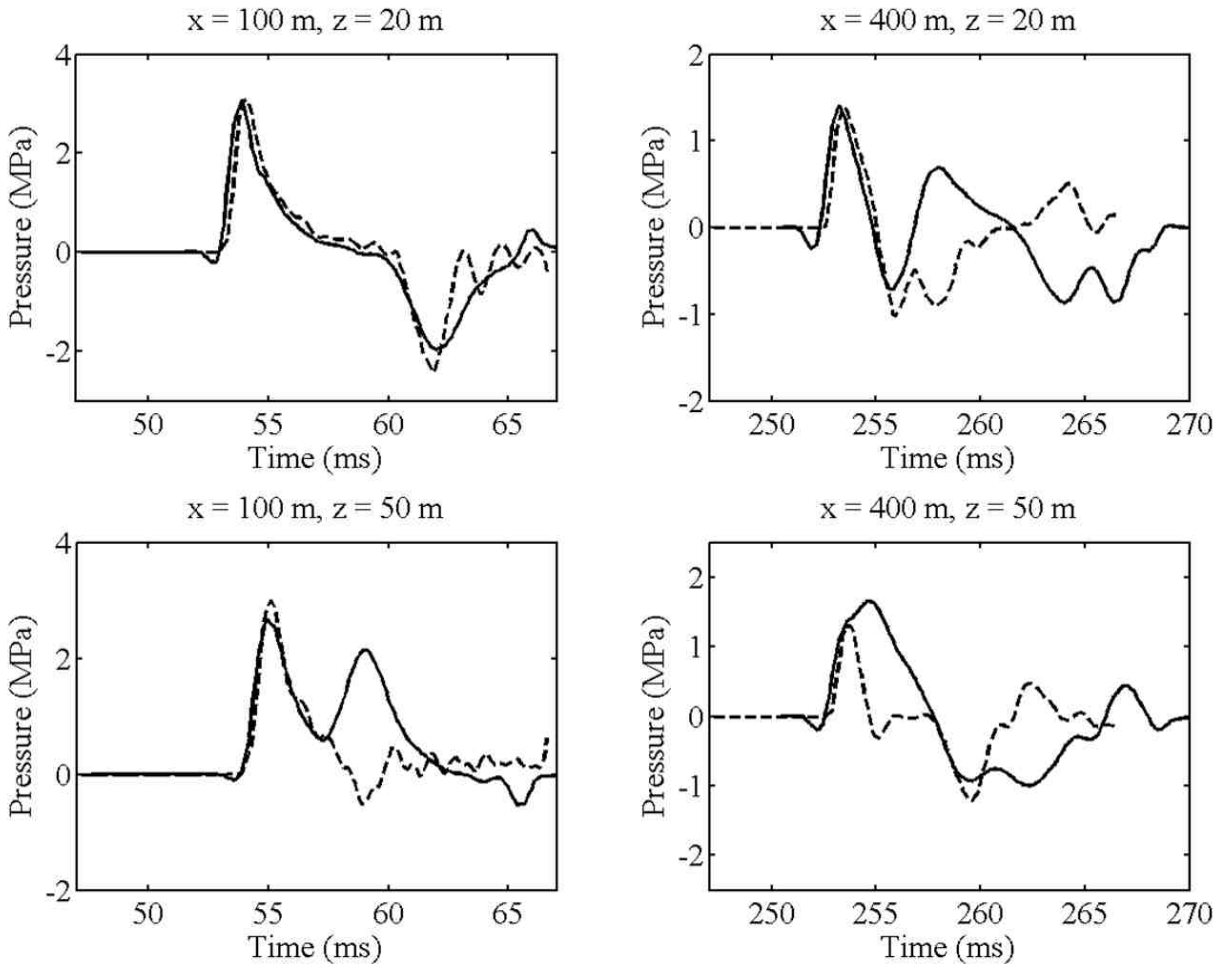

Figure B.11: Weakly-elastic nonlinear progressive wave equation and progressive elastic-fluid solutions for Case 6 comparison (ν = -0.061). Dashed line: WENPE solution; solid line: progressive elastic-fluid solution.

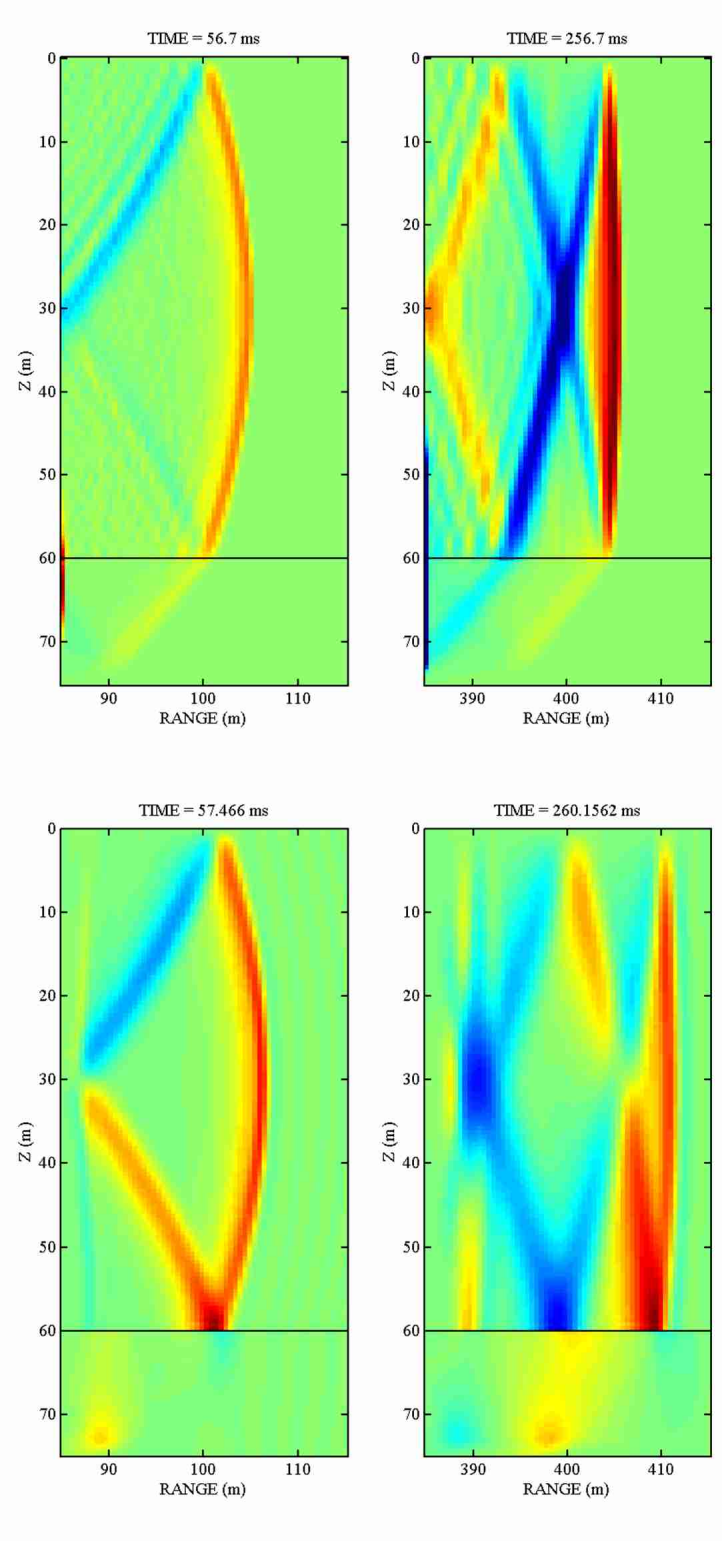

Figure B.12: Pressure fields near receiver locations for Case 6. Top row represents weakly-elastic nonlinear progressive wave equation results and bottom row represents progressive elastic-fluid results.

APPENDIX C - SLOPE LIMITING

The high-order Godunov scheme implemented in the elastic models can give rise to spurious post-shock (Gibbs') oscillations (Arora & Roe, 1997). To prevent these oscillations, it is necessary to apply a small amount of numerical dissipation in the areas of strong shock. This is done by limiting the slopes with a flattening parameter, χ.

The method for computing χ follows from that of Miller and Colella in which the dissipation correlates to a measured relative shock strength (Miller & Colella, 2001). First, the divergence of the velocity is computed in each cell by

$$\left(\frac{\partial v_x}{\partial x}\right)_{ij} + \left(\frac{\partial v_z}{\partial z}\right)_{ij}, \tag{C.1}$$

and cells whose velocity divergence is less than 0.5 have the flattening parameter set to unity. In the areas where there exists an abrupt change in velocity, a relative shock strength is computed. If cell (i, j) is a fluid cell, the shock strength there is measured with

$$\xi_{x,ij} = \frac{|P_{i+1,j} - P_{i-1,j}|}{K_{i,j}} \tag{C.2}$$

for the x direction and

$$\xi_{z,ij} = \frac{|P_{i,j+1} - P_{i,j-1}|}{K_{i,j}} \tag{C.3}$$

for the z direction. If the cell is a solid cell, the shock strength is measured with

$$\xi_{x,ij} = \frac{||(\boldsymbol{\sigma}\mathbf{e}_x)_{i+1,j} - (\boldsymbol{\sigma}\mathbf{e}_x)_{i-1,j}||_\infty}{\sqrt{\det(\mathcal{A}_{x,ij})}} \tag{C.4}$$

for the x direction and

$$\xi_{z,ij} = \frac{||(\boldsymbol{\sigma}\mathbf{e}_z)_{i,j+1} - (\boldsymbol{\sigma}\mathbf{e}_z)_{i,j-1}||_\infty}{\sqrt{\det(\mathcal{A}_{z,ij})}} \tag{C.5}$$

for the z direction, where $\mathbf{e}_x$ and $\mathbf{e}_z$ are direction unit vectors, $\boldsymbol{\sigma}$ is the (two-dimensional)

Cauchy stress tensor

$$\boldsymbol{\sigma} = \begin{bmatrix} \sigma_{xx} & \sigma_{xz} \\ \sigma_{xz} & \sigma_{zz} \end{bmatrix}, \tag{C.6}$$

and $\mathcal{A}_x$ and $\mathcal{A}_z$ are the acoustic propagation tensors given by

$$\mathcal{A}_x = \begin{bmatrix} \lambda + 2\mu & \mu \\ \mu & \lambda \end{bmatrix} \qquad \text{and} \qquad \mathcal{A}_z = \begin{bmatrix} \lambda & \mu \\ \mu & \lambda + 2\mu \end{bmatrix}. \tag{C.7}$$

It is then necessary to differentiate between steep and broad shocks using a ratio of pressures in the fluid cells or directional stresses in the solid cells. For the fluid cell, this ratio is given by

$$\varsigma_{x,ij} = \frac{|P_{i+1,j} - P_{i-1,j}|}{|P_{i+2,j} - P_{i-2,j}|} \tag{C.8}$$

for the x direction and

$$\varsigma_{z,ij} = \frac{|P_{i,j+1} - P_{i,j-1}|}{|P_{i,j+2} - P_{i,j-2}|} \tag{C.9}$$

for the z direction. For the solid cell, the ratio is given by

$$\varsigma_{x,ij} = \frac{||(\boldsymbol{\sigma}\mathbf{e}_x)_{i+1,j} - (\boldsymbol{\sigma}\mathbf{e}_x)_{i-1,j}||_\infty}{||(\boldsymbol{\sigma}\mathbf{e}_x)_{i+2,j} - (\boldsymbol{\sigma}\mathbf{e}_x)_{i-2,j}||_\infty} \tag{C.10}$$

for the x direction and

$$\varsigma_{z,ij} = \frac{||(\boldsymbol{\sigma}\mathbf{e}_z)_{i,j+1} - (\boldsymbol{\sigma}\mathbf{e}_z)_{i,j-1}||_\infty}{||(\boldsymbol{\sigma}\mathbf{e}_z)_{i,j+2} - (\boldsymbol{\sigma}\mathbf{e}_z)_{i,j-2}||_\infty} \tag{C.11}$$

for the z direction. When $\varsigma \approx 1$ the shock is relatively steep and will produce spurious oscillations. The minimum values of the flattening parameter in the x and z directions are based on the shock steepness:

$$\chi_{\min,a,ij} = \max\left(0, \min\left(1, \frac{s_1 - \varsigma_{a,ij}}{s_1 - s_0}\right)\right) \tag{C.12}$$

where a is x or z depending on the direction considered and s_0 and s_1 are numerical constants.

The values of $s_0 = 0.75$ and $s_1 = 0.85$ are used in this work. A directional flattening parameter, $\tilde{\chi}_{ij}$, $\chi_{\min,ij} \leq \tilde{\chi}_{ij} \leq 1$, is given by

$$\tilde{\chi}_{x,ij} = \begin{cases} \min\left(1, \max\left(\frac{\xi_1 - \xi_{x,ij}}{\xi_1 - \xi_0}, \chi_{\min,x,ij}\right)\right) & (\mathbf{v}\cdot\mathbf{e}_x)_{i+1,j} < (\mathbf{v}\cdot\mathbf{e}_x)_{i-1,j} \\ 1 & \text{otherwise} \end{cases} \tag{C.13}$$

for the x direction and

$$\tilde{\chi}_{z,ij} = \begin{cases} \min\left(1, \max\left(\frac{\xi_1 - \xi_{z,ij}}{\xi_1 - \xi_0}, \chi_{\min,z,ij}\right)\right) & (\mathbf{v}\cdot\mathbf{e}_z)_{i,j+1} < (\mathbf{v}\cdot\mathbf{e}_z)_{i,j-1} \\ 1 & \text{otherwise} \end{cases} \tag{C.14}$$

for the z direction, where $\xi_0 = 0.25$ and $\xi_1 = 0.75$ in this work. The flattening parameter for cell (i, j) is then given by

$$\chi_{ij} = \min\left(\tilde{\chi}_{x,ij}, \tilde{\chi}_{z,ij}\right). \tag{C.15}$$

APPENDIX D - TANK EXPERIMENT PRESSURE FIELDS

Pressure fields from the tank experiment comparisons (Section 5.5.2) are provided below.

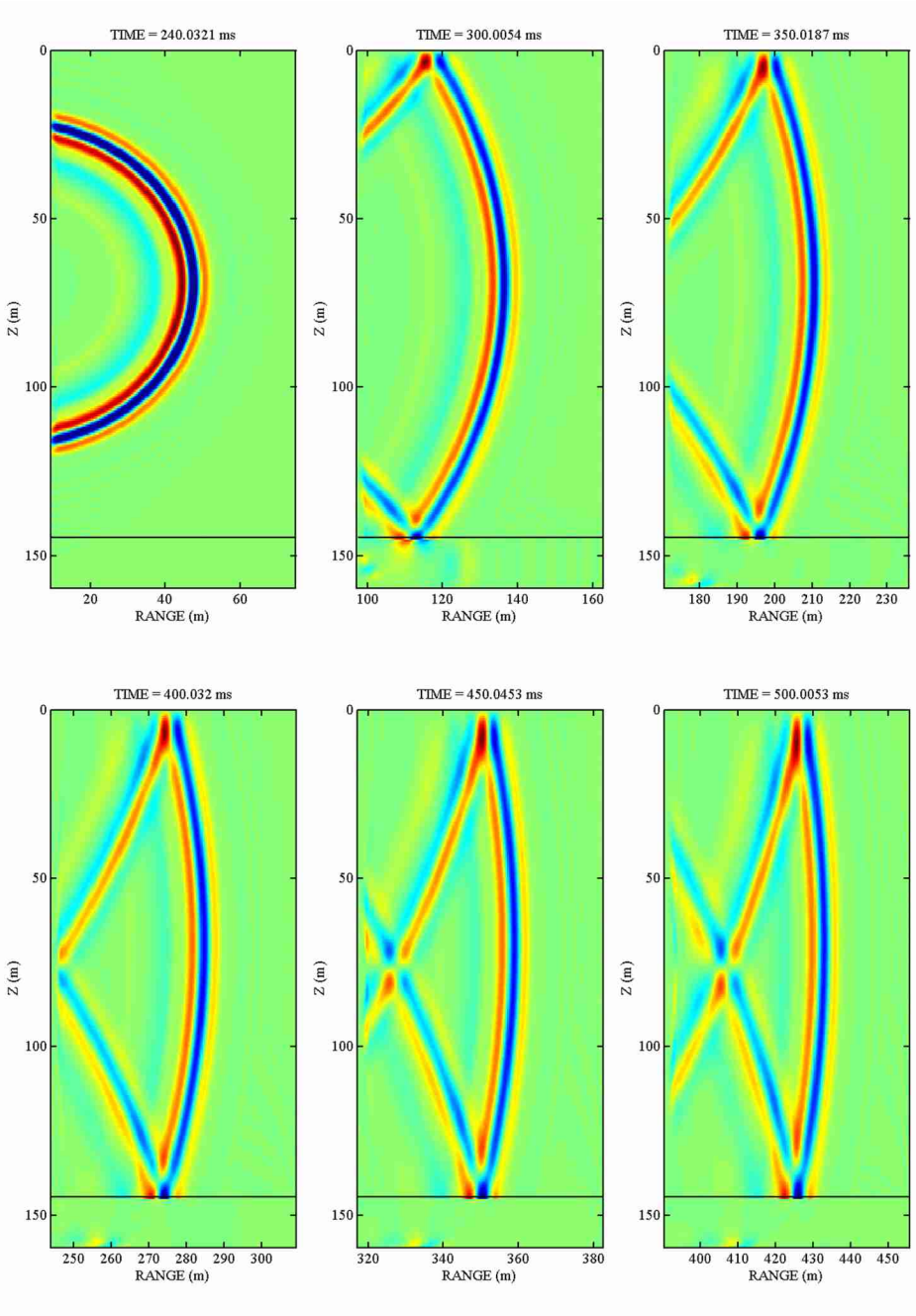

Figure D.1: Pressure fields for the flat ocean bottom case.

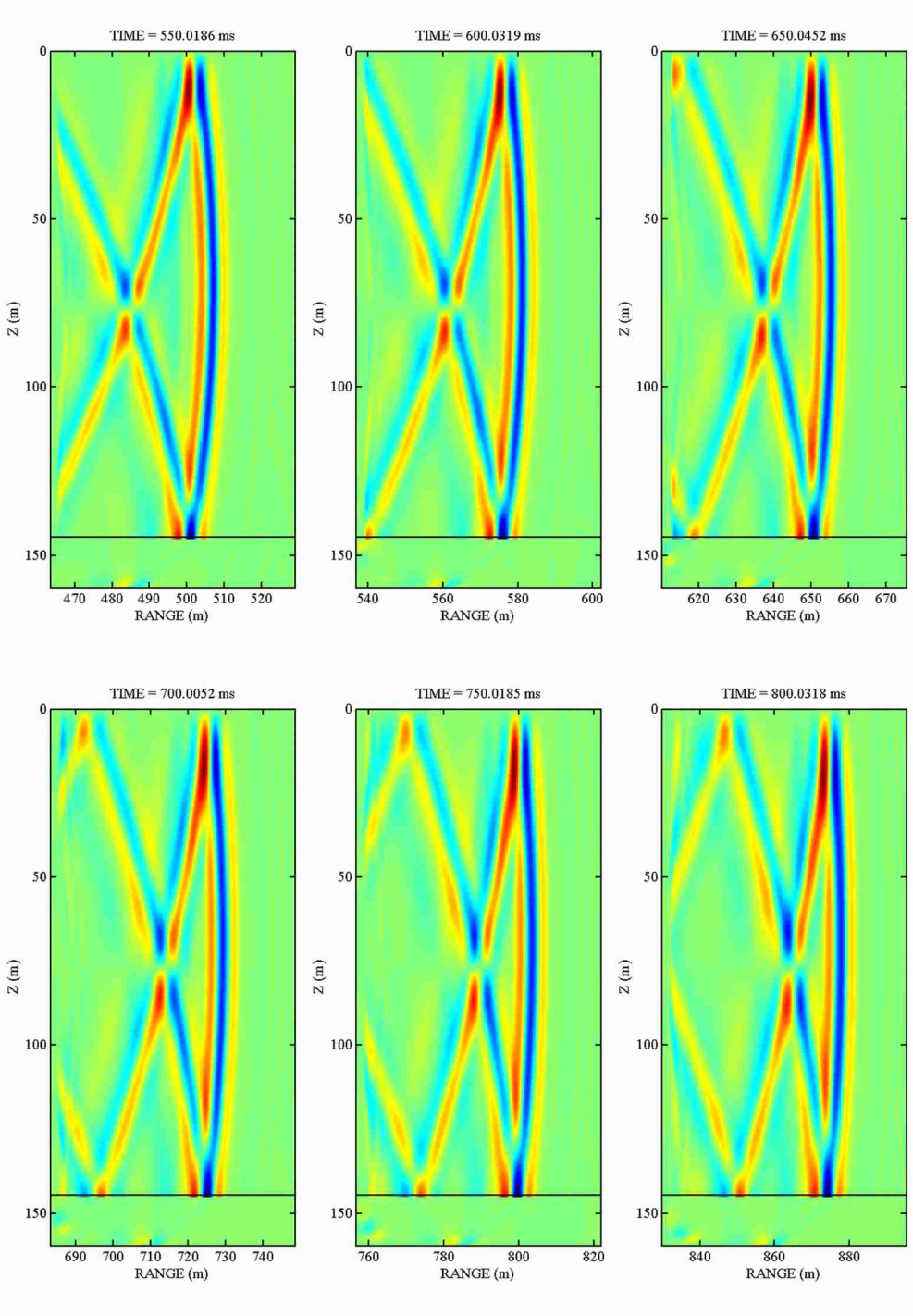

Figure D.2: Pressure fields for the flat ocean bottom case.

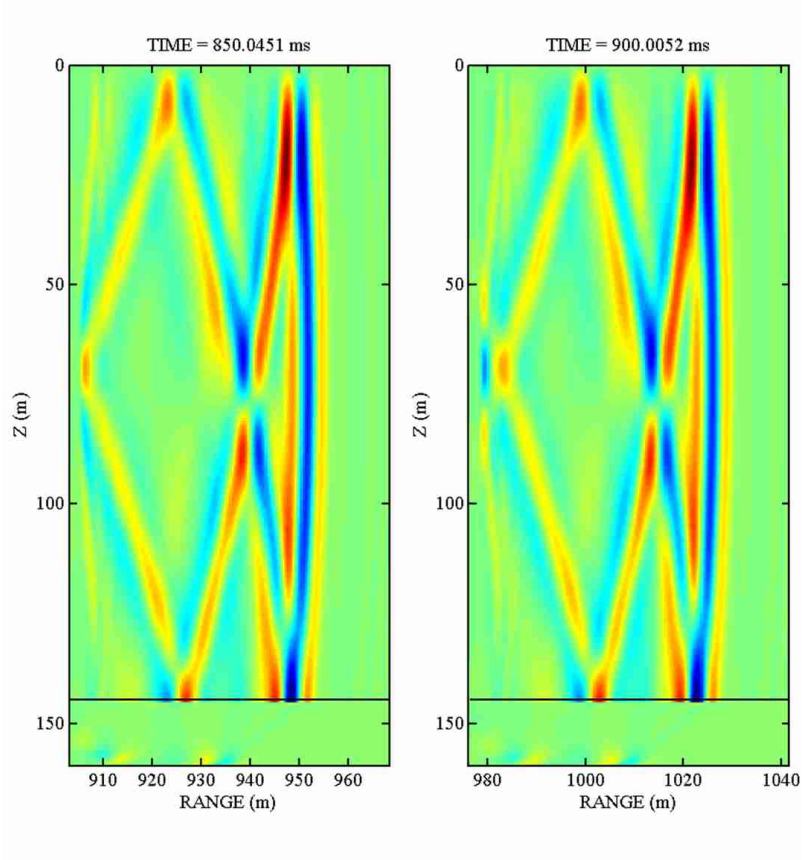

Figure D.3: Pressure fields for the flat ocean bottom case.

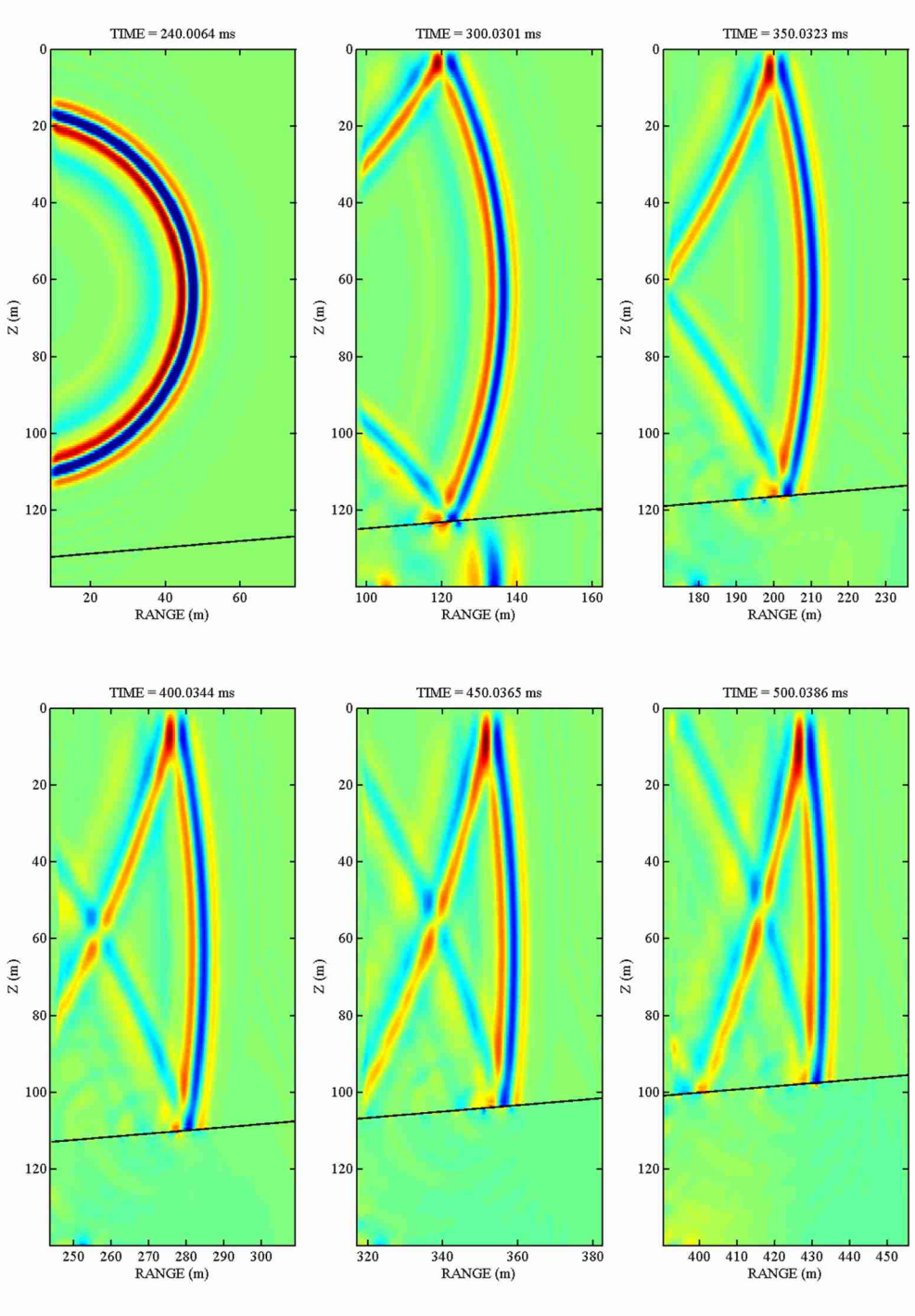

Figure D.4: Pressure fields for the sloped ocean bottom case.

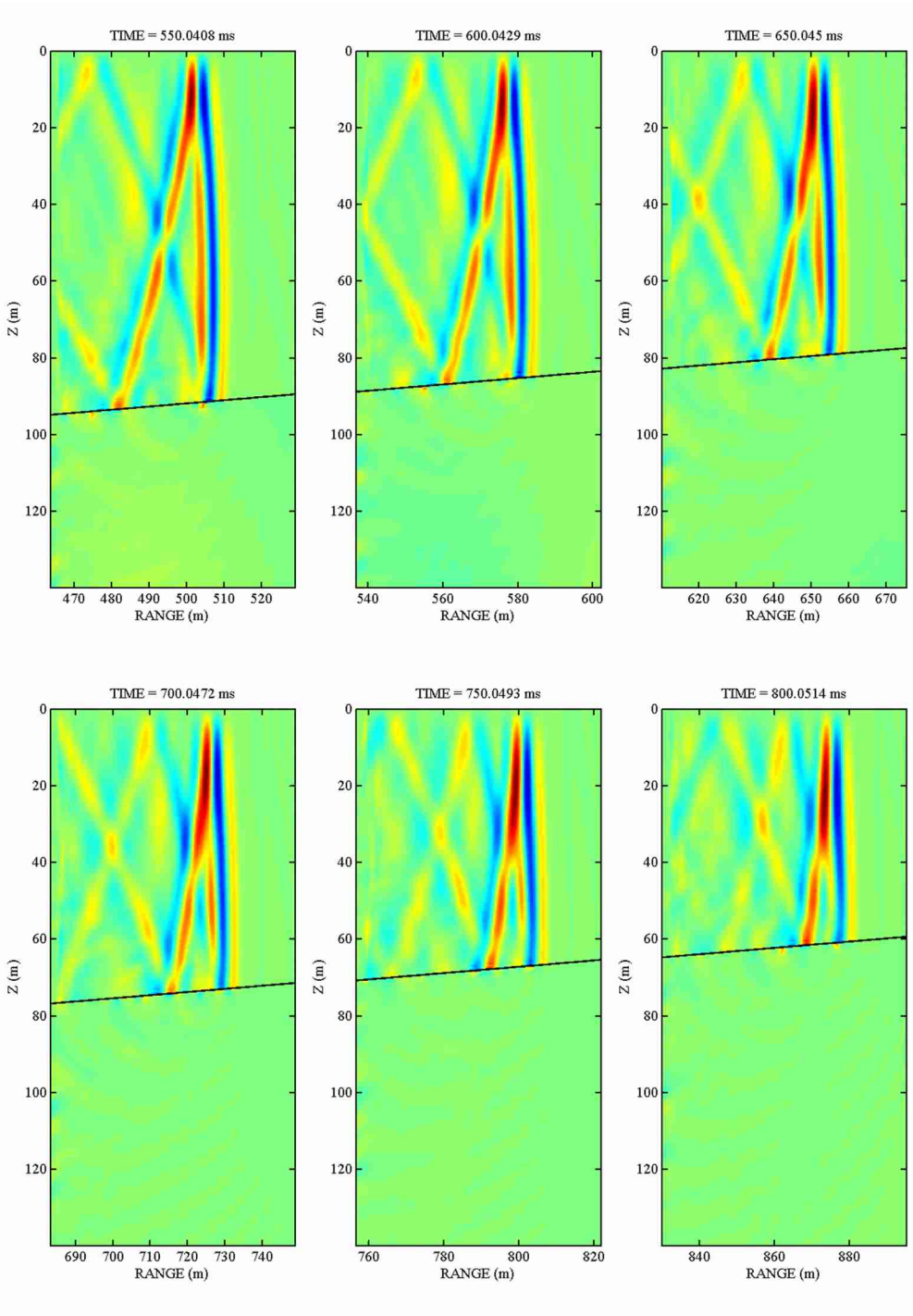

Figure D.5: Pressure fields for the sloped ocean bottom case.

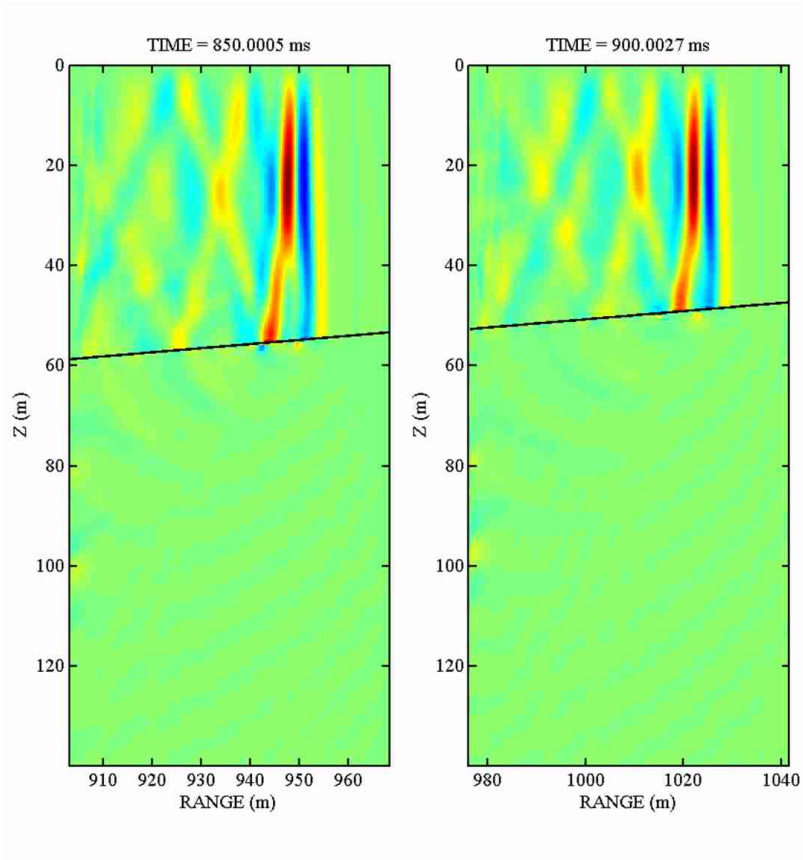

Figure D.6: Pressure fields for the sloped ocean bottom case.